



Highlights 2006

**Berliner Elektronenspeicherring-Gesellschaft für Synchrotronstrahlung m.b.H.**

Member of the Leibniz Association

**Published by:**

Berliner Elektronenspeicherring-Gesellschaft für  
Synchrotronstrahlung m.b.H. – BESSY

Albert-Einstein-Straße 15

12489 Berlin, Germany

phone +49 (0)30 / 6392 2999

fax +49 (0)30 / 6392 2990

[www.bessy.de](http://www.bessy.de)

[info@bessy.de](mailto:info@bessy.de)

**Board of Directors:**

Prof. Dr. Dr. h.c. Wolfgang Eberhardt,

Prof. Dr. Eberhard Jaeschke,

Thomas Frederking

**Editors:**

Dr. Heike Henneken,

Dr. Markus Sauerborn

**Layout:**

Annette Weber, Stitz & Betz GmbH, Berlin

ISSN Number: 1611-6127

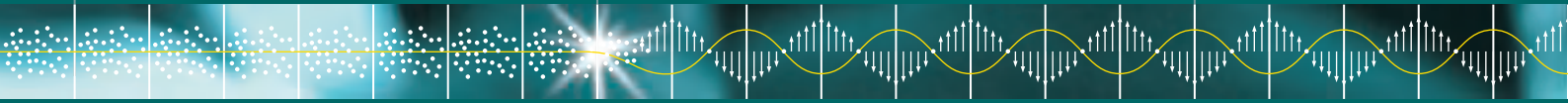
Cover Photo by Henrik Spohler / laif



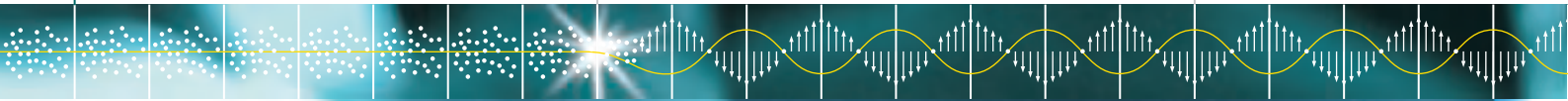
**Berliner Elektronenspeicherring-Gesellschaft für Synchrotronstrahlung m.b.H.**

Member of the Leibniz Association





<b>Introduction</b>	<b>04</b>
<b>Scientific Highlights</b>	<b>06</b>
Atomic Physics	08
Magnetism	10
Surface Sciences	16
Applied Sciences	22
Material Sciences	26
Life Sciences	30
Metrology	34
<b>News &amp; Events</b>	<b>36</b>
<b>Femtosing Special</b>	<b>42</b>
<b>Facility Report</b>	<b>48</b>
Maschine Operation	49
Beamline Developments	50
STARS shining bright - the status of the BESSY FEL Project	52
The Metrology Light Source of the PTB	53
<b>User Pages</b>	<b>54</b>
Operation Statistics	55
Improvements for Users	56
Beamlines	58
Experimental Stations	60
Board and Committees	62



Introduction

fel 06  
BERLIN

ACCEL

## Dear BESSY-users and friends,

Diamonds, glass and STARS ...

This year's Highlights appear to be shiny and sparkling. Researchers took a closer look at diamonds and glass and found that glass although breakable in our everyday experience is well suited for locking up toxic wastes in a stable, durable way for long time. Whereas blue diamonds are not only of jewellers' interest. They appear to be superconductors behaving essentially like their metal cousins, such as niobium.

Niobium is the basis of all linear accelerator (linac) modules for free electron lasers (FEL). Our FEL project received excellent marks in spring by the Wissenschaftsrat and we are eager now to build and operate the recommended two-stage cascaded FEL to demonstrate the feasibility of HGHG principle in the STARS project, the other sparkling issue. We are confident to achieve the goal since the successful operation of the Femtoslicing Source is already the first step of a cascaded FEL. In addition, recent measurements at BESSY showed for the first time that the accelerator modules can be adopted for continuous wave operation in a superconducting linac, which is also a major ingredient of our FEL project.

Sadly, our long-time member of the scientific advisory board and supporter Neville Smith will not see the BESSY-FEL up and running. He deceased after a short suffering from cancer. We will miss his advice and his companionship.

BESSY attracts many people with all different kinds of scientific and social background and we are pleased that we welcomed some 6,500 visitors during the year. Among them were visitors during the 'Lange Nacht der Wissenschaften', our Breakfast Physics during the summer holiday, delegates on a workshop on the use of Synchrotron Radiation in Arts and Archeology and our new minister of Science and Education Dr. Annette Schavan. We participated in the initiative 'Germany – Land of Ideas' showing ideas and innovation during the entire year and presented BESSY at fairs, at the 'Highlights der Physik' and at political events.



Free electron lasers have been in an one week focus during the FEL06 conference hosted by BESSY in collaboration with FZ Rossendorf in Berlin. Some 300 participants literally from all over the world discussed new developments and research opportunities during the four day conference.

The 25<sup>th</sup> users meeting in December has seen a record number of participants and poster contributions in BESSY history, reflecting the growing interest in the use of synchrotron radiation and the tremendous variety of research topics.

In 2006 all together seven prominent members of our user community and staff received calls for appointments as university professors based upon work carried out at BESSY. We would like to congratulate them and all our users for the exiting research they have been performing and we thank our staff members for their efforts and their never decreasing engagement.

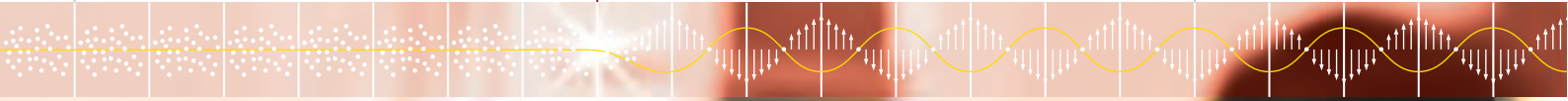
Enjoy reading the Highlights 2006.

Prof. Dr. Dr. h.c. Wolfgang Eberhardt

Thomas Frederking



Prof. Dr. Eberhard Jaeschke



Scientific Highlights

Atomic Physics	08
Magnetism	14
Surface Sciences	20
Applied Sciences	24
Material Sciences	28
Life Sciences	32
Metrology	34



## Electrons take the dress, that fits the best: The photoionization of laser-excited Li atoms

D. Cubaynes<sup>1</sup>, E. Heinecke<sup>2</sup>, M. Meyer<sup>1</sup>, T. Richter<sup>2</sup>, F. Wuilleumier<sup>1</sup>, P. Zimmermann<sup>2</sup>

<sup>1</sup> LIXAM, CNRS, Université Paris-Sud, France  
<sup>2</sup> Technische Universität Berlin

An atomic nucleus is enrobed with several layers of electronic orbitals. The inner orbitals are usually occupied by electrons, the outer ones empty. The particular shape and size of these 'dresses' is defined by the atomic potential, i.e. by the various interactions between the nucleus and the electrons. In case one of the electrons is removed from the atom by photoionization, the other electrons are most likely to stay in their orbitals. The electrons in the new ionic potential still fit to their old 'dresses'. However, in laser-excited Lithium we observed that this is not always true. Strong differences between the neutral and the ionic potential cause a mismatch of the orbitals in the neutral atom and the ion, in other words, the 'dress sizes' for the electrons change upon ionization. The electrons take the dress, that fits the best. As a result, in the photoionization of excited Lithium the electron emission is intimately connected to the promotion of another electron into a higher orbital.

To investigate this effect we use the so-called pump-probe technique, i.e. the successive absorption of two photons by the atom (Fig. 1). The first photon, here from an intense laser, is used to promote one electron to a higher orbital. In this way the atom can be prepared in a specific well-defined excited state, in other words, an electron can be inserted into another orbital modifying thereby the intra-atomic interactions in a controlled way. The second photon, here synchrotron radiation from BESSY, is then used to ionize the atoms. The combination of laser and synchrotron radiation has proven to be ideally suited for these studies [1], since the intense narrow-band laser light provides an efficient, controlled excitation process and the high-energy, tunable synchrotron radiation allows observation of photoionization in a wide range of photon energies. The modifications to the electronic cloud introduced by the laser can be evaluated by observing and analyzing the resulting differences in the photoelectron spectrum.

In the present study, we have investigated the photoionization of free Lithium atoms. Lithium has a very simple ground state configuration, Li 1s<sup>2</sup>2s, composed from only three electrons. Atoms with few electrons

exhibit a pronounced sensitivity to the displacement of one electron, making them an ideal testing ground for studies of electronic interactions. A high-resolution ring dye laser operating in a continuous wave mode at  $\lambda = 670$  nm excited first the 2s electron to the 2p shell, i.e. more precisely to the Li\*1s<sup>2</sup>2p <sup>2</sup>P<sub>3/2</sub> state. A laser power of up to 500 mW (i.e. about 10<sup>18</sup> photons/s) enabled us to excite about 20% of the Li atoms in the interaction volume. In addition, it was possible for the first time, to prepare the Li atoms in the 3p laser-excited state. This excitation requires laser photons in the more difficult to produce UV wavelength region. By frequency doubling in an external cavity up to 50 mW average power could be delivered at  $\lambda = 323$  nm and about 1% of the Li atoms were excited to the 3p <sup>2</sup>P<sub>3/2</sub> state. In the experiment, the synchrotron radiation crosses a mixture of atoms in the ground and excited state (Fig. 2) and the photoelectron spectrum is composed of both contributions. Excellent energy resolution for the exciting photon beam, provided from the UE52-SGM beamline, as well as for the electron analysis (Scienta SES-2002) is therefore prerequisite for the success of the experiments.

The relevant parts of the photoelectron spectra, recorded after the interaction of synchrotron photons of 100 eV with an effusive beam of Li atoms, are displayed in Figure 3. The spectrum in the lower part shows the photoionization of Li atoms in the ground state, i.e. with no laser light in the interaction volume. The highest intensity is found for the Li\*1s2s configuration, giving rise to two main lines, <sup>3</sup>S and <sup>1</sup>S, as the two electrons can couple their spins in the same or opposite direction. But the removal of one charge in the ionization process results in a modification of the electronic orbitals with respect to the neutral atom. There is therefore a non-negligible probability that the actual position of the outer electron corresponds to a higher (less strongly bound) shell in the ion. This gives rise to the intensity in the Li\*1s3s satellite lines at lower kinetic energies. Generally, the main lines exceed the satellites in intensity.

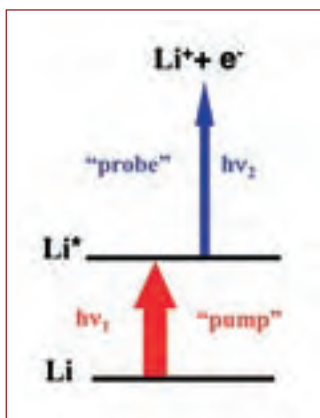


**Fig. 1:**  
 Typical two-photon pump-probe excitation scheme.

#### References:

- [1] F. J. Wuilleumier, M. Meyer, *J. Phys. B* **39**, R425 (2006).  
 [2] Z. Felfli, S. Manson, *Phys. Rev. Lett.* **68**, 1687 (1992).

Financial support by the EC through EC-IA-SFS is acknowledged.

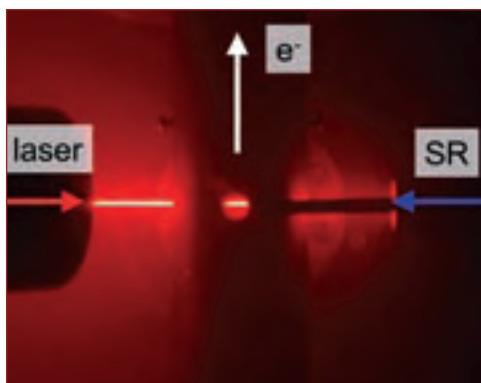


**Fig. 2:** Experimental geometry around the interaction volume. The bright white line in the center is produced from fluorescence of laser-excited Li atoms. The direction of the atomic Li beam is perpendicular to the drawing plane.

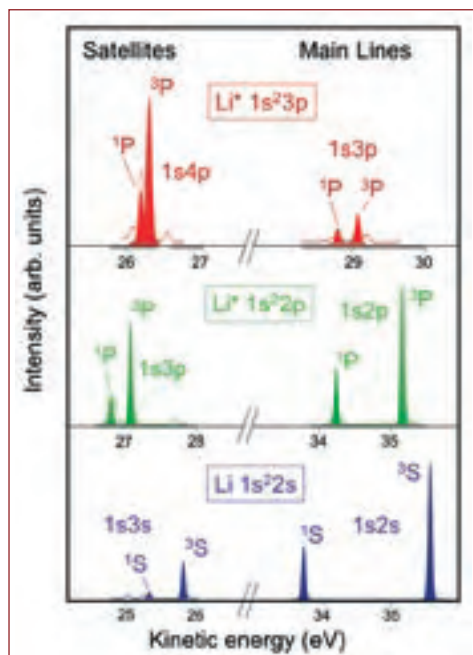


**Fig. 3:** Parts of the electron spectra recorded with 100 eV photon energy from the Li  $1s^2 2s$  ground state (bottom), the Li  $1s^2 2p$  (center) and Li  $1s^2 3p$  laser-excited state (top).

When the Li atoms are laser-excited to the  $Li^* 1s^2 2p$  state (Fig. 3, middle part) before ionization, this clear situation changes. The main line, corresponding now to the  $Li^* 1s 2p$  configuration, still comprises most of the intensity, but the relative intensity of the satellites,  $Li^* 1s 3p$  in this case, is increased matching almost the main lines.

A dramatic change, however, is observed when the 2s electron is laser-excited to the 3p shell (Fig. 3, upper part). The spectrum is now dominated by the  $Li^* 1s 4p$  satellite, caused by the shake-up of the initial 3p electron to the higher 4p orbital. The main line is now much weaker than the satellite!

It is the first time that such a strong alteration of electronic orbitals is observed in the direct photoionization process and only the preparation of the Li atom in the  $1s^2 3p$  laser-excited state provided the conditions to highlight this exceptional effect. The reason for the high satellite intensity is found in the vast mismatch of the 3p orbitals in the neutral and in the ionic state (Fig. 4). The ionization of the atom causes a spatial contraction of the wavefunctions making the 3p wavefunction in the laser-excited state very similar to the 4p wavefunction in the ion [2].

For atomic physics, the photoionization of laser-excited Li is a showcase to demonstrate fundamental principles of quantum

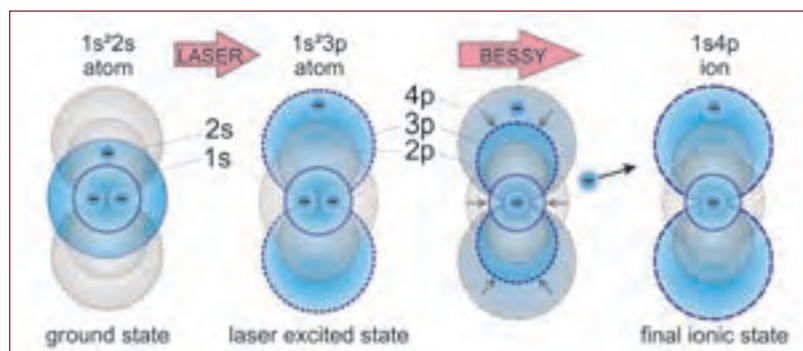


**Fig. 4:** Schematic representation of the excitation and ionization process.

mechanics, in particular the change of the radial distribution of electronic orbitals upon ionization. In a broader sense, it shows that it is not always possible to break-up a photoelectron spectrum into 'strong' main lines, arising from a direct, one-electron process, and 'weak' satellites, related to electron correlations. In more complex systems, the outer-shell of the atom can be modified by its environment, e.g. by other atoms or surfaces, and detailed knowledge of the electronic interaction is important.

**Contact:**

Michael Meyer  
michael.meyer@lixam.u-psud.fr



Hahn-Meitner-Institut  
Berlin

## Two magnetic ions join forces in multiferroics

E. Dudzik, R. Feyerherm, O. Prokhnenko, N. Aliouane, D. Argyriou

Unlike magnets, which occupy a familiar place both on the fridge and inside the computer, ferroelectrics are mainly known to experts. But the combination of ferroelectricity and magnetism has the potential to change our computers in future. It could eventually lead to ultra-high density non-volatile memory devices, capable of retaining data during power loss and with very short boot-up times.

In magnets microscopic magnetic moments appear spontaneously, which can be switched back and forth by an applied magnetic field, and thus can be used for data storage. Ferroelectric materials behave in an analogous fashion: they have a spontaneous electric polarisation which can be switched by an applied electric field. The name 'ferroelectric' does not mean that these materials contain iron – it was coined because their behaviour is so similar to that of a ferromagnet.

In a small group of materials – called multiferroics - ferromagnetism and ferroelectricity are closely entwined: their magnetisation can be switched by an electric field, and an applied magnetic field will switch their electric polarisation [1,2]. This multifunctional mix makes it possible to build a wide range of complex electronic devices, for example storage media where data can be written by applying an electric field (eliminating the need for a high writing current in a purely magnetic device), and read magnetically.

The orthorhombic rare earth manganites are one such group of materials that show a complex interplay of magnetism and electric polarisation. They contain two different magnetic ions, manganese and a rare earth metal, whose spins show several stages of magnetic ordering [3]. The following discussion is limited to the rare earth metals Terbium and Dysprosium. At room temperature these materials are paramagnetic. The first magnetic phase transition occurs at around 40 K, where the Mn moments order in a sinusoidal spin density wave whose period changes with temperature. At a second transition the Mn order locks into a helicoidal spin density wave in the bc plane of the crystal lattice. The rare earth ions order magnetically at temperatures below 10 K.

Both  $\text{DyMnO}_3$  and  $\text{TbMnO}_3$  show a spontaneous electric polarization below the intermediate lock-in transition (see Fig. 1, above). In  $\text{TbMnO}_3$  the electric polarisation sets in below 28 K, and after an initial rapid increase rises gradually towards lower temperatures. The  $\text{DyMnO}_3$  polarisation on the other hand increases rapidly below the lock-in temperature at about 16 K, reaches a maximum value which is double the Tb polarisation, and then drops to  $\text{TbMnO}_3$  levels at about 5 K. The Dy polarisation also shows a marked hysteresis at low temperatures.

The electric polarisation in  $\text{TbMnO}_3$  has been explained theoretically [4] on the basis of neutron diffraction measurements. Below the lock-in the helicoidal ordering of the Mn moments in the bc plane breaks both time reversal and spatial inversion symmetry and leads to a polarisation along the c direction (see Fig. 2).

Our experiment was motivated by the question why the temperature dependence and the magnitude of the  $\text{DyMnO}_3$  polarisation are so different from that of  $\text{TbMnO}_3$ . Dy is practically opaque for neutrons, so X-ray resonant scattering was used to study the magnetism. The experiments were carried

### References:

- [1] N. A. Hill, *J. Phys. Chem. B* **104**, 6694 (2000).
- [2] W. Eerenstein et al., *Nature* **442**, 759 (2006).
- [3] T. Goto et al., *Phys. Rev. Lett.* **92**, 25721 (2004).
- [4] M. Mostovoy, *Phys. Rev. Lett.* **96**, 067601 (2006).
- [5] R. Feyerherm, *Phys. Rev. B* **73**, 180401(R), (2006).
- [6] O. Prokhnenko et al., *Phys. Rev. Lett.*, in press

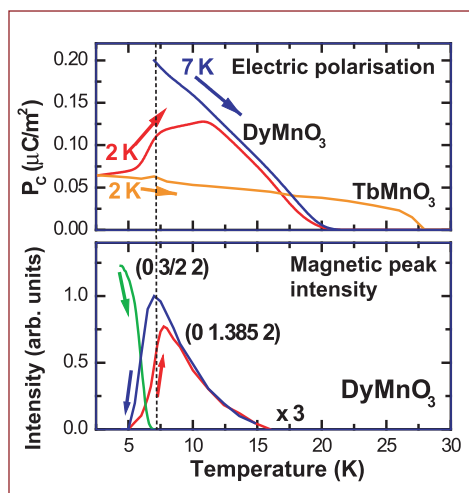


**Fig. 1:**  
Above: electric polarisation in  $\text{TbMnO}_3$  and  $\text{DyMnO}_3$  (after Goto et al. [3]). Below: Magnetic diffraction peak intensities in  $\text{DyMnO}_3$ .

out at the new high-energy MAGS beamline operated by the Hahn-Meitner-Institute at BESSY. Samples were cooled in a closed-cycle cryostat mounted on a six-circle diffractometer. Measurements were done both at the Dy  $L_3$ -edge at 7,790 eV and non-resonant at 12,398 eV.

X-ray resonant scattering clearly shows the three stages of magnetic ordering (Fig. 3). Below the Neel temperature of 40 K, the Mn orders in a sinusoidal spin wave with a propagation vector  $\tau_{\text{Mn}}=0.385 b^*$  in reciprocal space. Although the diffraction peaks from the Mn magnetic order could not be observed directly, we found second order diffraction peaks which are due to a structural distortion associated with the Mn order at positions  $k \pm 2\tau_{\text{Mn}}$  (Fig. 3, red inset). These second order peaks appear, because the magnetic order distorts the crystal unit cell. This distortion has half the period of the magnetic ordering (Fig. 4).

These peaks persist below the lock-in transition at 16 K. At the lock-in, a second set of diffraction peaks appear at positions  $k \pm \tau_{\text{Mn}}$  (Fig. 3, orange inset), which are resonant at the Dy  $L_3$  edge. Linear polarization analysis shows that these peaks are of magnetic origin. This shows that in the lock-in regime, where the spontaneous electric polarization appears, the Dy moments have ordered with the same periodicity as the Mn.

At temperatures below 4.35 K the Dy moments order independently of the Mn. This leads to the collapse of the magnetic diffraction peaks at  $k \pm \tau_{\text{Mn}}$  and the appearance of magnetic peaks with a period of  $\tau_{\text{Dy}}=0.5 b^*$  (Fig. 3, blue inset). As in the case for the Mn, these magnetic diffraction peaks are found to be associated with a second order structural distortion. These peaks should appear exactly at integer order positions, but instead are found at peak positions of  $q = 0.905 b^*$ . It appears that competition with the persisting Mn order shifts both the Dy and the Mn second order structural peaks slightly from their expected positions towards one another [5].

The transition from the independent Dy magnetic order to the induced order above the Dy Neel temperature shows a strong hysteresis (Fig. 2 below). This hysteresis coincides in size and temperature dependence with the hysteresis in the Dy electric polarisation shown in the upper part Fig. 2. Therefore we argue that in the lock-in regime, where the Dy moments order with the same periodicity as the Mn, the Dy moments contribute to the

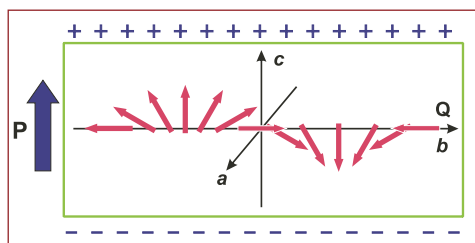


**Fig. 2:** Helicoidal magnetic order can induce an electric field in a crystal that is perpendicular to the magnetic propagation vector.

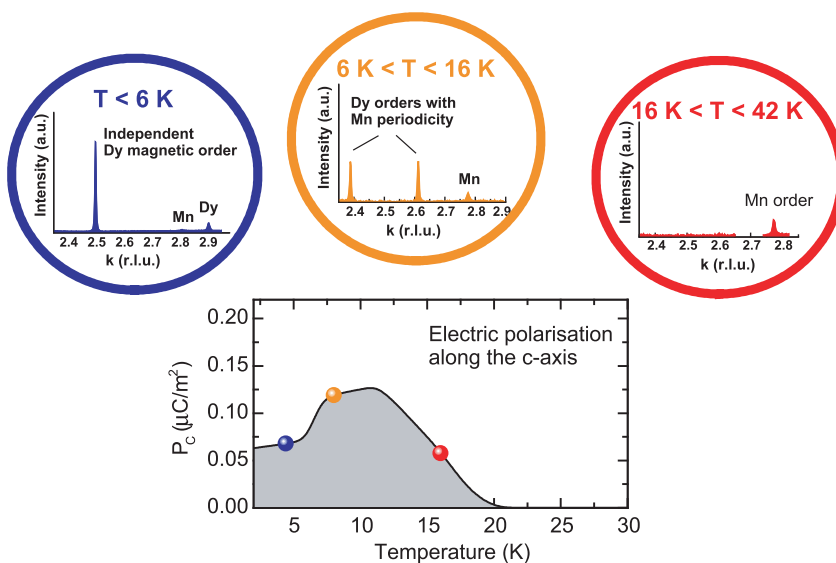


**Fig. 3:** Electric polarisation in DyMnO<sub>3</sub> shown with the X-ray diffraction data for high, intermediate and low temperatures (red, orange and blues insets, respectively).

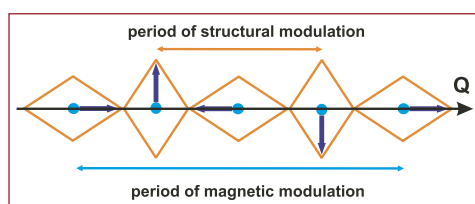


**Fig. 4:** A magnetic modulation can distort the crystal structure. When the period of this structural distortion is half that of the magnetic modulation, it leads to second order diffraction peaks.

electric polarisation. Thus the increase in polarisation above the Tb value shown in Fig. 2 between 4.35 and 16 K appears to be due to a contribution from the Dy moments. Surprisingly, the two magnetic moments situated at completely different positions in the unit cell combine to induce an electric polarisation as if they simply sum up [6]. This idea is supported by the fact that in TbMnO<sub>3</sub> in the ferroelectric phase the Tb moments order along a different direction from the Mn, and so cannot contribute to the electric polarisation.

**Contact:**

Esther Dudzik  
dudzik@hmi.de



## Melting the antiferromagnetic ice sheet

J. Goedkoop<sup>1</sup>, S. Konings<sup>1</sup>, Ch. Schüßler-Langeheine<sup>2</sup>,  
H. Ott<sup>2</sup>, E. Schierle<sup>3</sup>, E. Weschke<sup>3</sup>

1 University of Amsterdam,  
Netherlands  
2 Universität zu Köln  
3 Freie Universität Berlin

Polar bears and physicist share a strong interest in phase transitions. Polar bears take the real world irregularities that cause their ice flow to break up in fixed frozen and more dynamic molten parts rather stoically. For physicists however, who like to think in terms of ideal ordered systems, real world disorder is just bad news. Pet theories like critical scaling, which describe the divergence of the size of fluctuations at phase transitions, break down in the presence of disorder. Take for instance thin films, where structural disorder can never be avoided. As a result, magnetic phase transitions in such films are difficult to understand, a situation that is quite disturbing in view of the importance of such films in science and technology.

To oversee the battle between order and fluctuations in phase transitions and to understand the role of structural disorder in this fight requires a tool that covers a huge range of length- and timescales. While the length scale of fluctuations can be readily probed by conventional diffraction experiments, the observation of the corresponding fluctuation times is much more challenging. As we will show here, coherent soft X-rays turn out to provide a remarkably powerful looking glass for this purpose.

As a test case, we studied an epitaxially-grown ultrathin 11-monolayer holmium film displaying a helical magnetic order with a periodicity along the surface normal [1]. This order disappears in a broad transition around  $T_N=76$  K. In the experiment the coherence of the light of the beamline (U49-2 PGM 1 and UE46 PGM) is obtained by a spatial filter consisting of two pinholes (Fig. 1). The periodic helical magnetic structure produces strong magnetic diffraction peaks, when the photon energy is tuned to the  $M_E$  resonance of holmium. One these peaks we intercept with a CCD camera. In this way we can observe the melting of the magnetization, much like polar bears watch the ice melt under their feet. Unlike the polar bears however, we can regulate the temperature in our experiment within 10 mK and in this way control the magnetic correlation length  $\xi$ , the typical length scale over which the sample is magnetically ordered. With incoherent light we would observe one smooth diffraction peak, with a width that is inversely proportional to the correlation length of the ordered regions. As expected, we find that the closer we approach the transition temperature  $T_N$ , the smaller is the scattered intensity (Fig. 2). The correlation length also decreases, although in a way

that is quite different from standard models. What is happening here? In order to find out we make our light coherent and study the fluctuations in the time domain.

When coherent light is used, the magnetic peak breaks up in a myriad of speckles, which form the diffraction pattern of the magnetic structure of the illuminated spot. Any changes in this structure

are immediately reflected in changes in the speckle pattern. By recording the speckle-pattern as a function of time and performing a time correlation analysis of the speckle intensities it is possible to extract the correlation time of the fluctuations.

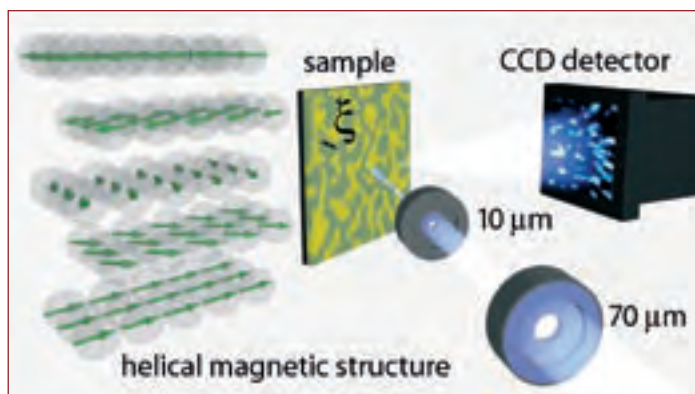


**Fig. 1:** Sketch of the coherent diffraction experiment and the helical magnetic structure of holmium. The length scale over which the magnetic structure is ordered in the plane of the sample is depicted by the correlation length  $\xi$ .

### References:

- [1] H. Ott et al., *Phys. Rev. B* **74**, 094412 (2006).
- [2] B.J. Berne and R. Pecora, *Dynamic Light Scattering with Applications*, John Wiley (1976).
- [3] G. Grübel and F. Zontone, *J. Alloy. Compd.* **362**, 3 (2004).
- [4] D.O. Riese et al., *Phys. Rev. Lett.* **85**, 5460 (2000).
- [5] I. Sikharulidze et al., *Phys. Rev. Lett.* **88**, 115503 (2002).
- [6] <http://www.science.uva.nl/research/cmp/goedkoop/group/docs/fluctuations/fluc2.html>.
- [7] Stephen D. Kevan, *Personal communication*.

### Acknowledgements:

The authors are indebted to H. Zabel for making excellent samples. Funded by EU, the DFG through SFB 608 and FOM/NWO (Netherlands).

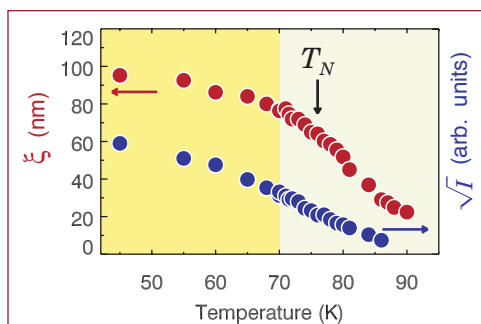


**Fig. 2:** Temperature dependence of the correlation length  $\xi$  and intensity  $I$ . The fluctuations could be measured in the time domain up to 70 K.

This technique is called Photon Correlation Spectroscopy [2] which is well known from laser light scattering where, among other things, it is used to study diffusion in colloidal systems. With the availability of brilliant X-ray sources, this laser technique has started to make inroads into the X-ray regime [3], where the fluctuations can be measured to much smaller correlation lengths. So far, only soft condensed matter systems have been probed such as colloids [4] or smectic films [5].

Here we use the technique to follow correlations in a hard condensed matter system, namely the magnetic fluctuations in our film. Fig. 3 shows one of the speckle patterns with an exposure time of 4 seconds together with snapshots of the 3-hour speckle movies, some of which can be viewed online [6]. From these it is clear that at 50 K the magnetic structure is fixed, but that at higher temperatures fluctuations appear that speed up dramatically.

Moreover, when all images in a movie taken at a fixed temperature are averaged, we find something remarkable. At 50 K, the intensity profile has a contrast close to a single speckle pattern of 4 s exposure, confirming a frozen domain structure (Fig. 4). At 70 K the intensity profile blurs out, but still some fixed speckles remain. This proves that the magnetic fluctuations are highly constrained by the defect structure of the film. In more technical terms, the system is said to be non-ergodic.

Although there are some important differences, this transition is analogous to the melting of ice, in which the correlation length of the ordered ice phase (e.g. the ice floes) will be reduced when the temperature increases. The limited coherent flux binds us at present to the ultra slow regime, between 4 seconds and 3 hours. From an intensity correlation analysis we find that this time regime corresponds to the fluctuation times in our sample at temperatures below roughly 70 K.

This is the first time such magnetic correlations have been followed not only in the space but simultaneously in the time

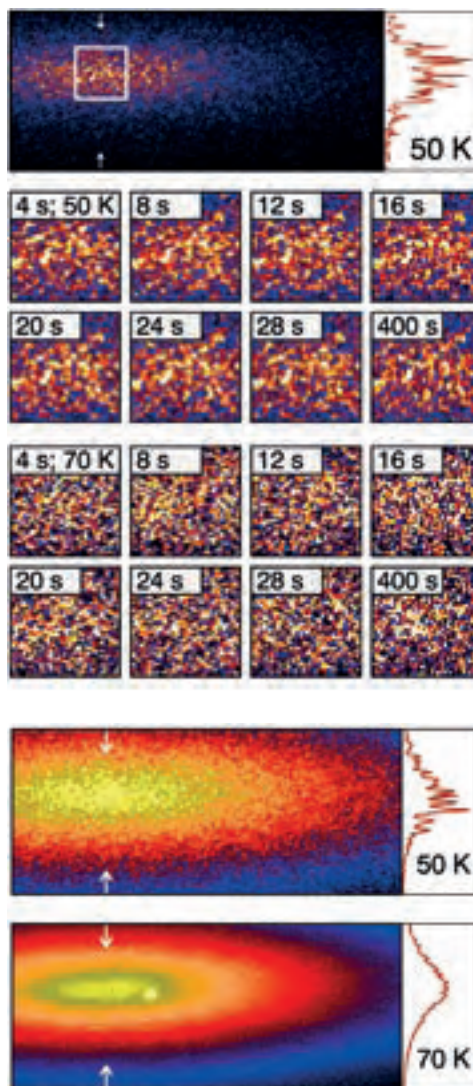


**Fig. 3:** Top: speckle pattern at 50 K. Below: examples of 4 s exposures acquired at the indicated time in the area marked in the top panel at 50 K (top rows) and at 70 K (bottom rows), showing the fluctuations in the speckle pattern that reflect the fluctuations in the magnetic structure. At 50 K the speckle pattern is almost completely static but is fluctuating rapidly at 70 K (6 K below the film's ordering temperature).

**Fig. 4:** Intensity profile obtained by averaging over 2,200 speckle patterns acquired over about three hours.

domain. The movies undoubtedly show that the strange behavior of the correlation length is not only due to the reduced dimensionality of the film, but also due to real world defects. The challenge now is to determine the temperature-dependent ratio of the dynamic to static parts of the sample in this magnetic system. Meanwhile beckoning on the horizon are the plethora of correlated electron systems showing stripes, charge and spin density waves or other long range order effects which may or may not be dynamic in nature. With the 1,000 times higher coherent flux that can be expected at optimized beamlines [7] or the  $10^9$  times higher flux provided by X-FELs, the future for this technique looks excellent.

**Contact:**

Jeroen Goedkoop  
Goedkoop@science.uva.nl

Source: Juan Salmotal Franco



## Filling the seats: Atomic-scale roughness of antiferromagnetic films

W. Kuch<sup>1</sup>, L. I. Chelaru<sup>2</sup>, F. Offi<sup>2</sup>, J. Wang<sup>2</sup>, M. Kotsugi<sup>2</sup>, J. Kirschner<sup>2</sup>

<sup>1</sup> Freie Universität Berlin

<sup>2</sup> Max-Planck-Institut für  
Mikrostrukturphysik, Halle

Saturday afternoon: The first supporters arrive and fill the stand, but this stadium has peculiar rules. On the orange seats women and men are seated in a strict alternating order, while the blue stand has to be filled with either only men or only women. The gender of the supporters in the blue seats has to be selected such that at the interface between the orange and blue seats preferably couples of men and women are placed. This makes the filling of the seats an interesting problem, which very much depends on the details of how the border line between orange and blue exactly runs. This is pretty much the situation of the interaction at the interface in a stack of ferro- and antiferromagnetic films. These multilayers are important ingredients of many devices like hard disk read heads, magnetic sensors, or magnetic random access memories [1,2]. Their widespread use in commercial applications is, however, not paralleled by a detailed fundamental understanding of the interaction between antiferromagnetic and ferromagnetic materials. While in ferromagnets all the atomic magnetic moments are pointing in the same direction (i.e. are all male or female in the stand), the magnetic order in antiferromagnets is more complex. In antiferromagnets the atomic moments align such that the total moment vanishes if averaged over a few neighbor atoms. In the simplest ones every other atom has its spin pointing into the opposite direction. To achieve understanding of the magnetic interaction between an antiferromagnetic and a ferromagnetic material, it is thus vital to characterize and control the interface structure and roughness on the atomic level.

We used the technique of magnetic domain imaging by x-ray magnetic circular dichroism photoelectron emission microscopy (XMCD-PEEM) [4] to study the dependence of the magnetic interface coupling on thickness and layer filling of both the ferromagnetic and antiferromagnetic films [3]. The absorption of circularly polarized synchrotron radiation from the elliptic undulator beamline UE56-2 PGM 2 was used to obtain magnified images of the sample by means of the emitted secondary electrons. In these images, regions of different intensity represent different magnetization directions. The XMCD

effect occurs only in resonance at elemental absorption lines, thus magnetic domain images of different layers at different depths of the single-crystal heterostructures can be acquired separately if they contain different elements. Crossed-wedge samples, in which the thickness of a ferromagnetic and an antiferromagnetic layer vary along perpendicular directions, were prepared, and allow the simultaneous visualization of the magnetic coupling as function of two different layer thicknesses.

Fig. 1 shows an example of a trilayer on a Cu(001) substrate in which antiferromagnetic FeMn is sandwiched by two ferromagnetic layers, a Co layer at the bottom, and a Co/Ni hybrid layer at the top. Panel (a) shows a sketch of the wedge geometry. The thickness of the bottom Co layer (blue) increases from left to right up to 8 atomic monolayers (ML), and then stays constant. The thickness of the antiferromagnetic FeMn layer (red) varies from bottom to top. Panel (b) shows the magnetic domain image of the as-grown Co bottom layer, panels (c) and (d) the domain images obtained at the Co and Ni absorption resonances, respectively, after deposition of the complete structure. Because both the bottom and top ferromagnetic layers contain Co, image (c) is a superposition of the magnetic domain patterns (b) and (d), while panel (d) represents the top layer only. Alternating regions of parallel and antiparallel coupling across the FeMn layer are indicated by couples of parallel and antiparallel arrows in (c). They alternate with a 2-ML period as a function of FeMn thickness, but also exhibit an interesting saw-tooth-like behavior on the thickness of the bottom Co layer. The latter represents the dependence on the interface morphology. It is modulated by the thickness, and hence the atomic layer filling, of the bottom Co layer.

From these measurements and supporting magneto-optical Kerr effect experiments, the following picture could be deduced [3]: First, to have a significant magnetic interaction between the ferromagnetic and the antiferromagnetic layers, steps of single atom height at the interface are required. Perfectly flat regions do not contribute. This follows from

### References:

- [1] G. A. Prinz et al., *Science* **282**, 1660 (1998).
- [2] S. A. Wolf et al., *Science* **294**, 1488 (2001).
- [3] W. Kuch et al., *Nature Mater.* **5**, 128 (2006).
- [4] J. Stöhr et al., *Science* **259**, 658 (1993).
- [5] W. Kuch et al., *Phys. Rev. Lett.* **92**, 017201 (2004).
- [6] J. C. Slonczewski, *Phys. Rev. Lett.* **67**, 3172 (1991).
- [7] F. Offi et al., *Phys. Rev. B* **66**, 064419 (2002)

### Acknowledgments:

We thank B. Zada and W. Mahler of the UE56-2 beamlines for their help.

Supported by the BMBF

the absence of  $90^\circ$  coupling, which would otherwise be expected at FeMn thicknesses close to  $n + 0.5$  ML thicknesses with  $n$  an integer number [6]. Also the influence of the Co bottom layer thickness on the sign of the coupling is not compatible with flat regions being the dominant source of the antiferromagnet/ferromagnet coupling. Second, the coupling is higher if these monatomic steps are laterally confined at small islands. Larger islands or elongated steps mediate a weaker coupling. The strength of the coupling can only be deduced from the Kerr measurements.

The observed saw-tooth pattern is surprising. The interface roughness has maxima at around 50% atomic layer fillings and decreases towards both sides, for higher and lower fillings, leading to the sine-like oscillations typically observed in the diffracted electron intensity [7]. In the present case, however, a 20% filling is completely different from an 80% filling, although the number of monatomic steps and thus the roughness may be equal. This leads to the third conclusion, that the amount of antiferromagnetic material needed to complete the outmost atomic layer of the ferromagnets is not contributing to the sign of the coupling.

The coupling is mediated by uncompensated spins of the antiferromagnet at monatomic step edges at the interface. A sketch of a possible interface spin configuration at such a monatomic step edge is shown in Fig. 2. Black and gray bullets with arrows represent atomic moments of next-level atomic planes of the non-collinear antiferromagnetic spin structure [5] of FeMn. Ellipses at the step edges indicate regions in which the antiferromagnetic spins do not cancel, but follow the magnetization direction  $M_{\text{FM}}$  of the ferromagnetic layer. These uncompensated atomic moments are responsible for the magnetic coupling to the ferromagnet.

Our results indicate that, in general, the interface coupling can be enhanced by the controlled incorporation of atomic-level roughness features with small lateral size. This would be like designing the border line between the orange and blue seats in the stadium in a particular rough zig-zag shape such as to provide a very clear-cut decision about the gender of the supporters in the blue stand. With the forthcoming advent of atomic-scale manipulation in nanotechnology, this may be a feasible way to controllably modify the coupling strength in ferromagnetic–antiferromagnetic systems.

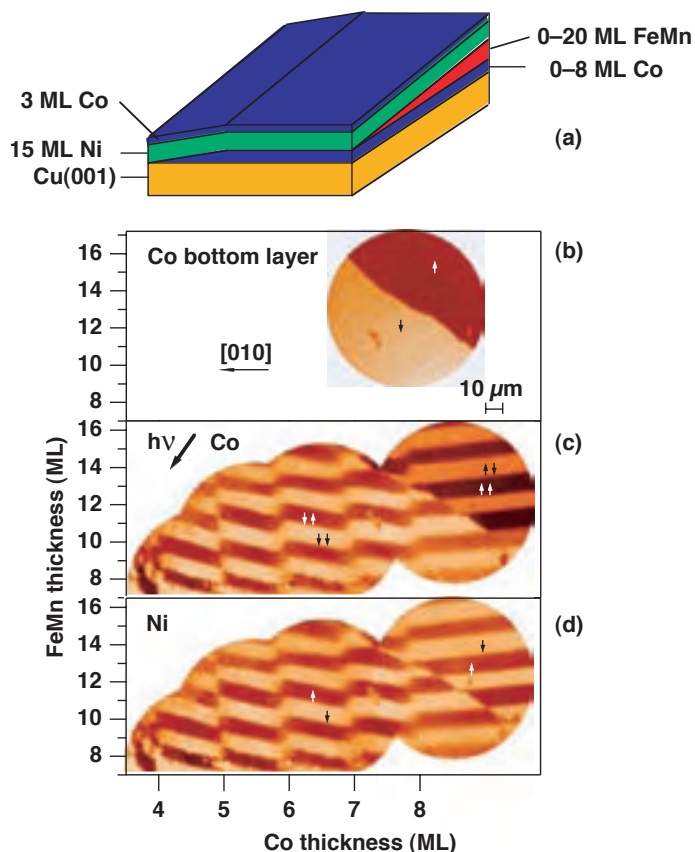


**Fig. 1:**  
**(a):** Geometry of a crossed double-wedge sample. Antiferromagnetic FeMn of varying thickness is sandwiched between ferromagnetic layers consisting of Co at the bottom and Co/Ni at the top.  
**(b):** Domain pattern of the Co bottom layer. Bright and dark regions correspond to magnetization direction down and up, respectively.  
**(c):** Element-selective domain image of the complete sandwich structure, acquired at the Co  $L_3$  edge. Bright and dark regions result from a superposition of magnetization directions of Co in the bottom and top layer, indicated by couples of arrows.  
**(d):** Element-selective domain image of the top layer, acquired at the Ni  $L_3$  edge. Bright and dark regions correspond to magnetization direction down and up, respectively.

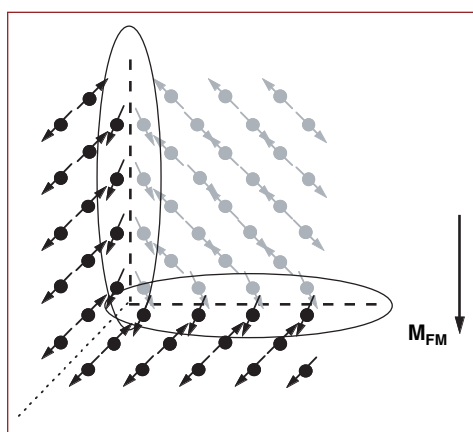
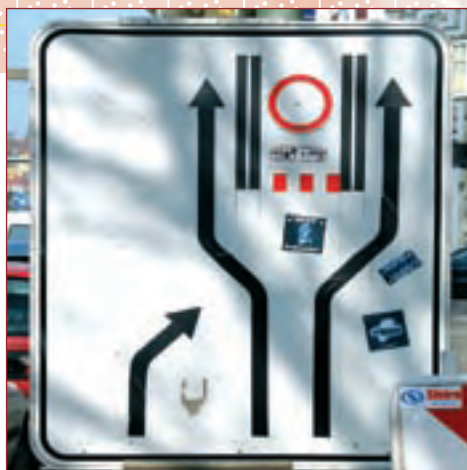


**Fig. 2:**  
**Sketch of a possible interface spin structure of the antiferromagnetic FeMn layer. Uncompensated atomic moments at monatomic step edges (ellipses) mediate the magnetic coupling to an adjacent ferromagnetic layer.**

**Contact:**

Wolfgang Kuch  
 kuch@physik.fu-berlin.de

Kai Godehusen



## Peer pressure among electrons: How localized and itinerant states interact

Yu. S. Dedkov<sup>1</sup>, M. Fonin<sup>2</sup>, Yu. Kucherenko<sup>3</sup>, S. Molodtsov<sup>1</sup>,  
U. Rüdiger<sup>2</sup>, C. Laubschat<sup>1</sup>

1 Technische Universität Dresden  
2 Universität Konstanz,  
3 Institute for Metal Physics,  
Kiev, Ukraine

Sometimes the world of atoms behaves very human: Magnetism is a collective phenomenon where the spins of electrons are oriented in the same direction. This is possible in a solid state where all atoms share the outermost electrons to build a band. In contrast to this concept are rare earth (RE) atoms, whose outermost  $4f$  shell is actually very close to the core and therefore more like in a single atom [1]. The question arises, whether an individual ( $4f$ ) electron can change the behavior of the group (band magnetism) and vice versa? Talking about people, the reaction could be manifold, i.e. a certain glance is enough to cause a reaction. For the atoms one has to consider electrons which hop between the localized ( $4f$ ) orbital and the valence band (group).

The magnitude of the hopping probability depends on the hybridization matrix element and the density of valence-band states. Both quantities are usually large in RE transition metal systems. Here, the magnetic properties depend not only on the localized  $4f$  moments, but also on itinerant  $d$  states that form exchange-split bands with different densities of states for different spin orientations [2]. One would expect, that the hopping probabilities and, thus, the magnetic properties of the  $4f$  states vary also as a function of spin orientation. Although this idea is rather transparent, such an effect has not been discussed to our knowledge in the literature so far, even so it might have severe consequences for the understanding of magnetic anomalies in these compounds.

Ce, the first element of the RE series, is subject of strongest interactions between  $4f$  and valence-band states. Here we report on a spin- and angle-resolved resonant photoemission (PE) study of an ordered Ce monolayer on Fe(110) (inset in Fig. 1) at the Ce  $4d \rightarrow 4f$  absorption threshold. The experiments were performed with a hemispherical PHOIBOS 150 electron-energy analyzer combined with a 25 kV mini-Mott spin detector using synchrotron radiation from UE112 PGM 1 beamline of BESSY. Application of resonant PE is necessary for a proper discrimination of the Ce  $4f$  and valence-band emissions.

PE spectra were taken on- and off-resonance at 121 eV and 112 eV photon energies, respectively, in normal emission geometry. In order to extract the pure Ce  $4f$  contributions from these spectra, the off-resonance data were subtracted from the on-resonance spectra after proper normalization of the intensities. The resulting spin-resolved  $4f$  spectra are shown in the upper part of Fig. 2 together with the corresponding spin polarization  $P$  (inset) defined as  $P = (N^\uparrow - N^\downarrow) / (N^\uparrow + N^\downarrow)$ , where  $N^\uparrow$  and  $N^\downarrow$  denote the intensities of the majority (spin up) and minority (spin down) channels, respectively. The spectra reveal a double-peak structure of the Ce  $4f$  emission consisting of a main maximum at 2.2 eV corresponding to the ionization peak expected from the unhybridized  $4f^1$  ground state and a hybridization peak at the Fermi level,  $E_F$ . From the weak intensity of the latter relative to the ionization-peak signal, a weak hybridization similar to the one in  $\gamma$ -Ce may be concluded as it is expected for a Ce surface layer [3]. Its intensity with respect to the ionization peak is, thus, a measure of the magnitude of the hopping probability and is expected to vary with spin orientation if the interaction depends on the latter. The most important observation is, however, that the intensity of the hybridization peak is larger for the minority- than for the majority-spin component (Fig. 2) indicating larger  $4f$  hybridization of the former. The spin polarization of both, the ionization and the hybridization peaks, gives a negative sign in  $P$  revealing that the preferred orientation of the Ce  $4f$  spins is opposite to the magnetization direction of the Fe layers.

In order to simulate the observed variation of  $4f$  hybridization as a function of spin orientation we used a simplified approach to the periodic Anderson model (PAM) that was recently successfully applied to explain the angle-resolved photoemission spectra of CePd<sub>3</sub> and Ce/W(110) [4, 5]. In this approach double occupation of the  $4f$  states is ignored (on-site  $f$ - $f$  Coulomb interaction energy,  $U_{ff} \rightarrow \infty$ ) and electron momentum conservation upon hybridization is assumed. For the hybridization matrix element we used calculated  $f$ -projected local expansion coefficients of the Bloch functions around the

### References:

- [1] H. R. Kirchmayr and C. A. Poldy, in **Handbook on the Physics and Chemistry of Rare Earths**, vol. 2 (North-Holland, Amsterdam, 1978).  
[2] O. Gunnarsson and K. Schönhammer, *Phys. Rev. Lett.* **50**, 604 (1983).  
[3] E. Weschke et al., *Phys. Rev. B* **44**, 8304 (1991) and references therein.  
[4] S. Danzenbächer et al., *Phys. Rev. B* **72**, 033104 (2005).  
[5] D. V. Vyalikh et al., *Phys. Rev. Lett.* **96**, 026404 (2006).

### Acknowledgements:

This work was funded by the DFG, SFB 463, Projects TP B4 and TP B16, and the BMBF.

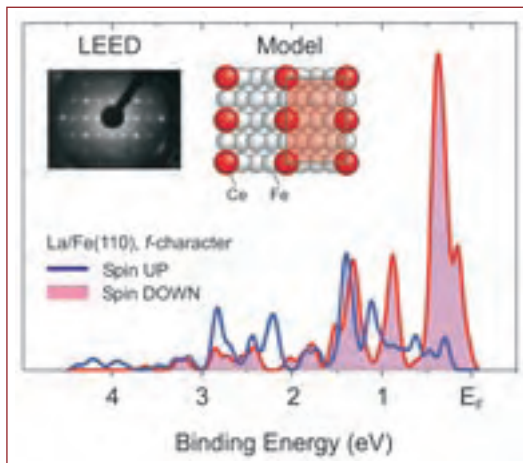


**Fig. 1:** Results of spin-polarized band structure calculations for an ordered monolayer of La on top of Fe(110) surface. Inset shows the diffraction image for the Ce/Fe(110) system and the structural model obtained after simulations of LEED.

rare-earth sites. Respective energy distributions of these coefficients at the  $\Gamma$  point were taken from a band-structure calculation of the system, in which Ce was replaced by La in order to exclude contributions of localized Ce  $4f$  orbitals (Fig. 1). Since these  $f$ -contributions are formed by linear combinations of wave functions of the neighboring atoms (mainly Fe  $3d$ ) penetrating into the La atomic spheres, they reflect to some extent the energy and spin distribution of the latter and are rather different for majority- and minority-spin electrons. On the basis of these data spin-resolved Ce  $4f$  PE spectra were calculated using the energy of the unhybridized  $4f$  state and a hybridization constant as the only adjustable parameters. The results are presented in Fig. 2 (lower panel): The energy distribution of the PE intensity agrees well with that of the experimental spectra (Fig. 2, upper part). The minority-spin spectrum reveals high intensity of the hybridization peak due to the large density of the  $4f$  minority-spin contributions close to  $E_F$ . On the contrary, no hybridization peak is obtained for the majority spin-direction due to an energy gap at the Fermi level for the respective valence-band states (Fig. 1). This particular result deviates from the experiment where a reduced but finite hybridization peak was observed. The deviation may be ascribed to the finite angle resolution of the experiment that samples also regions in reciprocal space where majority-spin bands cross  $E_F$ . The calculated spin polarization (Fig. 2, inset in the lower part) reproduces qualitatively the energy dependence of the measured polarization. Particularly good agreement is obtained for points where the spin polarization changes its sign.

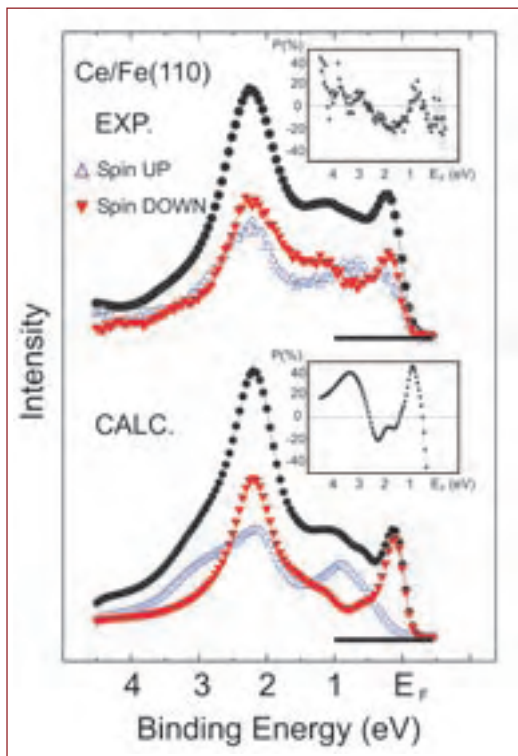
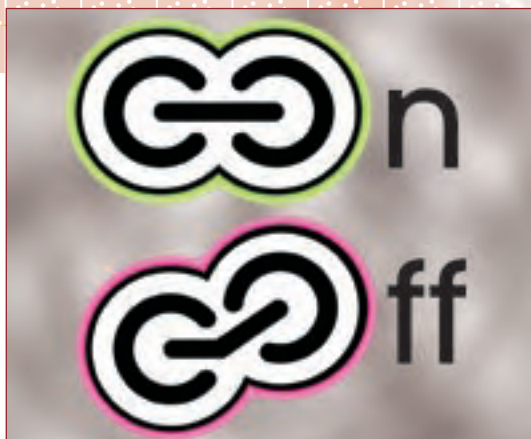


**Fig. 2:** Spin-resolved experimental (upper part) and calculated (lower part) Ce  $4f$  emission for Ce/Fe(110). Total, majority- and minority-spin photoelectron intensities are shown by solid circles, open and solid triangles, respectively. The insets show the corresponding spin polarization  $P$ .

**Contact:**

Yu. S. Dedkov  
dedkov@  
physik.phy.tu-dresden.de



## On or Off? Identifying isomerisation in molecular switches

P. M. Schmidt<sup>1</sup>, R. Püttner<sup>2</sup>, C. Kolczewski<sup>1</sup>, K. Hermann<sup>1</sup>, K. Horn<sup>1</sup>,  
T. U. Kampen<sup>1</sup>

<sup>1</sup> Fritz-Haber-Institut  
der Max-Planck-Gesellschaft,  
Berlin  
<sup>2</sup> Freie Universität Berlin

The phenomenal rate of increase in the integration density on semiconductor micro-chips is driven by advances in optical lithography, that is, the process used for patterning in microelectronic device fabrication. Although the introduction of shorter-wavelength light sources and resolution enhancement techniques helps to maintain the current rate of device miniaturization, at some time in the near future this top-down approach can no longer attain the required feature sizes.

Among several alternative techniques for the future, promising results have been obtained by the use of molecular systems [1]. Here, the advantages are easy fabrication and the possibility to shape and fine-tune organic molecules into desired structures by organic synthesis. Molecules with an extended  $\pi$ -electron system are especially promising candidates. Intermolecular interactions of the  $\pi$ -systems favor a stacking of molecules with their aromatic planes parallel to each other. In such highly ordered thin films, overlap between  $\pi$ -orbitals takes place only in one direction leading to an anisotropy of optical and physical properties, i.e. charge carrier mobility or optical absorption [2, 3].

A further advantage of organic materials is that the smallest building block, the molecule itself, represents an entity with a certain functionalization. For example, a molecule with two different possible conformations incorporated into one-dimensional 'molecular wires' would ideally serve as a 'molecular switch' (Fig. 1) The simplest model switch of this sort is the stilbene molecule (1,2-diphenylethylene) for which the phenyl groups can be arranged in two conformations, on the same side or on opposite sides around the central C=C bridge, i.e. to cis- and trans-stilbene, respectively (Fig. 1). This isomerisation can be triggered by UV irradiation as already shown by experiment and explained theoretically for the gas phase and in solution [5, 6, 7, 8].

Our goal is to find a spectroscopic fingerprint for the two isomers on the surface corresponding to the 'on' or 'off' position of this molecular nano-switch (Fig. 1). For molecular switching to be useful in microelectronics the switching pathway has to work on surfaces,

i.e. in a constrained situation. However, the bonding with the substrate surface must not hinder the switching process. This is possible for adsorbed stilbene since bonding to a surface via the central C=C double bond seems to be most favorable with the phenyl rings allowed to rotate freely.

To identify changes in the molecule due to the adsorption on the surface, we have taken Near Edge X-Ray Absorption Fine Structure Spectroscopy (NEXAFS) spectra from the molecule in the gas phase (i.e. prior to adsorption) and in the adsorbed phase on the surface accompanied by theoretical calculations (Fig. 2.). NEXAFS is an element-specific and surface sensitive method. Using angular-dependent measurements the geometry of the adsorbed molecules can be determined. Thus,  $\sigma^*$ -orbitals of the molecular backbone and  $\pi^*$ -orbitals can be probed selectively.

NEXAFS spectra of trans- and cis-stilbene in the gas phase (Fig. 3), show a prominent  $\pi^*$ -resonance between 284 and 286 eV photon energy and several smaller  $\sigma^*$ -resonances at higher photon energies [12]. The  $\sigma^*$ -resonances are found to be quite comparable (with only minor differences) due to the isomers possessing the same backbone. The  $\pi^*$ -resonance, on the other hand, shows significant differences. While the cis-isomer displays a single sharp peak, the  $\pi^*$ -resonance of trans-stilbene is split. Theoretical studies obtained by transition potential calculations with corrections for the ionization potential and relativistic effects

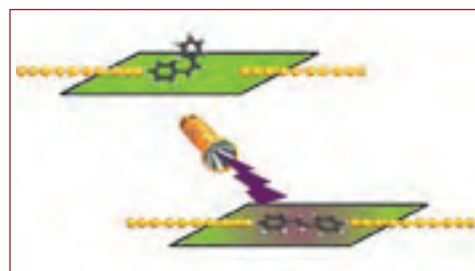


**Fig. 1:**  
Basic concept of an optically activated molecular switch.

### References:

- [1] R.L. Carroll, et al., *Angew. Chem. Int. Ed.*, **41**, 4378 (2002).  
[2] M. Friedrich et al., *J. Phys.-Condes. Matter*, **15**, S2699 (2003).  
[3] T.U. Kampen et al., *Appl. Surf. Sci.*, **212-213**, 501 (2003).  
[5] V.D. Vachev, et al., *Chem. Phys. Lett.* **215**, 306 (1993).  
[6] R.J. Sension, et al., *J. Chem. Phys.*, **98**, 6291 (1993).  
[7] J.S. Baskin, et al., *J. Phys. Chem.*, **100**, 11920 (1996).  
[8] W. Fuß, et al., *Angew. Chem. Int. Ed.*, **43**, 4178 (2004).  
[9] P.M. Schmidt, et al., *Surf. Sci.* (2007), doi:10.1016/j.susc.2007.01.044  
[10] The program package StoBe is a modified version of the DFT-LCGTO program package DeMon, originally developed by A. St-Amant and D. Salahub (University of Montreal), with extensions by K. Hermann and L.G.M. Pettersson.

### Acknowledgements:

Supported by the SONS-program (MOL-VIC) of the European Science Foundation (ESF).

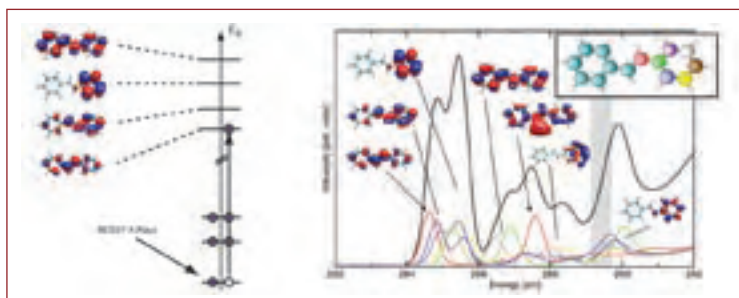
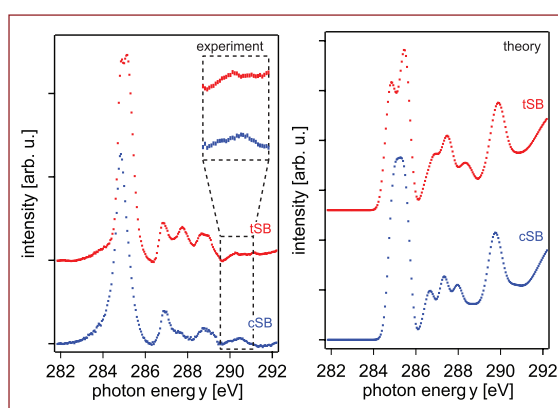


**Fig. 2:** Calculated NEXAFS spectrum of trans-stilbene showing the contribution of each carbon to the overall spectrum. For some peaks the corresponding final states orbitals are shown.

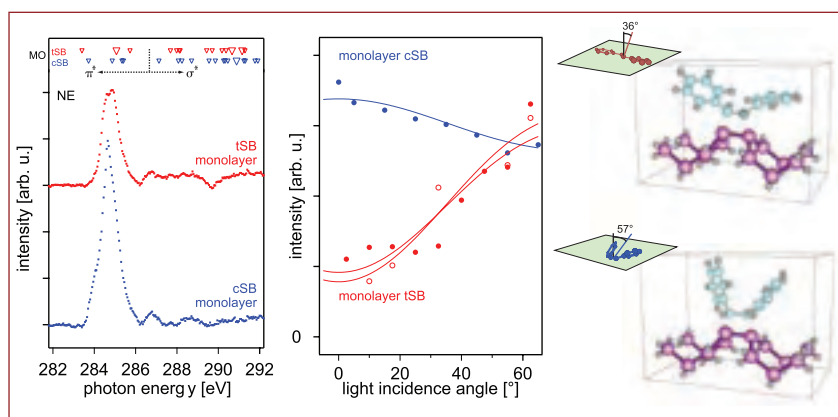
using the StoBe code [13] confirm all spectral features observed in the experiment. In particular, the also  $\pi^*$ -resonances are very well reproduced by the calculations; this can be used to clearly identify both isomers. For higher photon energies the calculations predict stronger signal intensities than found in the experiment. This may be due to the use of stronger broadening in the calculated intensities above the ionization threshold.

Figure 4 shows NEXAFS spectra recorded for a monolayer of cis- and trans-stilbene. The intensity curves to the right refer to the  $\pi^*$ -resonance for different photon incidence angles. The key features distinguishing between the isomers in the gas-phase spectra are also visible in the spectra of the adsorbed phase. The trans-isomer displays a split  $\pi^*$ -resonance while that of the cis-isomer is sharp. Thus cis- and trans-stilbene adsorbed on Si(100) can be distinguished. The  $\pi^*$ -resonance signal near 285 eV photon energy shows an asymmetric line shape which is different for the two isomers.

The intensities of the  $\pi^*$ -resonances upon changing the incidence angle of the monochromatized synchrotron light has been used to determine the orientation of the molecules with respect to the substrate surface. As shown in Figure 4 the intensity of  $\pi^*$ -resonance of trans-stilbene increases with increasing incidence angle. From this qualitative behavior we can already conclude that this isomer is lying almost flat on the surface. The angular dependence of the other  $\pi^*$ -resonance of cis-stilbene, on the other hand, shows a different behavior. The intensity is high for normal incidence and decreases only slightly with increasing incidence angle. This angular dependence is also obtained in our theoretical studies on the most stable adsorption geometries of the isomers. The two structure models of this detailed analysis are shown in Figure 4, where both isomers are found to bond with the silicon dimer at the substrate surface via their central carbon double bond.



**Fig. 3:** Experimental and theoretical NEXAFS spectra of trans- and cis-stilbene in the gas phase.



**Fig. 4:** Experimental NEXAFS spectra for trans- and cis-stilbene adsorbed on Si(100). The angular dependence of the  $\pi^*$ -resonance is a consequence of the adsorption geometry of the respective isomer.

Our results demonstrate, that clear differences between the  $\pi^*$ -resonance can serve as a fingerprint and permit a clear distinction between the cis- and trans-isomers, i.e. the 'on' or 'off' state of the molecular switch, which is essential for the detection and characterization of the isomerisation at the surface.

**Contact:**

Philipp M. Schmidt  
philipp@fhi-berlin.mpg.de



## Charge transport in plastic electronics

M. Häming<sup>1</sup>, S. Hame<sup>1</sup>, J. Ziroff<sup>1</sup>, T. Boecking<sup>3</sup>, O. Seitz<sup>2</sup>, G. Gavrilla<sup>4</sup>, D. Batchelor<sup>1</sup>, A. Schöll<sup>1</sup>, F. Reinert<sup>1</sup>, E. Umbach<sup>1</sup>

1  
Universität Würzburg

2  
Weizmann Institute of Science,  
Israel

3  
The University of New South  
Wales, Australia

4  
TU Chemnitz

Organic electronic devices found their way into everyday life, as cheap, flexible, and energy saving LEDs and displays in mp3 players or mobile phones. However, for more sophisticated applications of organic semiconductors such as high efficiency plastic solar cells, organic lasers, or in nano-electronics based on single molecules, it is essential to gain a much better understanding of the electronic structure on a molecular level.

Organic semiconductors often exhibit similar conduction mechanisms to inorganic semiconductors (e.g. charge-transfer complexes) including the presence of a hole and electron conduction layer and a band gap. In organic LEDs (OLEDs) both layers need to interact and hence exchange charge efficiently in order to emit light. In solar cells on the other hand photons induce charges in the semiconductor which have to be removed or transported very efficiently in the material to create an electrical current. How does charge occur and how does it move in organic materials?

Common belief is that an electron or hole resides on one molecule ('localized') and hops from there to a neighbouring molecule ('hopping transport'). It carries a polarization cloud and perhaps a molecular distortion ('polaron') with it. The consequences of this picture are low mobility and significant energy differences between charge carriers at a surface as compared to the bulk. Actually, staying in this picture a charge should even avoid a surface for energetic reasons. Also the exciton binding energy ('electron-hole interaction') or the energy required to separate charges in photovoltaics should strongly depend on whether the charges are localized within one or delocalized over several molecules.

To tackle this important issue we create a strongly localized hole in the C 1s core level and measure the ensuing charge redistribution (screening) of the systems valence electrons. However, as the polarization cannot be measured directly, we compare the screening difference between surface and bulk molecules by comparing the binding energies of their photoelectrons. Since surface molecules have fewer neighbours than

bulk molecules the screening by polarization should be lower – and hence the binding energy higher – at the surface than in the bulk. This effect is known to be in the range of 0.3-0.4 eV [1].

As C<sub>60</sub> is a good organic semiconductor, we chose it as one model system [2]. We prepared thin C<sub>60</sub> films in-situ by organic molecular beam deposition in UHV. The probing depth of photoelectron spectroscopy was varied by tuning the electron emission angle and especially the photon energy that the mean free path of the emitted electrons was either minimal or maximal resulting in a surface or bulk sensitive experiment, respectively.

With very high resolution we find for C<sub>60</sub> no difference in the C 1s peak energies between surface and bulk (Fig. 2a).

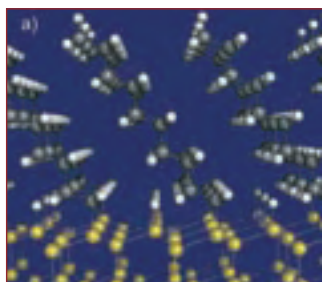


**Fig. 1:**  
Side view at a 'ball and stick' model of alkyl chains adsorbed on a Si(111) surface. [6]

#### References:

- [1] E. V. Tsiper, et al., *Chemical Physics Letters* **360**, 47 (2002).  
 [2] B. Casu et al., *PRL* (in preparation)  
 [3] A. Salomon et al., *Phys. Rev. Lett.* **95**, 266807 (2005).  
 [4] O. Seitz et al., *Langmuir* **22**, 6915 (2006).  
 [5] Ch. Zuberügel et al., *Chem. Phys. Lett.* **238**, 308 (1995).  
 [6] L. Segev et al., *Phys. Rev. B* **74**, 165352 (2006).  
 [7] A. Salomon et al., *Adv. Mater.*, **19**, 445 (2007).

#### Acknowledgements:

Supported by the BMBF. This work is part of a collaboration with the groups of D. Cahen and L. Kronik (Weizmann Inst.) and with T. Boecking (UNSW)

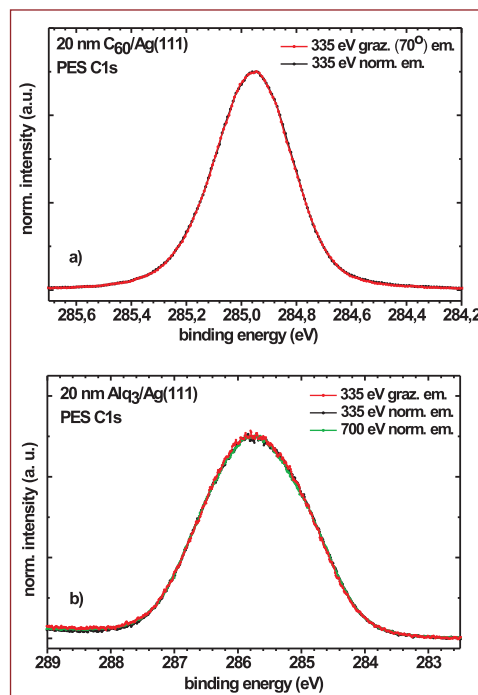


**Fig. 2:**  
A comparison between surface and bulk sensitive signals using C1s peaks of Alq<sub>3</sub> (top) and C<sub>60</sub> (bottom) shows that there is hardly any polarization difference. This leads to the conclusion that the screening charge is delocalized over several molecules.

For the very sharp C 1s signal of  $C_{60}$  the SCLS can be quantified to be lower than about 10 meV. This leads to the conclusion that polarization hardly contributes to screening in contrast to the statements in the literature [1]. Similar results are obtained for  $Alq_3$  (Tris-[8-hydroxyquinoline] Aluminium), a common component in the manufacture of OLEDs, which – unlike  $C_{60}$  – grows in amorphous structures (Fig. 2b). That implies that in contrast to the general picture charge is delocalised due to intermolecular interaction even in amorphous films in a way that the effective charge is spread over several molecules. This challenges the present models for polarization screening, charge transport between molecules (inter-molecular transport), and exciton binding energies in organic materials.

In addition to the understanding of inter-molecular transport, it is also essential to understand the charge transport within a molecule (intra-molecular transport), for the development of plastic electronics. We chose long-chain alkyl molecules which are self-assembled on a silicon surface (Fig. 1) to study such intra-molecular transport. Earlier highly reproducible transport measurements [3, 4] through such monolayers revealed that these materials have quite good transport properties in spite of their large electronic gap [6]. This excited our interest to study their intra-molecular electronic band structure, which is expected to be simply due to a 1D Brillouin zone [5]. DFT calculations also suggested an influence of the interface on the charge transport [6].

We studied samples with various alkyl chain lengths ( $C_{12}$ ,  $C_{14}$ ,  $C_{16}$ ,  $C_{18}$ ) on Si(111) substrates, which have been prepared at the Weizmann Institute (Israel) and at the University of New South Wales (Australia) [3, 4].

First we utilised NEXAFS spectroscopy at the C-K edge with p- or s-polarized light to study the molecular alignment and orientation. The spectra show two resonances which are assigned to  $\sigma^*(C-H)$  and  $\sigma^*(C-C)$  bonds at 287 and 292 eV, respectively (Fig. 3). The evaluation of the polarization dependence revealed a  $40^\circ$  tilt angle of the alkyl chains with respect to the surface normal which is in the range found in the DFT-calculations [6]

Varying the photon energy in the valence photoemission spectra (Fig. 4) leads to a change in momentum  $k$  of the emitted electrons along the surface normal and thus allows the study of dispersion along the alkyl chains. Indeed, we observe significant intra-molecular dispersion, i.e. a 'molecular band structure'. Some of the features between 5 and 10 eV which originate from  $C_{2p}$  orbitals

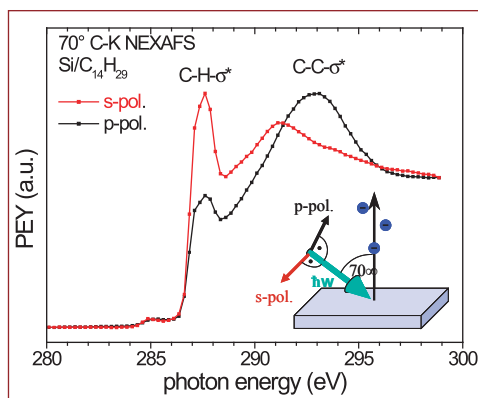


**Fig. 3:** Grazing ( $70^\circ$ ) incidence NEXAFS spectra of a  $Si/C_{14}H_{29}$  sample, recorded in the partial electron yield mode with p- and s-polarization of the incident light. Evaluation of the polarization dependence results in a tilt angle of  $40^\circ$ .

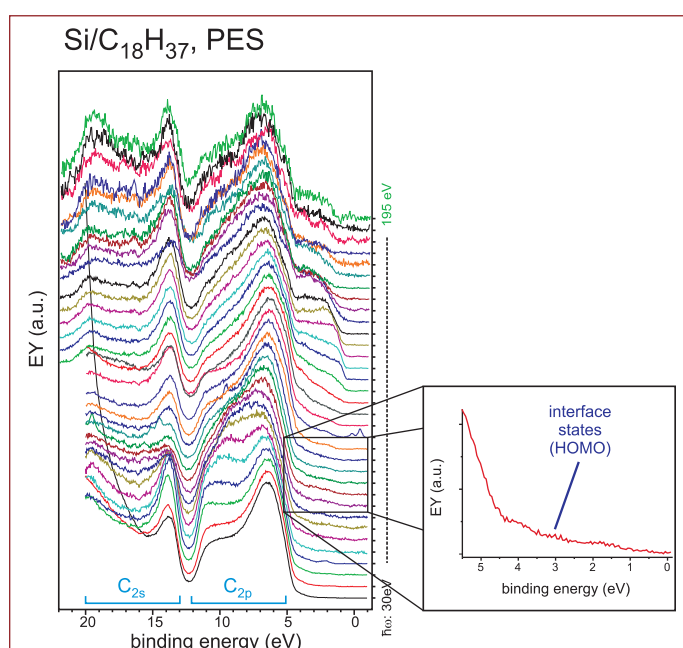


**Fig. 4:** Normal emission PES spectra of a  $Si/C_{18}H_{37}$  sample recorded with p-polarization of the incident light. The photon energy was tuned from 30 to 195 eV in 5 eV steps, and the spectra were normalized to the maximum of the  $C_{2p}$  band. The Si-C interface states between 0 eV and 4.5 eV, play a critical role in charge injection and transport. In the bulk of alkyl crystals where the interface has no influence this regime is part of the electronic gap.

show a rather strong energy dependence on momentum. These electronic bands are more than 2 eV wide, and hence arise from strong intra-molecular interaction. Another interesting feature at 0 - 4.5 eV can be assigned to C-Si interface states by comparison with DFT-calculations [6]; these states may play a critical role in charge injection [7]. In the bulk of alkyl crystals where the interface has no influence this regime is part of the electronic gap.

Taking together the results from earlier transport experiments, DFT calculations, and the present spectroscopic data it can be derived that charge transport along the chain is strongly influenced by molecular states induced by the interface. That means that the properties of the electronic states within the molecule, including band dispersion, depend on both the strength of intra-molecular interaction and on the interface bond. Thus, electronic transport through the molecules can be controlled by chemisorption at the interface.

#### Contact:

Marc Häming  
 Marc.Haeming@  
 physik.uni-wuerzburg.de



Aristotle University of  
Thessaloniki, Greece

## How safe is toxic waste in a glass cage?

F. Pinakidou, M. Katsikini, E.C. Paloura

Glass is very fragile – an annoying experience everyone made who dropped a full bottle. Why would one use glass of all things to store toxic waste? The secret is that the glass is not only the cage, but the waste itself is transformed into glass (Fig. 1). The process is called vitrification. It is an alternative to the common incineration, where the residues of the combustion are stored in tanks or disposed in landfilling areas where they can generate groundwater contamination and weathering problems. Making them

to glass is a rather simple and cost effective method for the management of Fe and Pb containing toxic wastes that originate from petroleum storage tanks. The process produces glass and vitroceramic materials which can homogeneously incorporate into their matrix various toxic elements [1]. The

vitrification process basically consists of mixing and co-melting the toxic waste with silica and soda and quenching of the melt to form solid materials. The final products can be freely disposed, or used for construction and even decorative applications. [2,3]. Nevertheless the question arises: How durable are these glasses?

Here we focus on the determination of the nanostructure and the long term stability of vitrified Fe- and Pb-rich waste-containing stabilized products by means of X-ray absorption fine structure (XAFS) measurements [4]. XAFS is an atom selective, non-destructive characterization technique which provides information on the coordination environment (nearest neighbor distances and coordination numbers) of the absorbing atom. The capabilities of XAFS can be further extended by using capillary optics, which reduce the size of the X-ray beam down to 1-5  $\mu\text{m}$  and thus enhance the spatial resolution of the experiment. The use of the capillary optics also permits the two dimensional mapping of the distribution of various elements in the samples using X-ray fluorescence (XRF) spectroscopy. Thus, by applying the XAFS technique in pre-selected spots of a sample (on the basis of the XRF maps), we can determine the effect of the inhomogeneous distribution of certain elements on their nanostructure.

A very interesting issue that needs to be addressed is the fatigue of waste glasses. Annealing at high temperatures promotes the evolution of fatigue-related effects and thus mimics the effect of long term exposure of the products to the environment. In addition to that, annealing is used for the production of glass-ceramic materials which exhibit exceptional mechanical properties compared to their glassy counterparts. The XRF maps of two solid glasses that contain 60 wt% waste, subjected to annealing at  $T_{\text{ann}} = 600$  and  $800^\circ\text{C}$  are shown in Fig. 2a and b respectively, while that of an as-casted solid product containing 70 wt% waste is shown in Fig. 2c. It is clearly seen that regions with high and low Fe concentration are grown in the bulk of the samples while the distribution of Pb is homogeneous. Therefore, since Pb is depleted from the Fe-rich inclusions it can be proposed that the Fe-rich inclusions are mainly formed by Fe-oxides.

$\mu$ -XAFS spectra were recorded from the regions with high (H-) and low (L-) Fe concentration of the annealed glass to determine whether the inhomogeneous distribution of Fe affects the nanostructure of the Fe atoms. The corresponding Fourier transforms (FT), which have clearly different profiles, are shown in Fig. 3. The only peak that is resolved in the spectra from the L-regions indicates that these regions are glassy [5, 6]. On the contrary, the structure that appears in the distance range 2-4  $\text{\AA}$  in the FT of the spectrum from the H-region is a signature of crystallinity [7, 8]. Indeed, fitting the spectrum from the high-Fe region reveals the presence of magnetoplumbite ( $\text{PbFe}_{12}\text{O}_{19}$ ) microcrystallites embedded into a glassy matrix. Hence, annealing at high  $T_{\text{ann}}$  destroys the homogeneity of the glass: Fe and Pb belong to both the glassy matrix and to crystalline inclusions.

In order to determine the percentage of the Fe atoms that belong to the glassy and crystalline phases we recorded XAFS spectra with the capillary optics removed. In this case the beam size is larger and thus the collected information is averaged over a larger sample volume. The FTs of the Fe-XAFS spectra recorded from the two annealed samples are shown in Fig. 3.



**Fig. 1:**  
Glass (left) and glass-ceramic (right) waste contaminated products. The glasses have a shining, dark color while the vitroceramics have a graded color due to surface crystallization.

### References

- [1] K.E. Haugsten et al., *Waste Manage.*, **20** 167 (2000).
- [2] G. Scarinci et al., *J. Eur. Ceram. Soc.*, **20** 2485 (2000).
- [3] G.H. Zheng et al., *Environmental Progress*, **15** 283 (1996).
- [4] 'EXAFS: Basics, Principles & Data Analysis', B.K. Teo, Springer-Verlag, Berlin (1986).
- [5] F. Pinakidou et al., *J. Non-Cryst. Solids*, **352**, 2933 (2006).
- [6] F. Pinakidou et al., *J. Non-Cryst. Solids*, **351**, 2474 (2006).
- [7] F. Pinakidou et al., *Nucl. Instr. Meth. B*, **246**, 238 (2006).
- [8] F. Pinakidou et al., *Nucl. Instr. Meth. B*, **246**, 170 (2006).
- [9] 'Crystal Structures' vol. 2, R.W.G. Wyckoff, John Wiley & Sons, New York (1964).

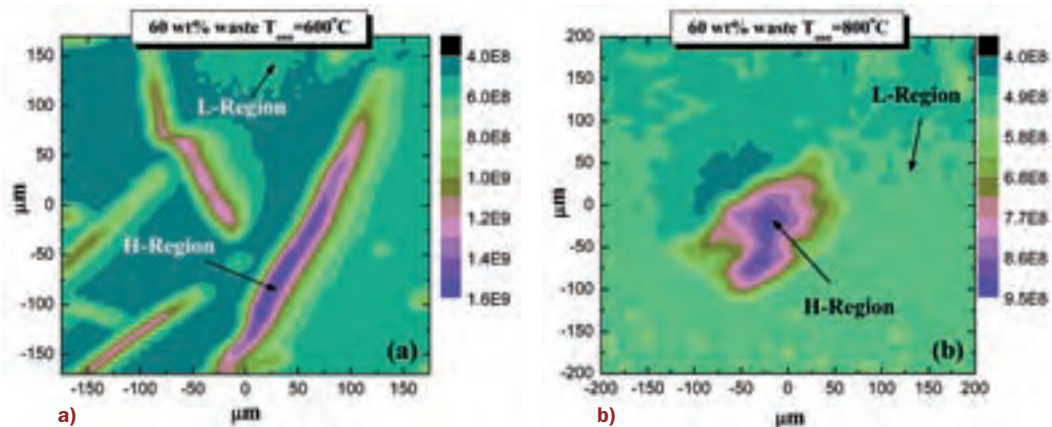


**Fig. 2:**  $\mu$ -XRF maps of two stabilized industrial glasses subjected to thermal treatment at (a) 600 and (b) 800°C, respectively. The maps picture the inhomogeneous distribution of Fe into the waste products. (c)  $\mu$ -XRF maps of a product containing 70wt% waste showing the distribution of both Fe and Pb. Notice the Pb is homogeneously distributed in the same area where Fe forms Fe-rich islands.

The fitting was performed assuming that a fraction of the Fe atoms is bonded in tetrahedra in the glass [6] while the rest occupies octahedral sites in microcrystallites [9]. It is revealed that the increase in the annealing temperature does not affect the extent of crystallinity, i.e. the same percentage of Fe (~80 at%) belongs to the glass. After annealing at  $T_{\text{ann}} = 600^\circ\text{C}$ , only magnetoplumbite crystallites are formed, which render the material safe for the stabilization of Pb. However upon increasing the  $T_{\text{ann}}$  both Fe-rich and mixed Pb and Fe-oxide microcrystallites are formed. This has a detrimental effect on the stability of the product since the former crystalline regions grow with the depletion of Fe from the later, enabling in this way Pb to escape from the material. Thus, the type of microcrystallites grown as a result of thermal treatment affects significantly the stability of the product.

To conclude, the chemical stability of the vitrified solid products is strongly correlated to the structural role of both Pb and Fe. The parameters that need to be monitored during the vitrification process are the concentration of the toxic waste, the processing conditions and the chemical composition of the final products. It is disclosed that the production of vitreous materials is possible when the waste content is less than 65 wt%. Process dependent inhomogeneities in the distribution of the heavy, toxic elements and the type of crystalline phases affect their long term stability. Proper exploitation of our results may lead to safer disposal of Fe- and Pb-rich industrial waste.

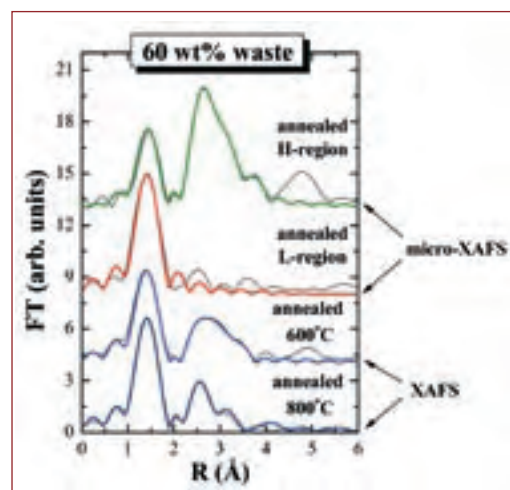
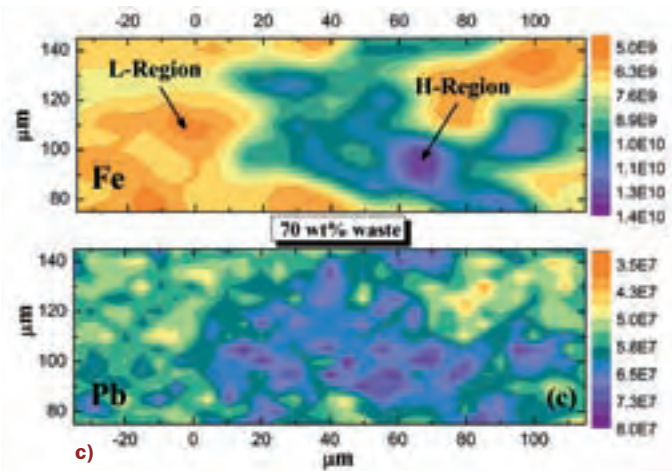


**Fig. 3:** Fourier transforms (FT) of the Fe-K  $\mu$ -XAFS spectra recorded from the H- and L-regions of the glass with 60 wt% waste, annealed at 600°C and of the Fe-K XAFS spectra of the same glass after annealing at the same temperatures. The experimental curve and the fitting are shown in thin and thick solid lines, respectively.

**Contact:**

Eleni Paloura  
paloura@auth.gr

Source: Bill Adler, www.billadler.web



## Package induced deformation of integrated circuits

R. Tilgner<sup>1</sup>, P. Alpern<sup>1</sup>, B.R. Müller<sup>2</sup>, A. Lange<sup>2</sup>, M. Harwardt<sup>2</sup>, M.P. Hentschel<sup>2</sup>

<sup>1</sup> Infineon Technologies, Munich  
<sup>2</sup> Bundesanstalt für Materialforschung und -prüfung (BAM), Berlin

Microelectronics makes live easier and safer. In modern automobiles micro electronic power devices (Fig. 1) are used to control e.g. the window-lift motors, mirror adjustments, automated locking systems, and the footwell lighting. Besides the elevated comfort the safety is also increased, because the driver can concentrate on driving and is not distracted too much by opening or closing the car windows. But the increasing implementation of car electronics makes the vehicle also vulnerable to microelectronics failure. During his "life" a car is usually subjected to all kinds of environmental changes like differences in temperature and humidity or mechanical stress, therefore, electronic components need to have a reasonable robustness in order to match the longevity car.

A major reason for microelectronics failure is due to the way these components are fabricated (Fig. 1): Within a microelectronic component containing an integrated circuit (IC) the interconnect structures establish a link between switching entities of the silicon

chip and the component's outer pins designated to become soldered to a printed circuit board (PCB). The mechanical interaction between package and chip induces deformations which may become starting points of mechanical flaws [1-3], and hence bears the risk of passivation cracking over the metal lines and therefore the failure of the device because of corrosion.

The main reason for deformation of the chip is the layered structure of the overall system chip and package. To spread the heat from the chip switching currents of ~1A the silicon is soldered at 328°C by lead on a copper heat slug (the use of lead is regulated by ROHS [4]). Cooling down to room temperature the shrinking copper will distort the thermally more inert silicon chip. In a similar way a mold compound is used to fix and to cover the construction. It is processed at 175°C as a liquid which shrinks and hardens after cooling down. As these interactions of different materials and temperatures influence the stability of the device, modern quality and reliability development ask for the degree of these interactions. The knowledge of the real deformation of the crystal is essential for calculations and predictions concerning nanofracture mechanics and hence to develop a device package with minimized IC deformation.

**Fig. 1:** Micro electronic power device for switching currents of up to 1 A.

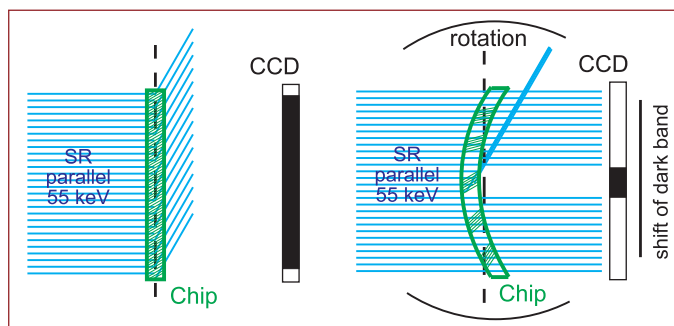


**Fig. 2:** Illustration of the pseudo absorption of single crystals. Left: X-rays are deflected across the whole flat single crystal due to diffraction. No X-rays arrive at the detector (the radiograph would be dark). Right: for curved crystals the Bragg condition is only fulfilled in local parts. This leads to dark bands in the radiograph (local pseudo absorption, see Fig. 2, right). The position of the dark band can be moved by rotating the crystal.

To visualize the real deformation of the crystal we developed a new inspection method at the materials research beamline (BAMline) [5]. The method – Synchrotron Laue Contrast Radiography (SLCR) – is based on the coherent scattering of monochromatic synchrotron radiation by the net planes of the silicon single crystal of the electronic device (Fig. 2).

X-rays will be deflected by a single crystal if  $d$  (the spacing between the planes in the atomic lattice of the single crystal),  $\lambda$  (the wavelength of the synchrotron beam) and  $\Theta$  (the angle between the incident beam and the scattering planes) fulfil the Bragg condition  $n\lambda = 2d \cdot \sin\Theta$ . For a perfectly flat single

### References:

- [1] P. Alpern et al., *IEEE Trans. CPMT* **A17**(3), 583 (1994); Erratum in **18**, 862 (1995).  
 [2] P. Alpern et al., *VTE* **10**(1), 10 (1998).  
 [3] Z. Suo, *Comprehensive Structural Integrity* (I. Milne, R.O. Ritchie, B. Karihaloo, Editors-in-Chief), Elsevier 2003  
 [4] *Official Journal of the European Union*, L37/19-23, Annex, point 7, 2003  
 [5] Müller, B.R. et al., *Nucl. Inst. and Meth. in Phys. Res. A*, **467/468**, 703 (2001).

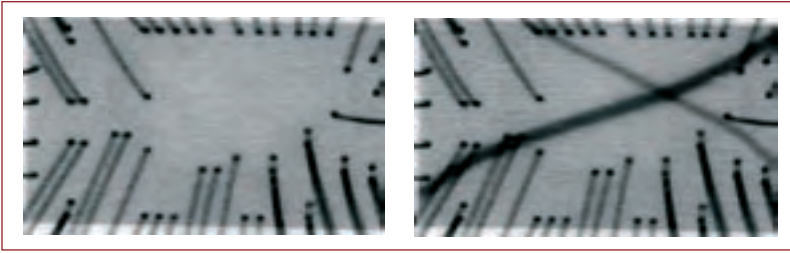


**Fig. 3:**  
Radiograph of the bonding wires,  
(left) without and (right) with  
dark bands, respectively

crystal the condition is fulfilled across the entire crystal simultaneously (Fig. 2, left). Thus the whole radiograph becomes dark, but not because of absorption (pseudo-absorption).

In flexural loaded single crystals the scattering planes are distorted. Thus the Bragg condition is only fulfilled in some local areas of the crystal (Fig. 2, right). This leads to more or less small dark bands in the radiograph. The shape and the width of the local pseudo-absorption bands depend on the shape and the radius of curvature of the flexural loaded crystal, respectively.

To explore the final shape of the whole chip the microelectronic device is placed in front of a CCD camera system (pixel size  $14.4 \mu\text{m} \times 14.4 \mu\text{m}$ ) and irradiated by a parallel and monochromatic beam (55 keV). The surface normal of the chip is parallel to the beam axis and the beam cross-section covers the entire chip. The measurement is performed by rotating the device around an axis perpendicular to the beam while recording in parallel the radiographs of the device. In most cases the CCD camera displays the radiograph of the absorbing gold bonding wires (Fig. 3, left). But for specific orientations of the device dark bands across the silicon crystal become visible (Fig. 3, right). By rotating the curved crystal (angle scan range  $0.11^\circ$ , step width  $0.001^\circ$ ) the dark bands are moving across the radiograph and assemble a series of dark band positions (isoclines) across the whole crystal (aggregated in a 2D plot in Fig. 4). The isoclines density represents the local radius of curvature of the crystal, typically, ranging between 5 m and 50 m (the higher the density the smaller the radius of curvature).

From the 2D isoclines plot we derived a 3D surface profile of the flexural loaded Silicon crystal with a very high resolution of about  $\pm 1 \text{ nm}$  in height (Fig. 5). A 3D surface profile of a chip just after packaging is shown in Fig. 5, left. As mentioned, the temperature dependent shrinkage of the heat slug which is situated beneath the profile exceeds that of the chip, and the mold compound leading to a smooth convex shape of the chip. The amplitude between the minimal and maximal height is about 1,500 nm, which may

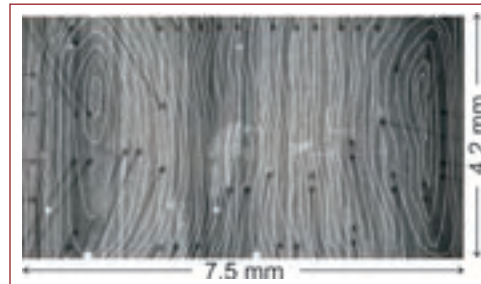
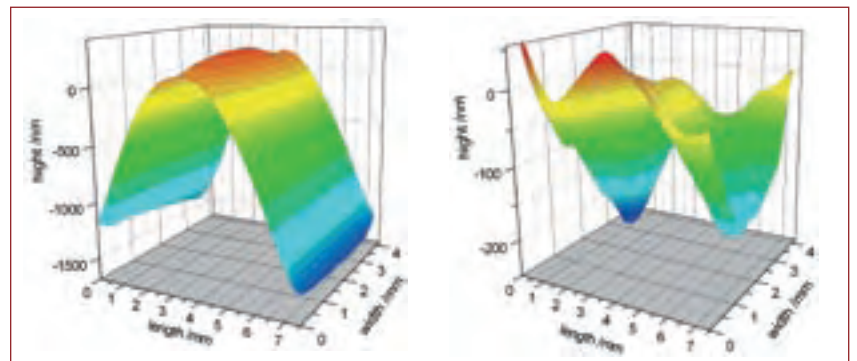


**Fig. 4:**  
Aggregation of all dark band positions (isoclines) during rotation (angle range  $0.11^\circ$ , step width  $0.001^\circ$ ). In the background the radiograph of the chip is shown. In the centre part of the radiograph a lead void is visible by the brighter grey coloured area.



not harm the functionality of the electronic device.

A second device was measured after a stress treatment of 1,000 temperature cycles from  $-55^\circ\text{C}$  to  $+150^\circ\text{C}$ . The shape has changed to a more irregular, 'magic-carpet-like' profile with a reduced height amplitude of about 300 nm (Fig. 5, right), which is possibly due to a partial loss of the adhesive strength between the package and the chip caused by degradation e.g. of the solder during stress treatment.

But what are the detection limits for more minute mechanical influences of the package. We found a void within the lead solder from X-ray absorption radiography. The SLCR measurement also discovered the mechanical effect of the gold wire bonds and the lead solder void on the surface of the silicon crystal. Finally, even higher order effects such as interaction between void and bonding wires have been detected. From these results SLCR can be considered as a new powerful inspection method to evaluate even minute degradation processes in electronic devices. This is an essential for any prognostic reliability work in the future.

**Fig. 5:**  
3D surface profiles (lateral resolution:  $14.4 \mu\text{m} \times 14.4 \mu\text{m}$ , height resolution:  $\pm 1 \text{ nm}$ ) deduced from the isoclines plots (Fig. 4). The Cu heat slug is situated beneath the profile. Left; chip just after packaging, right; chip after a stress treatment of 1,000 temperature cycles from  $-55^\circ\text{C}$  to  $+150^\circ\text{C}$ .

**Contact:**

Bernd R. Müller  
bernd.mueller@bam.de



## Soon to become physicists' best friend?

### Blue diamond superconductivity in the light of terahertz spectroscopy

M. Ortolani<sup>1</sup>, U. Schade<sup>1</sup>, L. Baldassarre<sup>2</sup>, S. Lupi<sup>2</sup>, P. Calvani<sup>2</sup>, Y. Takano<sup>3</sup>, M. Nagao<sup>3</sup>, T. Takenouchi<sup>4</sup>, H. Kawarada<sup>4</sup>

1  
BESSY

2  
Università di Roma  
'La Sapienza', Italy

3  
National Institute for Materials  
Science, Tsukuba, Japan

4  
Waseda University, Tokyo, Japan

Diamonds are transparent, lustrous, sparkling, and as we all know 'the girls best friends'. Even more attractive and expensive are the very rare natural 'blue diamonds'. For a scientist diamond is carbon, where each atom is covalently bonded to four other carbon atoms in a compact crystal structure to generate the largest insulating gap. This means that diamond is transparent to infrared, visible and ultraviolet light up to 5.5 eV and that diamond does not conduct electricity. Blue diamonds contain a small amounts of boron impurities. Being a p-type semiconductor blue diamonds can weakly conduct an electrical current if the boron concentration reaches 0.5% (Fig. 1) [1]. At higher boron contents it held a surprise in hand, which might make blue diamonds soon to be also 'physicists' best friend'!

Nowadays, diamond crystals and films can be produced in a laboratory (even if the beauty and the size of natural gems cannot be equalled) with a technique called microwave-assisted chemical vapour deposition (MW-CVD). Blue diamond has also been produced in several labs. Due to its properties boron-doped diamond is a possible candidate for substituting silicon in the future generation computer chips. However, the way to the 'diamond computer' is still long: n-type diamond is not easily available yet and the behaviour of charge carriers travelling in a diamond crystal still needs to be understood.

In 2004, it came as a surprise for the scientific community that weakly conducting boron-doped diamond is even a *superconductor* at liquid-helium temperature (4.2 K) for boron-concentrations above 3%. Diamond films grown at the NIMS in Tsukuba showed a  $T_c$  as high as 11 K.

Superconductivity is a quantum state of matter where electrical currents are free to run without friction (zero electrical resistance), found in some metals such as tin, aluminium, lead, and niob, below a critical temperature  $T_c$  of few K. The Bardeen, Cooper and Schrieffer (BCS) theory explains superconductivity in metals with the pairing of electrons via the electron-phonon interaction. The ground state below  $T_c$  is a 'Cooper

pair' condensate, and the first excited state is the breaking of a Cooper pair, requiring an energy  $2\Delta$ . In the case of weak BCS interaction, all the above described quantities are related to each other by:

$$2\Delta = 3.53 k_B T_c \approx \hbar\omega_0 \exp(-1/\lambda) \quad (1)$$

where  $\omega_0$  is an Einstein phonon frequency, and  $\lambda \ll 1$  is a coefficient describing the strength of the electron-phonon interaction. Not all superconductors are well described by the BCS theory, which holds for metals. Highly-doped semiconductors like the high- $T_c$  copper oxides also have a superconductivity state, where  $2\Delta$  seems uncorrelated with a  $T_c$  ranging up to 160 K. The mechanism for superconductivity in the high- $T_c$  copper oxides is still unknown; it is then legitimate to ask ourselves if we can describe boron-doped diamond within the BCS theory, or not.

At University of Rome we measured by Fourier-transform infrared spectroscopy (FT-IR) the reflectivity  $R$  (Fig. 2a) of a MW-CVD-grown boron-doped diamond film, produced at NIMS with a  $T_c$  of 6 K. The sample surface had a size of 2.5 x 2.5 mm, one of the largest to be produced with the necessary homogeneity in the boron-content. Through Kramers-Kronig analysis, the presence of electron-phonon interaction is demonstrated by the abrupt increase for  $E = \hbar\omega > 130$  meV of the scat-

#### References:

- [1] Y. Takano et al., *Appl. Phys. Lett.* **85**, 2851-2853 (2004).  
 [2] L.Boeri et al., *Phys. Rev. Lett.* **93**, 237002 (2004).  
 [2] M. Abo-Bakr et al., *Phys. Rev. Lett.* **90**, 094801 (2003).  
 [4] M. Ortolani et al., *Phys. Rev. Lett.* **97**, 097002 (2006).  
 [5] T. Yokoya et al., *Nature* **438**, 647-650 (2005).

#### Acknowledgements:

Supported by the EU via the IASFS funds.

We thank J.S. Lee for valuable help and P. Kuske, G. Wustefeld and J. Feikes for tuning the storage ring during the "low-alpha" shifts.

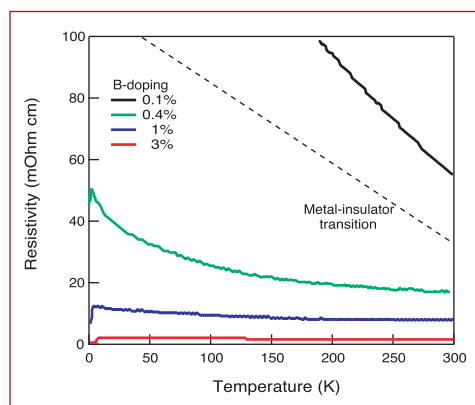


**Fig. 1:** Resistivity curves show that B-doped diamond is a hole-doped semiconductor. For high enough B concentration, it also becomes a superconductor below 4 - 8 K.

tering rate  $\Gamma(\omega)$  (Fig. 2b) and a peak at  $\hbar\omega = 130$  meV in the electron-phonon interaction spectrum  $\alpha^2F(\omega)$ , indeed corresponding to a Raman-active phonon of diamond [2]. However, to check Eq. 1 we still needed to determine the optical gap  $2\Delta$ . In principle, this can also be done with the FT-IR technique, since  $R(T < T_c)$  is predicted to be 100% for photon energies below  $2\Delta$ , and to decrease rapidly above that energy. In practice,  $2\Delta$  falls in the 0.1-1.0 THz range for most superconductors, where blackbody and even normal synchrotron sources provide a photon flux which is largely insufficient to probe small samples like ours.

BESSY provides a unique tool which could solve the problem. When the storage ring is set in the 'low- $\alpha$ ' mode, a stable state with short bunches (bunch length below 1 mm) is obtained. All electrons in a short bunch emit synchrotron radiation at millimetre-wavelengths in phase, leading to a power  $N$  times larger than normal radiation, where  $N \sim 10^8$  is the number of electrons in one bunch [3]. This kind of radiation is called Coherent Synchrotron Radiation (CSR) and up to now has been obtained in a stable state useful for spectroscopy only at BESSY. At the IRIS beamline, CSR is used as a high-brilliance broadband source for FT-IR which allows one to measure the absolute reflectivity of mm-sized samples in the 0.1-1.0 THz range.

The reflectivity change below  $T_c$ ,  $R(T < T_c)/R(T = 10 \text{ K})$ , measured with a liquid-helium cryostat shows a peak at 1.4 meV (0.3 THz), whose intensity increases when lowering the temperature (Fig. 3). This behaviour is predicted by the BCS theory (black lines in Fig. 4) and corresponds to the increase of the superconducting condensate density and to a dc-field penetration depth of 1 micron at 2.6 K [4]. If we input in Eq. 1  $\hbar\omega_0 = 130$  meV from the data in Fig. 2 and  $2\Delta = 1.4$  meV from the CSR data in Fig. 4, we obtain  $\lambda = 0.12$ , a moderate electron-phonon coupling, perfectly in the range of the BCS theory. However, the measurements at BESSY also showed an unpredicted effect in superconducting diamond: we obtain  $2\Delta/k_B T_c \sim 3.0$ , a value slightly lower than 3.53 in

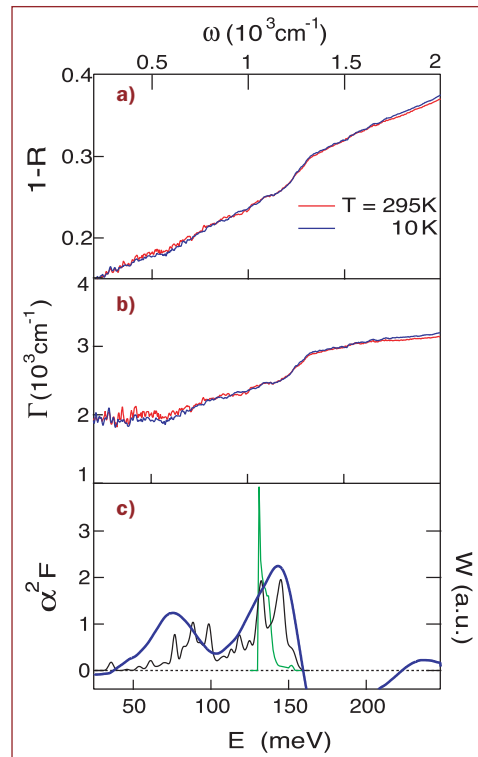


**Fig. 2:**  
**a)** The raw absorbance  $1-R(\omega)$  at two temperatures.  
**b)** The frequency-dependent relaxation rate of the free carriers  
**c)** Electron-phonon spectral function  $\alpha^2F(\omega)$ : from experiment (blue line), from two different calculations (green and the black lines).

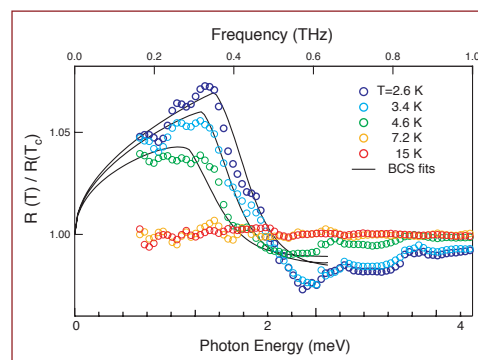


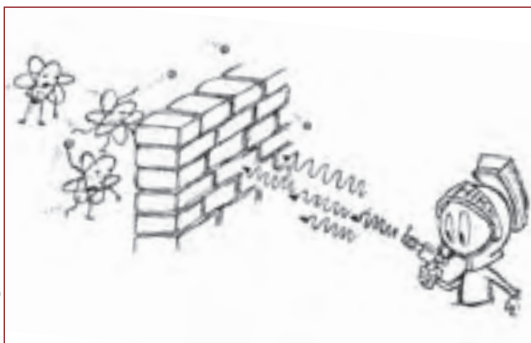
**Fig. 3:** Reflectivity of heavily boron-doped diamond between 2.6 and 10 K in the sub-THz region, normalized to its values at 10 K. Data taken with the unique Coherent Synchrotron Radiation source at BESSY (circles) show the enhancement in  $R(T < T_c)$  at  $2\Delta$ , which is the minimum energy needed to break a Cooper pair. The lines are fits based on the BCS theory.

Eq.1. This result can be understood in terms of the anisotropic band structure of diamond [5], which produces  $k$ -space anisotropy of  $\Delta$ .

In conclusion, Terahertz spectroscopy with the unique CSR source at BESSY played a key role in describing the superconducting mechanism in blue diamond, also contributing to the understanding of electronic interactions in doped semiconductors.

**Contact:**

Michele Ortolani  
 ortolani@bessy.de



M. Gorgoi

## Breaking through!

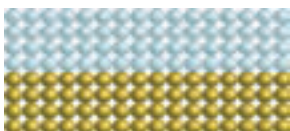
### High energy photoelectrons give insight into deeply buried interfaces

M. Gorgoi<sup>1</sup>, O. Karis<sup>2</sup>, S. Svensson<sup>2</sup>, F. Schäfers<sup>1</sup>, W. Braun<sup>1</sup>, G. Öhrwall<sup>2</sup>, G. Andersson<sup>2</sup>, M. Marcellini<sup>2</sup>, W. Eberhardt<sup>1</sup>

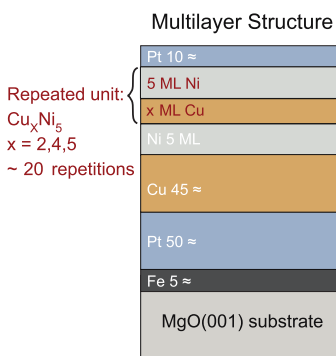
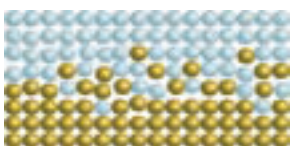
<sup>1</sup> BESSY  
<sup>2</sup> Uppsala University, Sweden

**Fig. 1:** (Left) Schematic illustrations of a perfect, idealized interface and a 'real' interface with disorder. (Right) The investigations were performed on  $\text{Cu}_x\text{Ni}_5$  multilayers, where the notation refers to the basic unit repeated in the multilayer.

A perfect interface



A real interface is never perfect



In almost any scientific discipline we find processes and phenomena that are dictated by the detailed properties of what we can refer to as functional interfaces. In medicine, such an interface could be the contact of an implant with tissue of the human body and in physics researchers are interested in the insulator-ferromagnet interfaces, which are the central structure in a tunnel-magneto-resistance (TMR) device used for read-heads in the next generation hard drives.

Interface composition and geometry alter chemical, electric, magnetic, optical and mechanical properties of the entire system. Even in simple assemblies made of two sorts of metal atoms, an interface is never perfect. There is always some degree of disorder (Fig. 1). The characterization and control of those properties is of particular interest to refine and optimize interface function.

X-rays to overcome these limitations by exciting photoelectrons in the depth of 20 or more atoms. Such photoelectrons bear a much higher kinetic energy and eventually escape to the surface to convey information of the electronic structure inside. However, the cross-section is very low and hence the number of detectable photoelectrons. Therefore we needed a high flux beamline with an outstanding energy resolution to be able to fully exploit this new technique.

Using the high-kinetic-energy photoelectron spectroscopy station (HIKE) at the KMC 1 (bending magnet) beamline we studied the interfaces of Cu/Ni multilayers sandwiched between two platinum layers. Those materials can be regarded as models of TMR devices. In order to control interfacial quality of the multilayers, the samples were heated to a preset temperature and subsequently cooled to room temperature (annealing). We recorded Cu 2p photoelectron spectra for several annealing temperatures in the range of 20 - 300°C. Figure 2 shows the results obtained for the  $\text{Ni}_5\text{Cu}_5$  system as one example of our investigated samples.

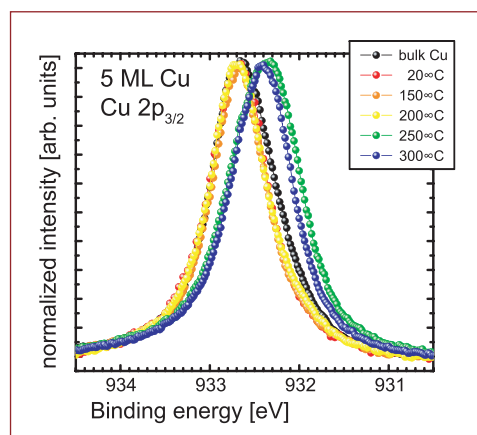


**Fig. 2:** Cu 2p photoelectron spectra for several annealing temperatures, using high excitation energies which give the emitted photoelectron sufficient energy to escape also from deeply buried interfaces.

#### References

[1] E. Holmström, et al., *Phys. Rev. Lett.* **97**, 266106 (2006).

#### Acknowledgements

Supported by Swedish Research Council (VR), Göran Gustafsson Foundation, EU IA-SFS - I3 program, and Swedish Foundation for Strategic Research (SSF).

The theoretical work presented here was performed by E. Holmström, W. Olovsson, I. A. Abrikosov and B. Johansson.

If researchers study interfaces using photoelectron spectroscopy they are usually looking at the characteristics of electrons in the valence orbitals using VUV or soft X-rays. However, with this approach the obtained information is restricted to the surface (up to several atoms depth) mainly owing to the limited escape depth of low energy photoelectrons.

With the availability of photoelectron analyzers combining highly stabilized power supplies with excellent sensitivity and energy resolution, researchers started to use hard

We find that the measured Cu 2p lines are quite similar for annealing temperatures up to 150°C. The red and orange curves both exhibit a small shift to higher binding energy relative to the Cu 2p line for bulk Cu. Also the line profile reveals a narrowing for the orange curve (150°C) compared to the un-annealed sample. The yellow curve (200°C), exhibits a small additional shift to higher binding energy. At 250°C the Cu 2p spectrum shifts about 200 meV to lower binding energy, and annealing at 300°C results in a small shift back and a change in the width of measured line. The data suggest a dramatic change of the interface quality and we are now able to directly observe the evolution of interface roughening in the multilayer.

To further quantify our results we need to model our measured core level spectra and relate them to interface order parameters. Looking at the cartoon in Fig. 1, illustrating the less idealized interface, we note that most of the atoms within some proximity of the interface are chemically different. The shape of a photoelectron line from a particular core level will reflect the distribution of core-level binding energies of all grey or yellow atoms. The peak position of this photoelectron line is thus a measure of a characteristic core-level binding energy. The difference between the peak position from a bulk sample and the peak position from a multilayer sample may then be seen as the average core-level shift (CLS) of all yellow (or grey) atoms in the multilayer.

Attempting to directly calculate a core level shift for each chemically unique atom for any given configuration at an interface is not a viable route. Based on our previous experience with calculations of magnetic properties in nanolayered systems we have reduced the complexity of the problem into a single characterization parameter which determines the main contribution to the core-level shift average. The quality parameter  $\Gamma$  describes the spatial extent of the diffusion at an interface by a Gaussian distribution function with standard deviation. Thus as illustrated in Figure 3 for  $\Gamma = 0$  the interface is abrupt and no diffusion takes place. Once the interface parameter  $\Gamma$  is defined it is straightforward to calculate core level shifts within our model.

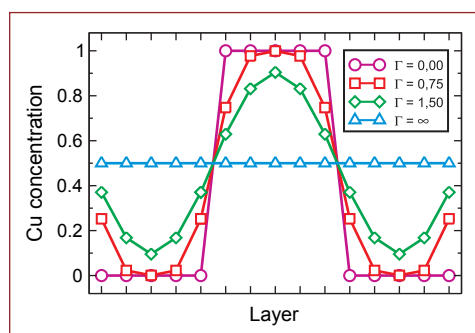


**Fig. 3:** Concentration of the Cu atoms as a function of the layer number within the multilayers and as a function of the  $\Gamma$  parameter. As shown, when  $\Gamma$  reaches infinity there is a complete intermixing of the Cu/Ni layers, the concentration of Cu atoms is 50% from each layer.

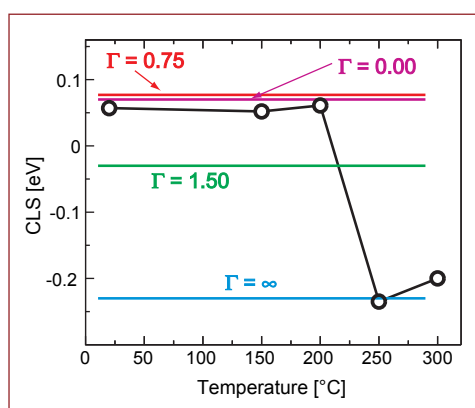


**Fig. 4:** This figure summarizes our theoretical and experimental results for the  $\text{Cu}_5\text{Ni}_5$  sample. On the left axis we plot the measured core-level shift relative to binding energy of bulk Cu. The full horizontal lines give the results of the theoretical calculations. By comparing the measured peak positions with the calculated core-level shifts we find that it is easy to identify different levels of interface intermixing in the multilayered materials. The agreement is remarkable.

In Figure 4 we show the energies of the peak positions from Fig. 2, together with the calculated core-level shifts for different interface diffusions. By comparing the measured core level shifts with the calculated results for different  $\Gamma$  values we easily identify different levels of interface intermixing in the multilayered materials. The agreement between the experimental data and the calculation is remarkable.

In summary, we have shown that a bending magnet beamline at a medium energy storage ring provides good conditions for HIKE spectroscopy. It is possible to perform non-destructive studies of the quality of multilayer structures by using HIKE photoelectron spectroscopy with state-of-the-art electron analysers. A modern beamline features sufficient precision to follow the alloying of nanolayered devices upon interface alteration.

**Contact:**

Olof Karis  
Olof.Karis@fysik.uu.se



## The multiple touch: How the $\omega$ repressor controls plasmid maintenance

W. A. Weihofen<sup>1,3</sup>, A. Cicek<sup>1</sup>, F. Pratto<sup>2</sup>, J. C. Alonso<sup>2</sup>, W. Saenger<sup>1</sup>

1 Freie Universität Berlin

2 Centro Nacional de Biotecnología, Madrid, Spain

3 Department for Molecular and Cellular Biology, Harvard University, USA

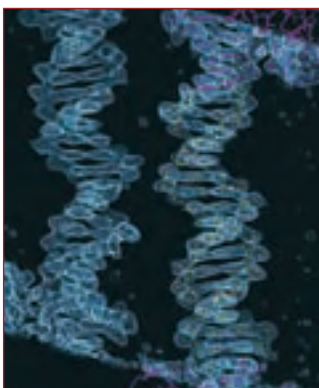


**Fig. 1:** Section of the electron density map showing two parallel free DNA double helices. On the right a yellow stick model for free DNA was placed into the density, and part of the model of the  $\omega_2$ -repressor/DNA complex is shown at the top in magenta.

During hospitalization the chances of acquiring a secondary infection can be as high as one in ten. These are often caused by 'superbugs', like the Methicillin-resistant *Staphylococcus aureus* strain that has developed resistance to all penicillin class antibiotics. The reason for the rapid spreading of antibiotic resistance among bacteria is that different strains can exchange genes conferring antibiotic resistance through horizontal transfer of mobile genetic elements, such as short and self-replicating DNA molecules known as plasmids. However, depending on the environmental conditions the bacterium does not always benefit from the genes carried on a plasmid and often is better off without them, since plasmid replication consumes energy. To prevent their loss, plasmids such as pSM19035, which was isolated from the human pathogen *Streptococcus pyogenes* [1,2], have evolved some cunning mechanisms that secure their stable maintenance in bacterial hosts even when there is no selective pressure. What are these mechanisms to sustain stable plasmid maintenance? First, pSM19035 can replicate in a broad range of Gram-positive bacteria, thereby gaining access to a variety of species (i.e. Streptococci, Staphylococci, Enterococci) living in different environments. Second, the plasmid exists in only 1 to 3 copies per cell to avoid an energy penalty for its host in producing plasmid DNA. Third, during cell division pSM19035-encoded proteins actively distribute the plasmid to the daughter cells. Fourth, if this fails, the plasmid encodes two proteins which act as a toxin-antitoxin system tasked to kill all plasmid-free progeny of the host [3].

All these functions are mediated by a collection of proteins, whose expression is under the control of a single protein called  **$\omega$  repressor**. We determined the 3-dimensional structure of the  $\omega$  repressor and showed that  $\omega$  repressor forms a dimer ( $\omega_2$ ) and is a member of the family of Ribbon-Helix-Helix repressors [4]. In general, two Ribbon-Helix-Helix dimers recognize symmetric DNA sequences called palindromes, with each repressor dimer inserting a two-stranded  $\beta$ -sheet (Ribbon) into the DNA major groove where direct and specific contacts to DNA bases are formed.

Since it controls the expression levels of a variety of genes,  $\omega_2$  binds to unique recognition sequences in promoter regions that precede a gene and control its expression. These promoter regions comprise arrays of ten, nine or seven consecutive and non-palindromic seven base-pair repeats (with the sequence AATACA called heptad, symbolized by  $\rightarrow$ ) that are organized as ( $\rightarrow\rightarrow\leftarrow\leftarrow\rightarrow\rightarrow\leftarrow\leftarrow$ ); ( $\rightarrow\rightarrow\rightarrow\rightarrow\rightarrow\rightarrow$   $\leftarrow\leftarrow$ ) or ( $\rightarrow\rightarrow\leftarrow\leftarrow\rightarrow\rightarrow\leftarrow\leftarrow$ ) [1]. We found that one  $\omega_2$  binds weakly to a single heptad, but binding is tight to at least two consecutive heptads and tightens further with increasing number of heptads. In addition, the DNA affinity depends on heptad arrangement, since binding affinity for heptads in diverging ( $\leftarrow\rightarrow$ ) orientation is 6-fold lower compared to repeats with direct ( $\rightarrow\rightarrow$ ) or converging ( $\rightarrow\leftarrow$ ) orientations [2]. This means that altering numbers and arrangements of heptad repeats modulates the DNA affinity for  $\omega_2$ , which is in turn used to tune gene expression levels. But how does  $\omega_2$  recognize different orientations of heptad repeats and how does this result in altered binding cooperativity and affinity?

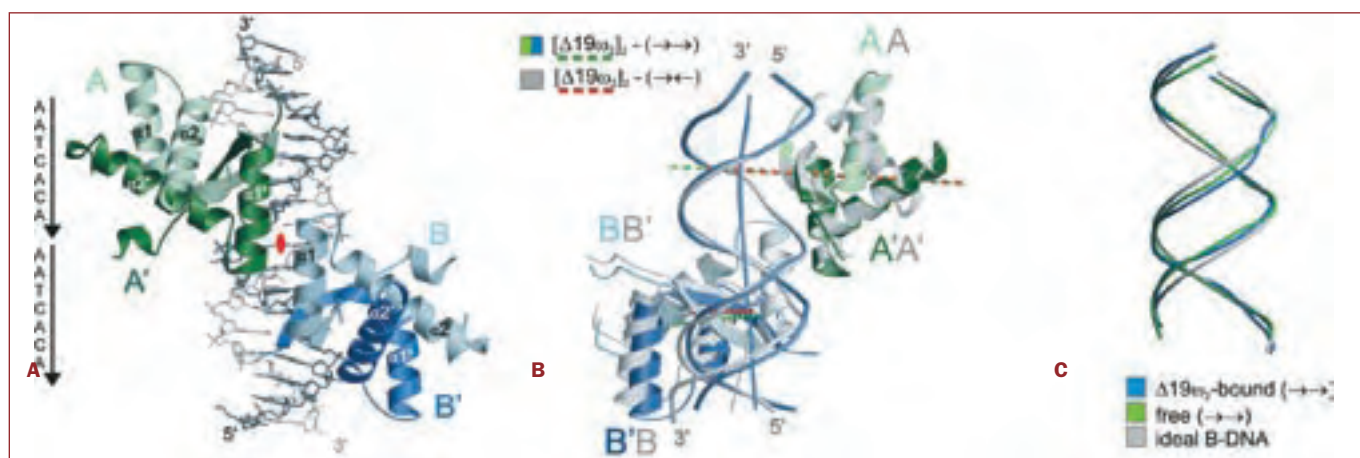
To address this question, we crystallized  $\omega_2$  in complex with DNA comprising two heptads in the ( $\rightarrow\rightarrow$ ) or ( $\rightarrow\leftarrow$ ) arrangement [5]. X-ray diffraction data from crystals were collected at beamlines 14.1 and 14.2 of Freie Universität Berlin and BESSY. After data processing we were able to calculate electron density maps which were interpreted with  $\omega_2$ /DNA models. A section of an electron density map with and without a placed model is shown in Fig. 1. To our surprise, this section revealed only electron density for free DNA without any bound  $\omega_2$ , whereas another section showed electron density for a complete  $\omega_2$ /DNA complex. Fig. 2A shows a model of this complex with two  $\omega_2$ -repressors ( $\omega_2$ s) bound to DNA comprising two heptads. **That free DNA was found with repressor-bound DNA in the same crystal was unprecedented.** Since it is very common that DNA-binding proteins cause conformational changes in their recognition sequences upon binding, we compared both, free DNA and  $\omega_2$ /DNA conformations (Fig. 1C), and found that the intrinsic conformation of the free DNA resembles the  $\omega_2$ -bound DNA better than ideal B-form DNA.

#### References:

- [1] A. B. de la Hoz et al., *Proc. Natl. Acad. Sci. U S A*, **97**, 728 (2000).  
 [2] A. B. de la Hoz et al., *Nucleic Acids Res.*, **32**, 3136 (2004).  
 [3] A. Meinhart et al., *Proc. Natl. Acad. Sci. U S A*, **100**, 1661 (2003).  
 [4] K. Murayama et al., *J. Mol. Biol.* **314**, 789 (2001).  
 [5] W. A. Weihofen et al., *Nucleic Acids Res.*, **34**, 1450 (2006).

#### Acknowledgements:

Supported by DGCICT, EU FP5 and Fonds der Chemischen Industrie.



This observation provides a nice example for the bipartite recognition mechanism of many DNA-binding proteins which can read out and form direct contacts to individual bases and at the same time can contact/distort and read out DNA conformations. To address the question of how  $\omega_2$  binds to and distinguishes between different heptad orientations, we superimposed complexes of  $\omega_2$ s bound to DNA with direct ( $\rightarrow\rightarrow$ ) or inverted ( $\rightarrow\leftarrow$ ) repeats in Fig. 2B. The figure reveals that the  $\omega_2$ s are 0.6 Å closer when bound to the convergent ( $\rightarrow\leftarrow$ ) repeats compared to  $\omega_2$ s bound to direct ( $\rightarrow\rightarrow$ ) repeats. In both cases the cooperative interactions between neighboring  $\omega_2$ s mediated by helices  $\alpha 1$  are similar (Fig. 1A, B). However, when  $\omega_2$ s bind to heptad repeats in diverging ( $\leftarrow\rightarrow$ ) orientation (not shown), it is predicted that the two  $\omega_2$ s will be 0.6 Å more distant rendering cooperative interactions less favorable, and this explains the lower affinity of  $\omega_2$  for heptads in this orientation.

The structures represent only a small part of a natural complex of  $\omega_2$ s bound to a natural promoter, which can feature 7 to 10 consecutive heptads. However, we extended our structures and modeled one of the  $\omega_2$ /promoter complexes. Fig. 3A shows  $\omega_2$ s bound to seven heptads in the promoter with arrangement ( $\rightarrow\rightarrow\rightarrow\rightarrow\leftarrow\leftarrow$ ) [1]. The model implies that the seven  $\omega_2$ s form a left-handed spiral around the right-handed and straight DNA. Fig. 3B shows that the negatively charged sugar-phosphate backbone of DNA faces the positively charged surface of the  $\omega_2$ s, giving rise to electrostatic interactions.

Our results explain how the  $\omega$  repressor recognizes and binds to DNA heptad repeats arranged in different orientations and how this leads to the modulation of transcription of several genes.

**Fig. 2:**

(A) Structure of two  $\omega_2$ -repressors bound to DNA comprising two direct heptad repeats ( $\rightarrow\rightarrow$ ). DNA strands are shown in grey stick mode. Cartoons of  $\omega_2$ s (A/A' and B/B') are shown in light and dark green and blue, respectively. Helices  $\alpha 1$ ' of A' and  $\alpha 1$  of B are related by a pseudo-twofold axis perpendicular to the paper plane (red ellipse) and form cooperative interactions between  $\omega_2$ s. (B) Superimposition of  $\omega_2$ s bound to DNA comprising direct ( $\rightarrow\rightarrow$ ) and convergent ( $\rightarrow\leftarrow$ ) heptad repeats (grey). DNAs are represented by lines drawn along the sugar-phosphate backbone. The axes of  $\omega_2$ s are indicated by dashed lines coloured green for  $\omega_2$ s bound to direct repeats ( $\rightarrow\rightarrow$ ) and red for grey  $\omega_2$  bound to convergent repeats ( $\rightarrow\leftarrow$ ). Note that the red  $\omega_2$  axes are closer for  $\omega_2$ s bound to the convergent repeats ( $\rightarrow\leftarrow$ ) (C) Phosphate backbone of the 14 bp promoter regions of free operator-DNA ( $\rightarrow\rightarrow$ ) in green and  $\omega_2$ -bound DNA ( $\rightarrow\rightarrow$ ) in blue superimposed on ideal B-DNA (grey). Note that the free ( $\rightarrow\rightarrow$ ) DNA resembles the  $\omega_2$ -bound ( $\rightarrow\rightarrow$ ) better than the ideal B-Form DNA.

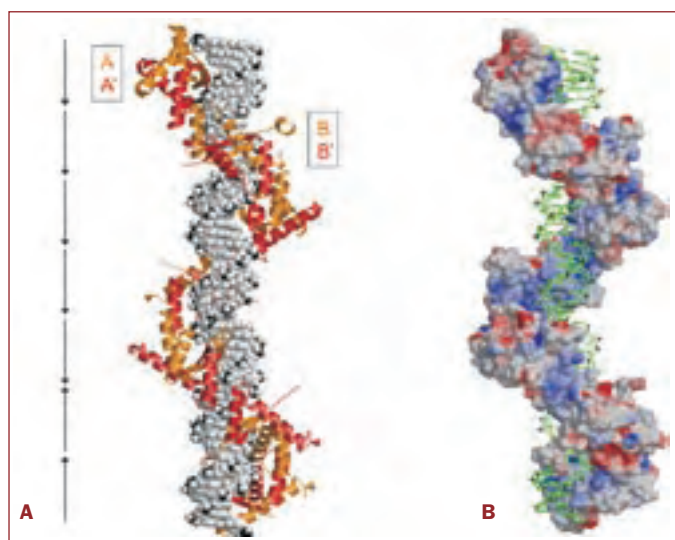


**Fig. 3:**

**Model of  $\omega_2$ s bound to a natural promoter comprising seven heptads. (A) DNA represented by a space filling model and  $\omega_2$ s as orange/red ribbons, (B) DNA in stick presentation (green) and  $\omega_2$ s in surface presentation coloured according to the electrostatic potential (negative and positive charges red and blue, respectively). The model is based on the structures shown in Fig. 2. Repressors  $\omega_2$  form a left-handed protein-matrix winding around the nearly straight operator.**

**Contact:**

Wilhelm A. Weihofen  
weihofen@mcb.harvard.edu  
Wolfram Saenger  
saenger@chemie.fu-berlin.de



## Collapsing in style: How a protein finds its fold

A. Hoffmann<sup>1</sup>, A. Kane<sup>2</sup>, D. Nettels<sup>1</sup>, D. Hertzog<sup>2</sup>, P. Baumgärtel<sup>3</sup>, J. Lengefeld<sup>3</sup>, G. Reichardt<sup>4</sup>, R. Seckler<sup>3</sup>, O. Bakajin<sup>2</sup>, B. Schuler<sup>1</sup>

<sup>1</sup> Universität Zürich, Switzerland

<sup>2</sup> Lawrence Livermore National Laboratory, Livermore, USA

<sup>3</sup> Universität Potsdam

<sup>4</sup> BESSY

Proteins are the most versatile biomolecules, performing a vast number of functions in living organisms. They act as chemical factories in the form of enzymes accelerating chemical reactions; as regulators, signal transducers, channels or transporters; as grids and beams for cellular structure; or as defence elements to fight infections from bacteria or viruses. To perform these functions, proteins have to assume a well-defined three-dimensional structure to specifically interact with each other or other target molecules. Remarkably, their structural arrangement is entirely and uniquely encoded in the sequence of building blocks they are made from. In a cell, proteins are produced as linear chains of amino acids, according to a blue print stored on DNA, the molecular library of any cell. After synthesis, this polypeptide chain spontaneously folds into the three-dimensional structure required for its function, making protein folding one of the most important and universal self-organization processes in nature. If this process fails, misfolded, non-functional protein molecules accumulate in or between cells giving rise to degenerative diseases such as Alzheimer's or Creutzfeldt-Jakob Disease.

The detailed mechanism on how folding proceeds has been a topic of research for about a century. There are several models of how the early stages of protein folding proceed,

especially for large proteins. In one type of model, the polypeptide first collapses to minimize unfavourable interactions of hydrophobic side chains with water (hydrophobic collapse) and then finds its final fold from the collapsed state. In other models, the formation of secondary structure precedes collapse to the native fold. But due to the complexity of the process, involving thousands of atoms within a protein molecule, and a range of weak interactions whose balance is difficult to quantify, many questions remain. In contrast to the described two-step models, folding of simple small proteins was regarded to be a single step process (Fig. 1).

A powerful method to study the kinetics of structure formation in proteins is circular dichroism spectroscopy in the UV wavelength range, where the relative absorbance of left- and right-circularly polarized light depends on the three-dimensional arrangement of the polypeptide chain (Fig. 2). Unfortunately, the wavelength range available in commercial instrumentation equipped with Xenon lamps does not allow the kinetic investigation of structure formation in many proteins consisting of  $\beta$ -pleated sheets, which is one of the main structural motifs in proteins. We have now started to solve this problem by combining synchrotron radiation with microfluidics. Synchrotron radiation allows us to access wavelength ranges where the formation of  $\beta$ -structure can be followed easily; the use of microfluidic mixing devices allows us to mix solutions in milliseconds or even faster [1]. We can thus trigger folding reactions, e.g. by rapid dilution of chemicals that destabilize protein structure, and then use synchrotron radiation in the UV to follow the rapid processes of protein folding. Another crucial virtue of synchrotron radiation is its brilliance, which enables us to focus a small beam into the microfabricated devices, where the protein molecules fold into their final native structure while they flow down the tiny channel of the mixer (Fig. 3).

### References:

- [1] D. E. Hertzog et al., *Analytical Chemistry* **76**, 7169 (2004).  
 [2] B. Schuler et al., *Nature* **419**, 743 (2002).  
 [3] E. A. Lipman et al., *Science* **301**, 1233 (2003).  
 [4] A. Hoffmann et al., *Proc. Natl. Acad. Sci USA* **104**, 105 (2007).  
 [5] W. Kremer et al., *Eur. J. Biochem* **268**, 2527 (2001).

### Acknowledgements:

Supported by the Human Frontier Science Program, the Schweizerische Nationalfonds (B.S.), DFG and BMBF.

The work of O.B., A.K. and D.H. was performed under the auspices of the U.S. DoE Lawrence Livermore National Laboratory supported by the Center for Biophotonics and the SEGRF Program at LLNL.

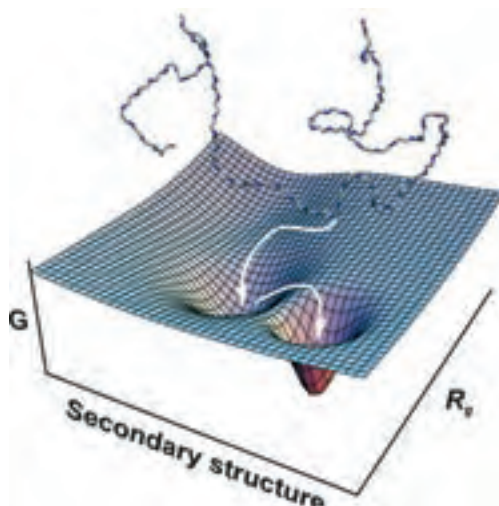


**Fig. 1:** Sketch of the free energy surface governing protein folding with a representation of an unfolded protein chain illustrating the difficulty of finding the energy minimum, i.e. the correct fold.



Using this approach, we have recently investigated the collapse of a small beta-protein, the cold shock protein (CspTm) from the hyperthermophilic bacterium *Thermotoga maritima* (Fig. 2). This protein has become an important model system to investigate elementary processes in protein folding due to the simplicity of its folding mechanism. Rather unexpectedly, this protein has recently been found to collapse prior to the actual folding process [2, 3], but it was unknown whether collapse is accompanied by the formation of specific structure. Our experiments revealed that already during collapse, about 20% of the  $\beta$ -structure content of the folded protein is present in the collapsed, yet unfolded protein chain [4]. Independent spectroscopic methods using single molecule fluorescence showed that in spite of the presence of  $\beta$ -structure, the polypeptide chain can still be well described as a random coil in terms of polymer physics [4], indicating that the structure formed is highly dynamic and covers only short segments of the molecule. This work is an important step towards understanding the interplay between the generic heteropolymer properties of proteins and the specific intramolecular interactions that drive the folding process. The next steps will be to further clarify the detailed influence of preformed structure on protein folding.

The combination of microfluidic mixing and synchrotron radiation circular dichroism spectroscopy (SRCD) is expected to be of great value for a wide range of questions regarding the structure, dynamics and function of biomolecules. Potential applications include not only protein folding, but also the interaction of proteins with ligands, such as drugs, and many of the conformational changes that proteins undergo while they do their duty as key players in all organisms.

**Fig 2:**

**Cartoon representation of the three-dimensional structure of the cold shock protein used in this work [5]. The blue ribbons represent  $\beta$ -structure, whose formation is difficult to detect with conventional methods, but can be observed using kinetic SRCD.**

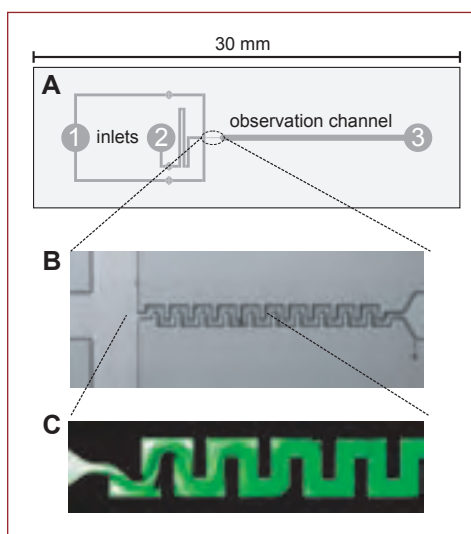
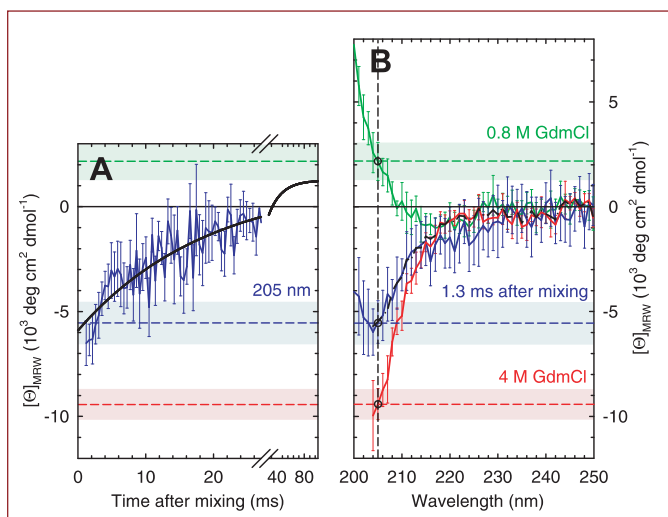


**Fig. 3:**

**The microfluidic mixing device. (A) Channel pattern of the microfluidic mixing device. To initiate refolding, unfolded protein injected into inlet 2 is diluted with buffer injected into inlet 1. Rapid mixing occurs in the serpentine-shaped channel shown as a scanning electron micrograph (B). The synchrotron radiation beam is positioned in the observation channel, such that a position in the channel can be related to a given time after mixing, i.e. after the start of the folding reaction. (C) Mixing process in the serpentine channel visualized with fluorescein in a fluorescence microscope.**



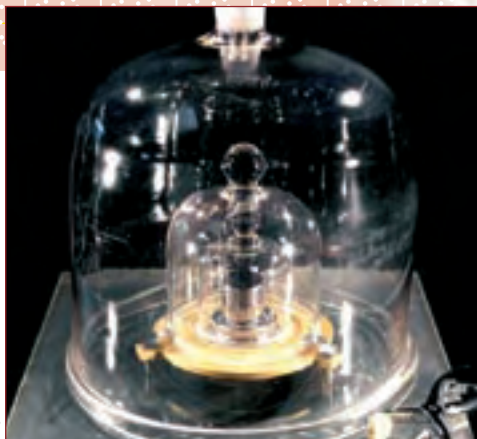
© 2007, National Academy of Sciences, U.S.A.

**Fig. 4:**

**(A) Collapse and refolding kinetics of CspTm at 0.8 M GdmCl measured at 205 nm (blue line), and a single-exponential fit to the data (black line). (B) CD spectrum taken 1.3 ms after mixing (blue line), compared to equilibrium spectra under native (green line; 0.8 M GdmCl) and unfolding conditions (red line; 4 M GdmCl). The corresponding ellipticities at 205 nm are indicated in the spectra as blue, green, and red dashed lines, respectively. The shaded light blue, green, and red bands indicate one standard deviation from the equilibrium ellipticities of folded and unfolded CspTm, respectively, at 205 nm.**

**Contact:**

Benjamin Schuler  
schuler@bioc.unizh.ch



## How much is a kilogram? Every atom counts

M. Krumrey, L. Cibik

Physikalisch-Technische  
Bundesanstalt, Berlin

It is kept under three 'cheese covers' in a safe at the Bureau International des Poids et Mesures (BIPM) at Sèvres near Paris. There it is since it was manufactured of an alloy of 90% platinum and 10% iridium in 1889: the kilogram. This makes the base unit for mass a very special unit in many senses. Most base units, like meter, ampere and second, have been redefined during the last decades in relation to atomic or fundamental constants. But up to now, the kilogram cannot be traced back to fundamental constants with sufficient accuracy. It is the last base unit of the international unit system that is realized by a comparing object, the prototype.

Every country that joined the metric system has its own national prototype that is regularly compared with the one at BIPM and it turned out that the 40 copies seemed to be heavier by about 50 micrograms than the original, creating an urgent need for a new definition of the kilogram.

Currently, two international projects are pursued to redefine the kilogram by fundamental constants: the watt balance to trace it back to the Planck constant and almost perfect silicon spheres to trace it back to the Avogadro constant [1]. The Avogadro constant defines the number of particles in a mole. If one could count this number very precisely (there are about  $6.022 \times 10^{23}$ ), one would have precise measure for the mass at hand. For the Avogadro project, spheres of high-purity silicon have been made. 'To count' the number of atoms in these spheres, not only the lattice parameter and the molar mass of silicon have to be determined, but also the density of silicon by measuring the mass and the volume of the silicon sphere. This seems to be an easy task, but the required uncertainties are extremely low. For the sphere radius of about 5 cm, the required uncertainty is about 0.1 nm! This is the thickness of a single atomic layer, i.e. every atom counts. To make it even more complicated, all silicon

surfaces are covered by a native silicon oxide layer. By cleaning and subsequent thermal oxidation, this layer can be replaced by a  $\text{SiO}_2$  layer with known stoichiometry and a thickness of a few nm. The traceable determination of this layer thickness is an important contribution to the project.

An absolute and highly accurate method for layer thickness determination is X-ray reflectometry (XRR). With this technique, the reflectance of the sample is measured as a function of the grazing incidence angle of X-rays. Due to interference effects of radiation reflected on the layer surface and radiation reflected on the

layer/substrate interface (Fig. 1), oscillations occur in the reflectance curve which can be fitted according to the Fresnel equations. In commercial instruments, Cu  $K\alpha$  radiation with an energy of 8,048 eV is used. This radiation is not well suited for  $\text{SiO}_2$  on Si because the optical constants are very similar at

this energy so that the reflection at the layer/substrate interface, and therefore also the oscillations, are very weak. In addition, the very small grazing angles (only a few degrees) prevent the application on the surface of the sphere.

With synchrotron radiation, any photon energy can be selected. It has been shown that pronounced oscillations occur at 1,841 eV, just above the Si K absorption edge in pure Si, because the chemical bonding in the oxide causes a shift of the edge towards higher energies [2]. Pronounced oscillations also occur at the oxygen K edge around 540 eV. Here, steep incidence angles up to  $50^\circ$  can be used, enabling the application on strongly curved surfaces. The required intense radiation is available at the undulator beamline in the PTB laboratory at BESSY [3].

However, a slight increase of the layer thickness had been observed in first measurements using the UHV X-ray reflectometer at this beamline [4]. Therefore, an energy-dis-

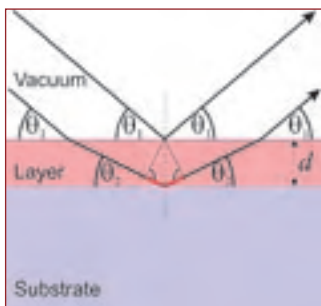
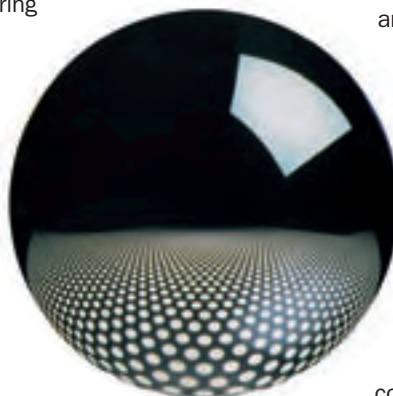


**Fig. 1:**  
Principle of layer thickness  
determination by X-ray  
reflectometry (XRR)



#### References:

- [1] P. Becker et al., *Metrologia* **40**, 271 (2003).
- [2] M. Krumrey et al., *Thin Solid Films* **459**, 241 (2004).
- [3] F. Scholze et al., *Proc. SPIE* **4344**, 402 (2001).
- [4] D. Fuchs et al., *Rev. Sci. Instr.* **66**, 2248 (1995).

#### Acknowledgements:

We thank Peter Becker, the leader of the Avogadro project, and Ingo Busch who coordinates the surface investigations on the spheres.

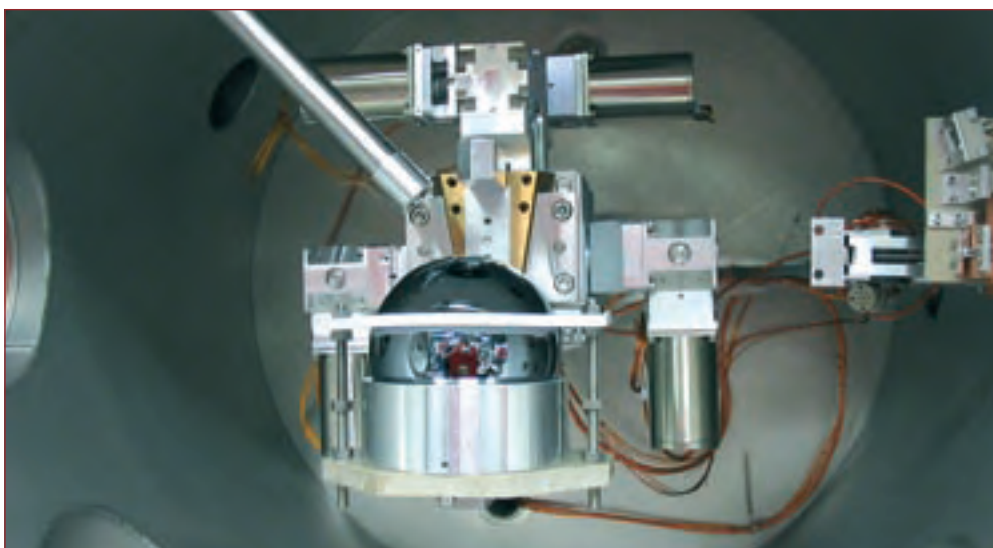


**Fig. 2:** Silicon sphere in the UHV-reflectometer with XRR and XRF detectors.

persive silicon drift detector (SDD) has been added to the reflectometer for simultaneous X-ray fluorescence analysis (XRF) measurements on the same position of the surface to distinguish between the growing of a carbonaceous contamination layer and a further oxidation of the surface (Fig. 2). By taking spectra before and after each XRR measurement, the change in the fluorescence intensities can be observed. It turned out that the oxide layer is stable while the thickness increase is due to the carbon-containing contamination layer (Fig. 3). This growth of the contamination layer only occurs at the position where the XRR measurements have been performed.

By reducing the radiant power, almost stable conditions have been achieved. By performing the measurements at different positions on the sphere the dependence of the oxide thickness on the crystal orientation has been studied. A minimum occurs in the (100) direction. A typical example of the measured and fitted reflectance is shown in Fig. 4. Here the total layer thickness was 6.7 nm, including about 0.5 nm of contamination. Additional measurements at different energies around the O K edge will allow the separate determination of the individual oxide thickness and the contamination layer and to further reduce the uncertainty from currently about 0.2 nm to the required 0.1 nm.

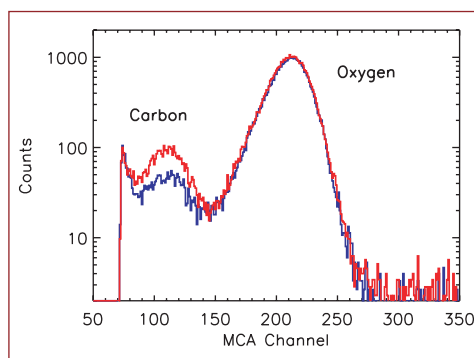


**Fig. 3:** XRF spectra at an excitation energy of 550 eV before (blue) and after (red) XRR measurements in intense radiation.

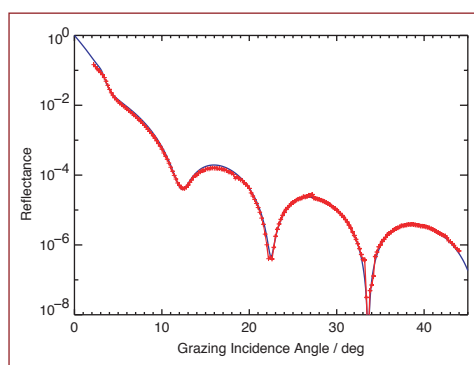
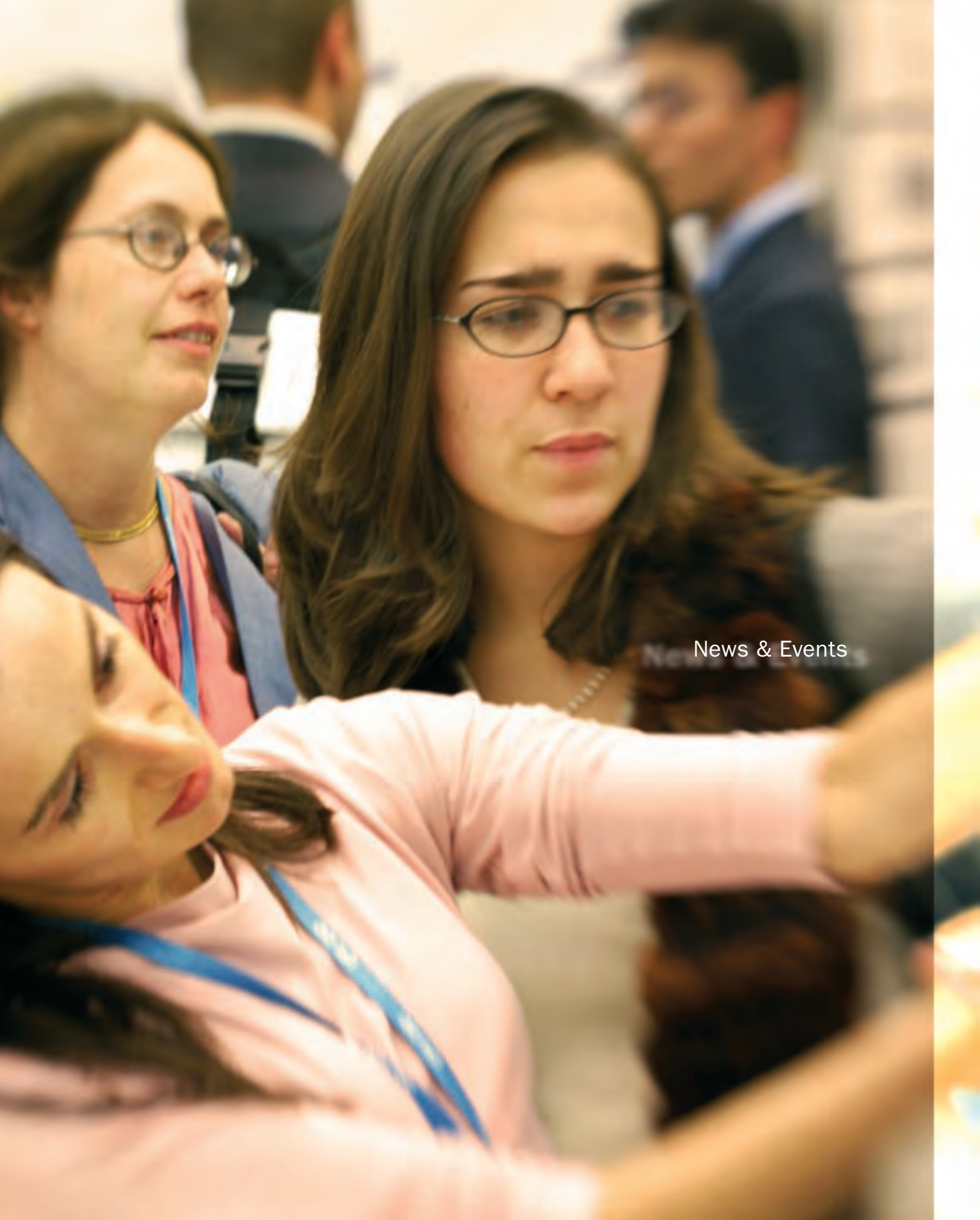
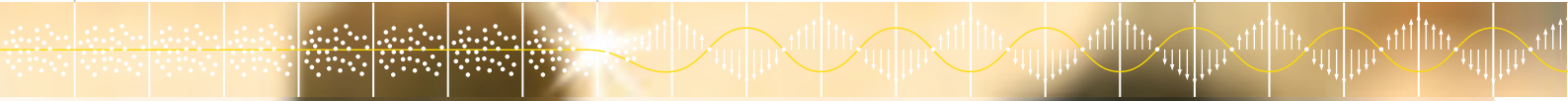


**Fig. 4:** Measured and fitted reflectance of a silicon sphere at 536 eV. The resulting total layer thickness is 6.7 nm.

**Contact:**

Michael Krumrey  
Michael.Krumrey@ptb.de



News & Events

## News

The German Science Minister Dr. Annette Schavan visited the science campus in Adlershof in January 2006. After a tour through BESSY, she had a discussion with the directors of several research institutes. The main problems addressed were the low incomes especially for young scientists and engineers and the twelve year limit for short-term contracts. The minister assured her support in solving these pressing questions.

Her Brandenburg colleague Prof. Dr. Johanna Wanka came by in October on a tour focussing on co-operations between Brandenburg and Berlin in science and technology. Vice-Minister Shang of China as well as members of the 'Ordre pour le merit' also honoured BESSY with their visit. BESSY is proud of the ongoing interests of high-ranking as well as general visitors which added up to about 3,000 individuals last year, among them one third from schools. We are working continuously to improve our tours, informational material and guides to make the stay at BESSY as pleasant and as informative as possible for our guests. We are obliged to an open-house policy trying to satisfy most if not all visit requests.

In the summer the FEL06 conference took place at the head quarter of the Deutsche Telekom right in the centre of Berlin. This very successful meeting in a stimulating ambience attracted some 300 participants from all over the world, a sign of the growing FEL community.

The upcoming FEL06 conference was an omen of success for BESSY as the technical design report was evaluated very positive in May by the Wissenschaftsrat (German Science Council). 'There is no other European initiative as technically advanced and as scientifically competent as the BESSY team,' stated the international board of referees.



The FEL06 conference took place at the Deutsche Telekom headquarter right in the heart of Berlin.



German Science Minister Annette Schavan (above), her Brandenburg colleague Johanna Wanka (right) and Vice-Minister Shang (below) visit BESSY.



Their recommendation led to the decision of building a two step, cascaded FEL to proof the principle of the high gain harmonics generation (HGHG) scheme including the seeding by an external laser – major characteristics of the BESSY second generation FEL. The proposal for the construction of cascaded FEL – named STARS – was published in October. The evaluation board also recommended that BESSY should in future be funded within the Helmholtz Association of German Research Centres. First considerations for creating a new institute together with the Hahn-Meitner-Institute have already started.

The PTB celebrated the opening a new Synchrotron radiation source in Berlin-Adlershof, the Willi-Wien-Laboratory, which will be operated by the BESSY crew. On the reception with several local and national guests, Prof Göbel, president of the PTB, gave an opening speech with an historic review on the importance of radiometry.





**Little ones and grown-ups explore the fun of sciences.**

Under the motto 'Electrons, Light and Computer sciences' the 'Lange Nacht der Wissenschaften' took place already in May 2006 due to a slightly more important event - the soccer World Championship later in the summer. The motto took over the title of the whole year declared by the German Ministry of Research and Education as 'Year of Computer Sciences'. The Physikanten – already well-known not only by the Lange Nacht audience played again in sold-out halls – being certainly one highlight of this night. We are very proud on an already long-term collaboration with schools in Berlin. The pupils themselves asked to take part at the event, explaining some of the experiments together with a BESSY staff member. Especially, their help in the kid's lab is greatly acknowledged.



**BESSY is an open house not only for the 'Lange Nacht der Wissenschaften'.**



## Events

More than 3,600 visitors enjoyed again, or for the first time the fun of science during this night.

Also in May the Leibniz Association invited politicians to an evening, where member institutes presented their results on 'water'. A quite general exhibition on various aspects of the subject opened the ground also discussions with the present politicians. Together with the Max-Born-Institute we presented novel studies on the structure and the memory of water.

During the summer the 'Physik zum Frühstück' interactive breakfast lecture was one event selected for the campaign 'Germany - Land of Ideas'. A certificate was handed over by a representative of the Deutsche Bank, sponsor of the campaign. The success of this campaign was celebrated with an ice cream party the way molecular chefs and physicists do it by using liquid nitrogen.



**Scientists of Max-Born-Institute and BESSY presenting 'water'.**

**'Imaging' was the subject of the Industrieforum, jointly organized by ANKA, BESSY, and Hasylab.**



**'Physik zum Frühstück' ice cream party celebrating the honour of being selected for the 'Land of Ideas' initiative.**



In autumn BESSY participated at the exhibition 'Highlights der Physik' in Bremen. Under the theme WellenWelten (WaveWorlds) we presented two hands-on experiments on Terahertz-radiation and the Free Electron Laser. This annual event by the Deutsche Physikalische Gesellschaft attracts regularly big crowds to science show, humoresque talks and pupils contest – making this exhibition really a magnet in the hosting city.

The Industrieforum – a workshop addressing users from industry and those who think of becoming one - was organized by ANKA in collaboration with Hasylab and BESSY. The subject 'Imaging' was highlighted in talks on chip technology, material sciences and fuel cells, leading to fruitful discussions with potential users afterwards.

BESSY hosted this years Business talks – a talk round initiated by the Adlershof campus management (WISTA). On this occasion representatives of local business, politics and science discussed under the headline 'Media meets Technology'.



**Adlershofer Business Talks bringing together local business and sciences.**



At the end of the year users, visitors and staff were 'surprised' by a performance taking place in and around a plexiglass cube (an art object by Sonja Hartmann) right in front of the main entrance. The artist Petra Lang tried to 'wallpaper memories' ('Erinnerungen tapezieren') - the subject of her performance. We believe it was an interesting, yet sometimes odd, experience for all who had encountered the project.



Jürgen Kirschner as 'Mr. Kulicke'.

## Users' Meeting 2006

This year already the 25<sup>th</sup> BESSY Users' Meeting took place. Looking back a quarter of a century ago, experimenting at BESSY was quite adventurous: The new scientific results were exciting, as was the everyday life of a user. A pioneer of the first hour – Jürgen Kirschner (MPI Halle) - reminisced about teething problems, Einstein proving machines, exciting experiments, and 'Mr. Kulicke' and the crane in his key note lecture.

With now some 1,300 international users, the research areas worked at BESSY have grown tremendously. The meeting had seen a record number of poster contributions, displayed and lively discussed in the experimental hall. Some recent highlights were presented in the talks covering such diverse topics as Laser-excited atoms, protein folding and industrial waste management.

The second day started with a report of BESSY management on the development and the status of accelerator and instrumentation, in particular, the status of the FEL project - which is in the STARting blocks - was highlighted. Christian Jung summarized

the new beamlines and experimental stations, which are reaching for better spatial, time or spectral resolution. Among other things, Peter Kuske reported on the preparations to increase the total flux. To serve that introducing a top-up injection mode is currently evaluated, also an increase of the ring energy might be a future option. Ralf Püttner, on behalf of the User Committee, encouraged users to comment whether their group anticipates benefiting from any of these changes, or is worried by adverse effects like non-exponential characteristic of the ring current due to topping-up, and change of the undulator spectrum due to a change in ring.

Ralf Püttner and Wolfgang Braun did not candidate again for the User Committee. We would like to thank them for their work in the committee and congratulate Thomas Schmidt, (Universität Würzburg) and Tobias Lau (TU Berlin) to their election along with hope for an ongoing good cooperation on improving the life and work for users at BESSY.

The Users Meeting was accompanied by several satellite workshops. The topics ranged from 'Ultrafast X-ray science', 'From diffraction to imaging' to 'High resolution Photoemission' focusing on new developments at BESSY. The industrial exhibition featured some 50 exhibiting companies which were also gratefully sponsoring the traditional 'Berliner Buffet'.



Poster session at the 25<sup>th</sup> Users' Meeting.

### Workshops

28 <sup>th</sup> International Free Electron Laser Conference (FEL06)	August 27- September 01
Workshop on Nanoscale Spectroscopy and Nanotechnology	Rathen, September 17-21
Synchrotron Radiation in Arts and Archeology (SR2A)	September 27-29
Industrieforum	Karlsruhe, November, 17
Workshop on Ultrafast X-Ray Sciences	December, 5-6
From Diffraction to Imaging	December 6
BESSY Users' Meeting	December, 7-8
Workshop on High resolution Photoemission	December, 8-9



Participants of the SR2A workshops.

## Ernst-Eckhard-Koch Prize

The vitrification of toxic, heavy metal containing sludges, that pile-up in storage tanks of oil industry, is a relatively new method to safely dispose the waste. Glasses show a high chemical resistance and stability against corrosion. In her PhD thesis the physicist Fani Pinakidou of Aristotle University Thessaloniki investigated such glasses with synchrotron radiation. One of her results is that the chemical resistance is depending on the presence of heavy metals, their local surrounding in the matrix and their valence. She received the Ernst-Eckhard-Koch-Prize for her thesis. For further details read her article in this issue.

The bestowal of the Ernst-Eckhard-Koch-Prize is a link between BESSY's tradition and the scientific future, remembering the work of Ernst-Eckhard Koch and shining a light onto an extraordinary Ph.D. thesis and a young scientist, who will surely play an important role in future science projects.



**Ernst-Eckhard-Koch Prize laureate Fani Pinakidou (Aristotle University Thessaloniki).**

## Innovation Award on Synchrotron Radiation

Spectro-electron microscopes are devices that combine spectroscopy and microscopy. Therefore, it is possible to gain not only structural, but also chemical, electronic and magnetic information of a sample with the high spatial resolution. For the development of a device named SMART with much higher transmission and resolution at BESSY, the innovation award was granted to Wilfried Engel (Fritz-Haber-Institut) (departed in the meantime), Dirk Preikszas (Carl Zeiss AG) and Thomas Schmidt (Universität Würzburg).

In electron microscopy the resolution was limited by uncorrected aberrations. As a workaround, apertures were used in photo electron emission microscopy (PEEM), leading to the best possible resolution of about 10 nm, ten times worse than the theoretical limit. This method also has the drawback that parts of the electron beam are lost due to the aperture, so that there is not enough intensity for time-resolved studies.

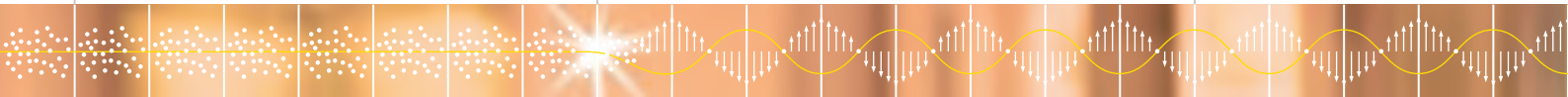
With SMART, the physicists corrected the aberrations with an electron mirror. This allowed to improve the resolution to better



than 3 nm. Since this mirror made the apertures nearly obsolete, the electron image is about 100 times brighter as in conventional electron microscopes.

The Innovation Award on Synchrotron Radiation is awarded for an outstanding technical achievement or experimental method that promises to extend the frontiers of research with synchrotron radiation. The prize is awarded annually by the Society of BESSY Friends and Sponsors.

**The laureates: Dirk Preikszas (left) and Thomas Schmidt (right). For the deceased Wilfried Engel his wife received the prize.**

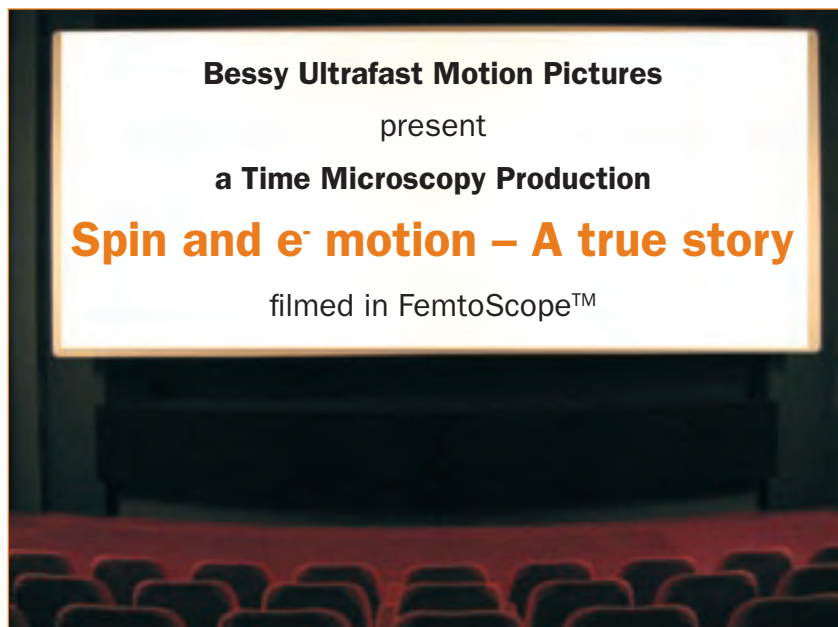


## Femtoslicing Special

Chirping violins suggest the end of a movie in the seventh heaven. The couple got together eventually. How? You do not know since you had fallen asleep after the first sequence when he started to write an email ... Well, never mind: You have something in common with physicists and chemists! They often know from where a process like a chemical reaction started and where it ends, but they neither know the storyboard. You would just have to stay awake but for them it is more complicated. Scientists need very short and very bright X-ray pulses to watch their movies.

On a timescale of 20-100 femtoseconds (fs) the atomic nuclei 'stand still' while the much lighter electrons are still moving. Spectroscopy on the fs time scale is, therefore, able to detect the breaking and formation of electronic bonds as the nuclei move during a chemical reaction. In magnetic solids the electronic orbital motion is intimately linked to spin motion. Such spin-orbit forces ultimately determine the direction of spontaneous spin order as well as energy barriers for magnetization reversal especially of nanometer scale devices. Spectroscopy of spin and orbital motion on the fs timescale, therefore, opens up radically new ways for determining the ultimate speed of magnetization reversal of bits in magnetic data storage devices. On a microscopic level it is of interest to observe the transfer of energy and angular momentum between electronic, spin, and lattice degrees of freedom in atoms, molecules and solids. The use of optical fs laser excitation leads to the fascinating prospect of observing these processes in real time by stroboscopically 'imaging' the electron and spin motion, thus, separating the influence of lattice vibrations.

X-rays as a probe are especially suited for this purpose due to the inherent element specificity by involving electronic core levels. Resonant core-valence excitation also enables an orbitally resolved probe of the electronic structure. X-ray polarization control finally is the key ingredient in obtaining magnetic sensitivity which is nowadays routinely employed at 3<sup>rd</sup> generation synchrotrons for separating spin and orbital components of the magnetic moments. However, researchers were limited in time resolution due to the pulse length available at synchrotron radiation sources. 'To watch' the ultrafast changes in magnetization or chemical reactions shorter X-ray pulses are required.

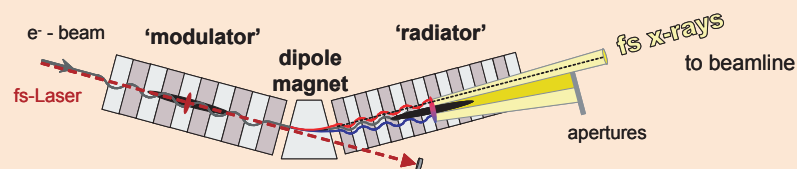


### Synchrotron radiation meets fs laser

Synchrotron sources do not radiate their X-rays continuously but rather produce series of short pulses. In time-resolved experiments the shortest observation time is given by the duration of the X-ray pulses. At present 3<sup>rd</sup> generation synchrotron sources, X-ray pulses are typically 50 picoseconds (ps) long. Shorter pulses down to just a few ps are available at BESSY during special operation conditions, the so-called 'low- $\alpha$ ' mode. The ultimate temporal resolution of <120 fs is reached with the Femtoslicing Source.

### Femtoslicing scheme

Femtosecond pulses from a Ti:sapphire laser system (wavelength  $\lambda = 780$  nm, pulse duration  $\tau = 50$  fs FWHM, pulse energy  $E = 2$  mJ, repetition rate = 1 kHz) co-propagate with electron bunches in a planar U139 undulator (the 'modulator'). The electric field of a 50 fs laser pulse induces an energy modulation of up to  $\pm 1\%$  to the 1.7 GeV electrons within an ultrashort 'slice' of the 50-70 ps wide bunch. Within our scheme the energy modulated electrons are separated from the major (99.9%) non-sliced part of the bunch by a dipole bending magnet. It serves for angular separation within the helical UE56 soft X-ray source (the 'radiator'). Picosecond radiation from the main bunch is blocked by front end apertures.



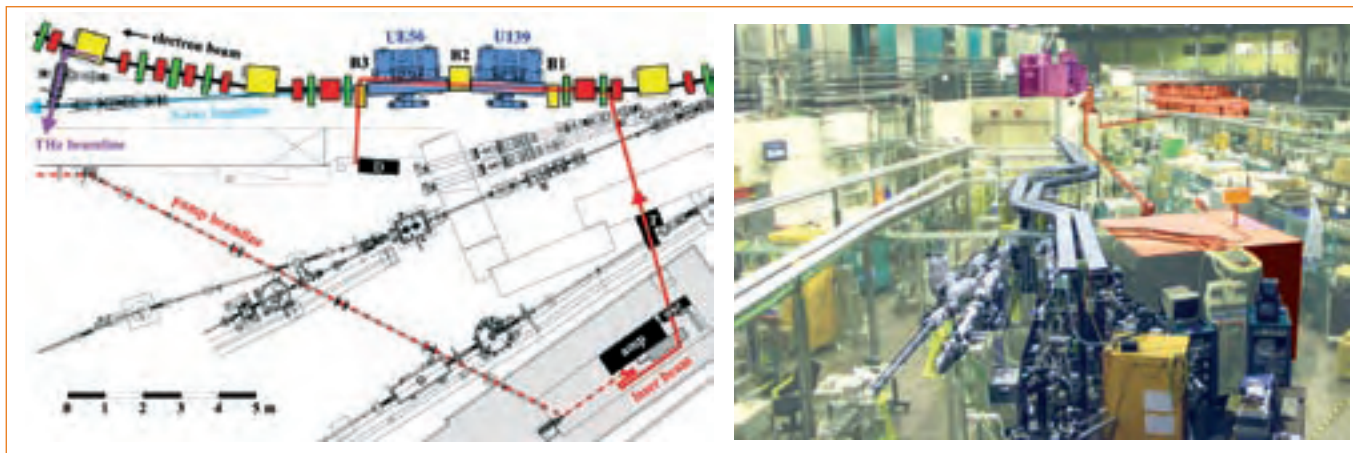


**Fig. 1:**  
**Left: Floorplan of the Femtoslicing source. The fs laser beam (red) is guided into the tunnel for 'slicing' the electron hybrid bunch within the U139 undulator. The 'pump'-part of the laser beam is transferred to the experiment (not shown).**

**Right: Photo of the installation with the experimental chamber in front, the laser hutch in the back (orange) and the THz setup (violet).**

Here, the electron pulse is 'sliced' with an optical femtosecond laser where the field of the laser pulse causes an energy modulation in the electron bunch [1]. In the BESSY scheme the energy-modulated electrons are separated from the main pulse in a dipole magnet and subsequently generate fs pulses by passing through a helical undulator (see box: Femtoslicing scheme). The price to be paid for the now improved time resolution (at storage rings) is a dramatic reduction in X-ray intensity since only  $10^{-3}$  of the electrons of the initial bunch are involved in the fs-pulse generation.

A major advantage of the Femtoslicing scheme is the inherent rigid temporal correlation between fs laser and fs X-ray pulses. This is due to the fact that the fs laser pulses used for the slicing and the pump processes originate from the same laser pulse (see box: experimental setup). The temporal phase between the laser pulse and the energy modulated electrons has to be preserved during propagation from the modulator to the sample. This translates into controlling the optical path length difference between optical and X-ray pulses by a distance better than  $30 \mu\text{m}$  (corresponding to 100 fs) over a distance of typically 50 m (Fig. 1).

The implementation of the Femtoslicing Source started in 2004 with the insertion of the two undulator pieces (U139 and UE56) and the set-up of the high power laser [2]. Beyond these challenges, the key ingredient of getting the facility up-and-running was to achieve the overlap of the electron bunch and the laser pulse in the modulator. It turned out that our experiences with coherent synchrotron radiation and THz radiation played a major role in opening the door to the fs-pulses.

## THz-Flashes

When the (optical) laser pulse hits the electrons, the path length differences of energy-modulated electrons also create a sub-ps density modulation in the longitudinal bunch profile, which gives rise to intense coherent THz pulses [3].

Using a dedicated THz beamline at a bending magnet 11 m downstream of the modulator (Fig. 1), strong pulses in the range up to 3 THz appear with each laser shot. The detection of the THz signal is a prerequisite for the generation of fs X-ray pulses. Featuring a high dynamics, these ultrashort THz flashes indicate a successful resonant interaction in the modulator, where the two beams (laser and electron beam, both having a diameter comparable to a human hair) have to co-propagate over a few meters with a temporal overlap of only some picoseconds.

We found at BESSY, that a THz flash returns after subsequent turns of the bunch along the storage ring lattice (240 m). The ratio of the THz intensity from the first and second turn sensitively depends on the initial energy modulation  $\Delta E/E$  of the electrons, a phenomenon which can be explained by momentum compaction and a resulting longitudinal expansion of the initial density modulation on the bunch. This 'afterglow' of the THz flashes is routinely used to maximize the energy modulation process prior to fs X-ray experiments on a shot-to-shot basis. The spectral shape of the THz flashes as measured by advanced rapid-scan Fourier Transform Spectroscopy techniques is employed to pre-tune the  $\sim 100$  fs length of the slice and hence, the resulting length and intensity of the fs X-ray pulses (see box: THz pre-tuning).

During routine operation of the fs X-ray facility, the laser-electron interaction is now stabilized over many days correcting for long term transverse drifts between laser- and electron beam and synchronous phase shifts

of the order of 20 ps of the decaying bunch. This is performed by feedback loops to keep the THz signal maximized by controlling two laser mirrors and the laser-electron timing.

### Properties of fs X-rays

The UE56 femtoslicing radiator is optimized for polarization dependent spectroscopy in the soft X-ray range. The fs X-ray flux for 0.1% bandwidth is of the order of  $10^4$  photons per second. Our fs undulator source allows for wavelength tuneability between 300 and 1,200 eV photon energy and for full polarization control. The polarization can be varied between linear (horizontal or vertical) and left and right handed elliptical.

The horizontal angular separation has been shown a successful concept of suppressing non-sliced undulator radiation from the desired fs soft X-rays. By choosing appropriate settings of the beam bend in the dipole magnet and the front end beamline apertures, we have succeeded to obtain very good fs-signal/ps-background ratios (up to 100:1) over the full photon energy range for either linear or elliptical polarization.

The UE56 X-ray source can still act as a **normal BESSY undulator** when the laser is switched off and using  $0^\circ$  beam bend allowing for pump-probe experiments with 70 ps temporal resolution and significantly higher photon flux, which is also an important feature for setting up a new fs experiment.

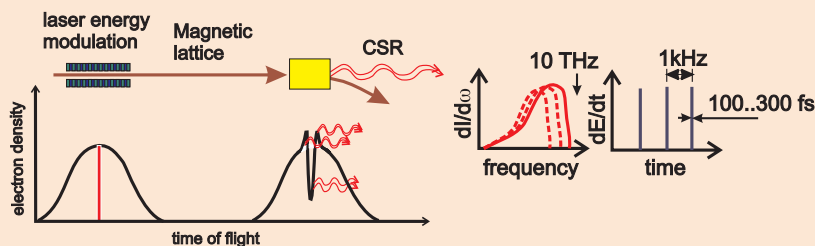
### Fs electronic motion in metals

As a first proof-of-principle experiment utilizing full polarization control of fs X-rays at the Femtoslicing Source we studied the ultrafast transfer of angular momentum between spins and lattice in ferromagnetic materials.

When energy is pumped into the electronic system of a metal by absorption of a fs laser pulse, electrons are excited into unoccupied states above the Fermi level. These electron-hole excitations will ultimately decay into phonons on a characteristic timescale given by electron phonon coupling ( $\sim 1$  ps). On intermediate times of several 100 fs an increase of the electronic temperature of a metal is observed while the lattice remains cold. This effect can be observed in fs X-ray absorption spectroscopy (Fig. 2). The X-ray absorption especially at the threshold energy changes during laser heating. The observed rise time is given mainly by the X-ray pulse duration since the response of the electrons to laser excitations is essentially instantaneous. Increasing the X-ray pulse length from the Femtoslicing ( $< 120$  fs) to low- $\alpha$  mode ( $\sim 10$  ps) and standard operation ( $\sim 50$  ps) is

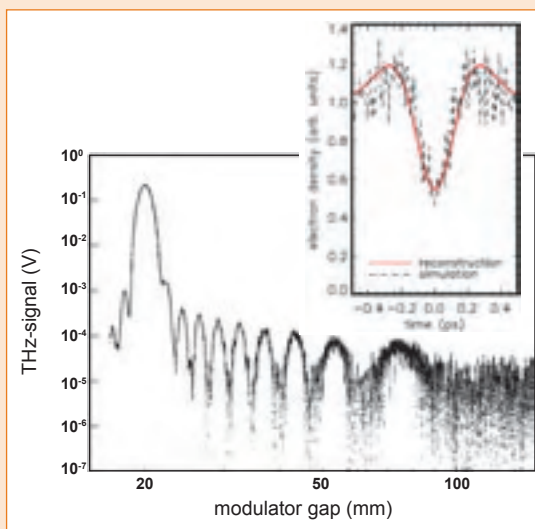
### THz pre-tuning

A coherent THz pulse is emitted on a bend magnet (THz-radiator, yellow) by a 'dip' in the electron bunch, left behind by the sliced electrons after propagating the magnetic lattice. Since other electrons emit only weak incoherent radiation in that spectral range, the coherent flash exceeds the radiation from all other bunches by many orders of magnitude. The spectral shape of the THz flashes is essentially the Fourier Transform of the 'dip'. FTIR spectroscopy is employed to pre-tune the  $\sim 100$  fs length of the slice and the initial energy modulation



Total THz pulse energy (emitted by a 'dip', i.e. electron-density modulation measured in the inset) while the resonance at 19.85 mm gap of the U139 has been slowly detuned to a maximum gap of 150 mm. The periodicity of the side bands corresponds to  $\lambda/N$ , where  $N=10$  is the number of periods and  $\lambda$  the fundamental wavelength.

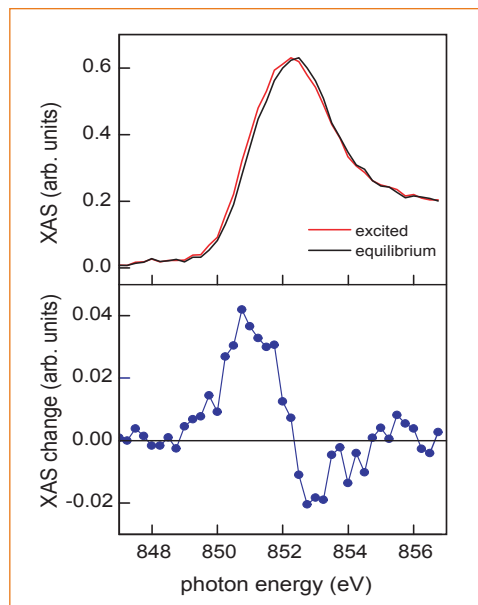
The measurements demonstrate that the resonance can be alternatively described as a convolution of the spontaneous undulator field and the laser field. Even if the undulator field is many orders of magnitude smaller, an interaction can still be detected. This high sensitivity of the THz signal is a key to establish and maintain the overlap between laser and electron beam necessary for fs X-ray experiments.



clearly seen in the decreasing slope of the so-called pump-probe cross-correlation scans (Fig. 3).

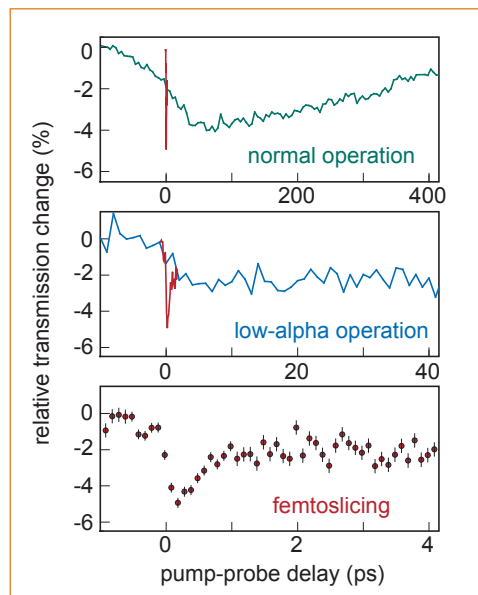
On  $\sim 1$  ps timescale the energy deposited in the electronic system is dispersed to the lattice, this relaxation process can be seen in Fig. 3 at corresponding times. On closer inspection the fs changes of X-ray absorption spectra cannot be explained by a heated electronic system alone. An increased electronic temperature would result in a broadening of the electron distribution at the Fermi level. This was clearly observed in time-resolved photoelectron spectroscopy with fs laser radiation [4]. Naively we would

**Fig. 2:**  
**Top panel:** Ni  $L_3$  absorption edge studied with 120 fs soft X-ray pulses. Red: IR laser pumped Ni film, black: laser off.  
**Bottom panel:** The difference between the laser pumped and not-pumped absorption spectrum reflects the observed peak shift of the Ni  $L_3$  edge.



expect to observe a similar broadening of the leading edge in X-ray absorption spectroscopy of Ni metal. This is not observed as can be seen in the time-resolved X-ray absorption spectra in Fig. 2. Instead the fs laser excitation leads mainly to a rigid shift of the absorption threshold towards lower X-ray energy. This is typical for a core level shift as it is observed for differing chemical environments. These data are, therefore, the first indication of a transient core level shift due to fs laser heating in metallic Ni. Presently we can only speculate about the microscopic mechanism for such an effect. It seems, however, reasonable to assume that the scattering of laser excited electrons could lead to an increased localization of itinerant Ni valence electrons.

**Fig. 3:**  
**Transient shift of the Ni  $L_3$  edge measured at the maximum of the laser induced difference curve (Fig. 2, bottom panel) vs delay time between laser pump and X-ray probe pulse. The bunch lengths are: 50 ps (top), 10 ps (middle) and 120 fs (bottom), with the latter superimposed on the two upper graphs (red line).**



#### References

- [1] R. W. Schoenlein et al., *Science*, **287**, 2237 (2000).
- [2] K. Hollnack et al., *Phys. Rev. ST Accel. Beams*, **8**, 040704 (2005) and S. Khan et al., *Phys. Rev. Lett.* **97**, 074801 (2006).
- [3] K. Hollnack et al., *Phys. Rev. Lett.*, **96**, 054801 (2006)
- [4] H.-S. Rhee et al., *Phys. Rev. Lett.*, **90**, 247201 (2003).
- [5] E. Beaurepaire et al., *Phys. Rev. Lett.*, **76**, 4250 (1996).
- [6] A. Vaterlaus et al., *Phys. Rev. B*, **46**, 5280 (1992).

## Ultrafast heating of a ferromagnet

Optical transitions are usually spin conserving, even in a ferromagnetic material. In this respect the first observation of fs laser induced demagnetization of ferromagnetic Ni [5] has attracted enormous interest. Applications such as magneto-optical recording could become feasible on sub-ps timescales. These results raise the fundamental question about angular momentum conservation on ultrafast timescales. Since the electron spin represents an angular momentum quantum, any quenching of spin angular momentum by fs laser excitation must lead to an increase of angular momentum in another particle reservoir. It has been argued that spin angular momentum can be transferred to the lattice only on significantly longer timescales of  $\sim 100$  ps [6]. On the fs timescale quenching of spin angular momentum should then be accompanied by an increase of orbital angular momentum. In the ground state the orbital motion of electrons contributes by only  $\sim 20\%$  to the total magnetic moment in 3d transition metal ferromagnets. It could, therefore, act as a sink for angular momentum even on the fs timescale.

X-ray magnetic circular dichroism (XMCD), i.e. the difference of X-ray absorption between left and right circularly polarized X-rays in ferromagnets, is the ideal tool to observe such effects. For instance, at the Ni  $L_3$  absorption edge sum rules relate the XMCD intensity to linear combination of spin,  $S$ , and orbital,  $L$ , angular moment as  $2S+3L$ . The fs temporal evolution of the quantity,  $2S+3L$ , following the absorption of a fs optical laser pulse. It represents the first direct demonstration that  $S$  is transferred to the lattice and not to  $L$  on a  $\sim 100$  fs timescale (Fig. 4). This can be visualized for the following scenario, considering that in thermal equilibrium (at negative time delays in Fig. 4)  $L$  is typically only about 20% of  $S$ . The  $\sim 80\%$  decrease of  $2S+3L$  during the first ps is then mainly due to the reduction of  $S$ . If this change in  $S$  would be completely compensated by  $L$ , the quantity  $2S+3L$  would actually increase by about 20% in contradiction to the measurements. The important conclusion drawn from the data in Fig. 4 is the existence of an ultrafast channel for transfer of spin angular momentum to the lattice. In analogy to the well known Einstein-de Haas-effect, a small suspended ferromagnet would start to rotate upon laser induced demagnetization (schematically shown at the top of Fig. 4).

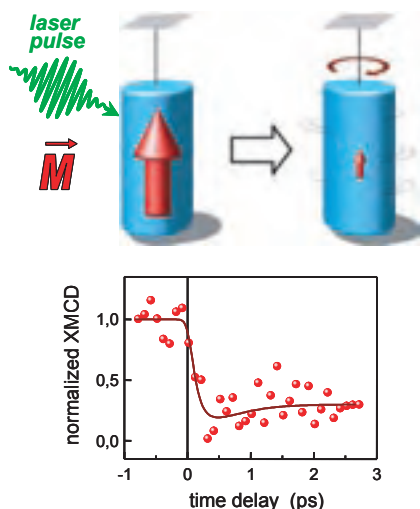


**Fig. 4:** Transient normalized XMCD of the Ni  $L_3$  edge vs delay time between laser pump and X-ray probe pulse. The curve is taken with elliptically polarized fs soft X-rays. The upper part illustrates the concept of angular momentum conservation upon laser induced demagnetization (Einstein-de Haas-Effect).

### Where we are and where to go ...

Employing X-ray pulses of fs duration from the BESSY Femtosing Source and the laser for well correlated pump-probe experiments, we were able to demonstrate an ultrafast transfer of angular momentum between spins and lattice in ferromagnetic materials. This allows a glimpse at the future use of intense fs X-ray pulses from the planned BESSY soft X-ray Free Electron Laser source.

The results also show that the required level of stability of the laser-synchrotron setup can indeed be achieved. The Femtosing Source can be considered as a new user facility allowing for pump-probe experiments with X-rays (between 300 and 1,200 eV photon energy) and THz radiation on a sub-ps timescale

For more sophisticated experiments involving more intense pulses, however, it will be of paramount importance to avoid the intensity losses due to slicing. This can be achieved using linear accelerator based X-ray sources since the electron bunches are used only once for X-ray generation and can, therefore, be compressed down to sub-ps duration. In free electron laser (FEL) sources, the bunches contain enough electrons so that the resulting ultrashort X-ray pulses become coherent like a conventional laser.

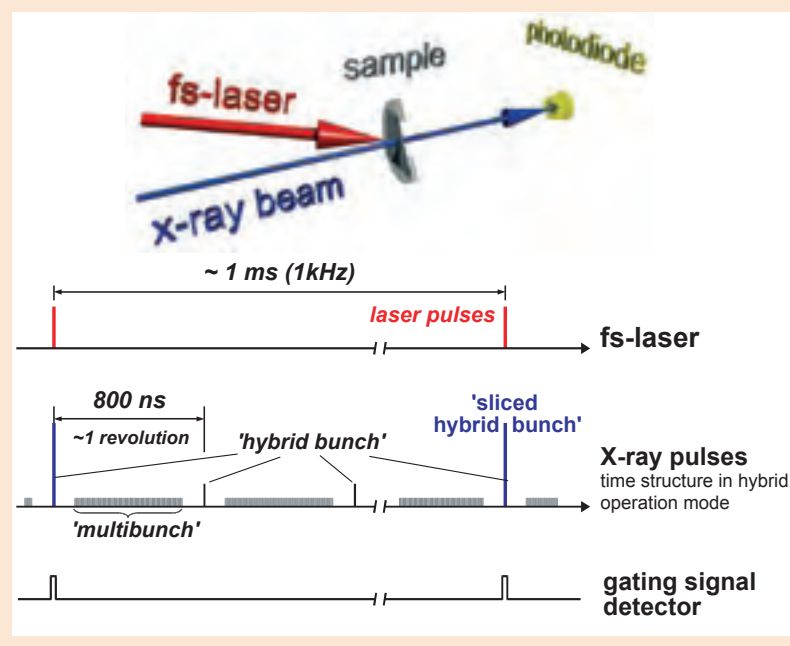
In the proposed BESSY soft X-ray FEL, the lasing process is induced by seeding the electron bunches by external optical fs laser

### Experimental setup

A scheme of the experimental XAS setup is shown in the upper part of the figure. A 30 nm Ni-film deposited on a 500 nm thick aluminum membrane is carried by an aluminum frame. X-ray absorption spectra of the Ni-film are recorded by measuring the transmitted X-ray intensity by an avalanche photodiode. For XMCD measurements, an external magnetic field can be applied to the sample by an electromagnet.

Laser-induced ultrafast excitation and subsequent relaxation processes are studied employing the pump-probe principle. A well defined time prior to the arrival of the X-ray probe pulse a laser pulse focused on the probed area excites the sample. Recording X-ray absorption at a particular X-ray photon energy for a sequence of different time delays between pump and probe pulse images the progression of laser induced dynamics. The relative time delay is controlled by changing the geometric path length of the laser pulse ( $1 \mu\text{m} \approx 3.3 \text{ fs}$ ).

The effective repetition rate of the experiment is determined by that of the laser. The laser is electronically synchronized to the synchrotron within less than the hybrid electron bunch width. Intrinsic synchronization of the fs laser pump and the fs X-ray probe pulses is obtained through the slicing process. An efficient suppression of remaining X-ray intensity from non-sliced electron bunches requires time gating of the photodiode (lower part of the figure).



pulses. This new FEL principle utilizes the fact that the time structure of an optical fs laser pulse can be 'imprinted' upon an electron bunch in a way very similar to the Femtosing principle. In a sense the BESSY Femtosing Source represents the first step towards a seeded soft X-ray FEL including the required development of suitable electron bunch diagnostics capable of measuring a fs charge modulation of electron bunches.

So, while we are waiting to be able to watch the whole movie using Free Electron Lasers, with Femtosing we can now get the first glance of the storyboard ... and this is already very exciting.

### The Femtosing Team:

Herrmann Dürr  
Karsten Holldack  
Torsten Kachel  
Shaukat Khan\*  
Rolf Mitzner°  
Niko Pontius  
Torsten Quast  
Christian Stamm

\* now Univ. Hamburg  
° Univ. Münster

The significant changes within the design and modifications of machine, undulator, beamline and detector have been facilitated by a joint effort of many more BESSY staff members.

**Contact:**  
femtosing@bessy.de

## Facility Report

## Machine Operation

During 2006 the accelerator/storage ring complex operated smoothly and without any severe failures of major components. The reliability was as high as usual leading to an availability of well above 96%. The only noteworthy exception was an interruption of the cooling water supply which led to problems with the cryogenic cooler for the liquid Helium supply in late November. When the superconducting insertion devices were brought back into operation after this failure, the high temperature superconducting current feedthroughs of the PSF-WLS burnt through and it will take until the beginning of 2007 to replace them.

Some minor interruptions during the year were caused by the increasing complexity of the operational requirements. i.e. the daily demand for the hybrid filling pattern with a single bunch of 10 mA in the 100 ns dark gap, the optics modifications for the low- $\alpha$  operation with much shorter bunches which has been offered four times last year, and during certain weeks the desired frequent changes of the closed orbit bump for the fs-slicing in order to switch the beamline between different user groups.

The procedures how to achieve the demanded hybrid filling pattern with a single bunch in the dark gap have been settled. At the beginning of the year the gun was improved and the resulting higher stability led to acceptable injection times for the single (hybrid) bunch. In addition, the total beam current in routine operation could be increased to the legislative limit of 300 mA (Fig. 1). Switching between different optics (i.e. normal operation vs low- $\alpha$  with shorter bunches) has become routine, and work on improving the procedure for the fs-slicing bump is progressing.

### New Insertion Device – UE112

In low energy storage rings APPLE II-type undulators with large period length, like the recently installed UE112, can have a negative impact on the horizontal beam dynamics especially when they are set for vertical polarized radiation. BESSY has developed expertise in the modelling, compensation, and measurement of these effects. For UE112 three iterations were required in order to find a satisfactory shim configuration which nearly restored the horizontal dynamic

aperture of the ring (Fig. 2), a prerequisite for efficient top-up injections. A new dipole vacuum chamber was installed down stream of the ID and cooling of the Cu-chamber was improved. Radiation of UE112 with large vertical opening angle can be extracted through the enlarged vertical slot of the chamber. Tests have shown that this ID can safely operate in all possible modes now.

### News on topping-up

In the top-up operation mode lost electrons are replaced after minutes and not after a couple of hours as it is done today. High injection efficiency and small orbit perturbations during these injections are mandatory in order not to disturb the users. BESSY II was not designed for this mode of operation but work continues to master some of the challenges and to enable test operation in this mode for some beamlines at the end of 2007.

Currently, the injection efficiency is limited by IDs at small gap and by additional non-linear field components of the storage ring that reduce the horizontal acceptance of the ring. Also, the horizontal orbit distortions during the many top-up injections will be rather large. Some improvements can be achieved in the near future by less invasive means i.e. improvements of the pulsed power supplies of the injection elements and improvements of the synchrotron. Major modifications, like the replacement of the pre-injector microtron by a linear accelerator (LINAC), the improvement of the shielding of septum stray fields, or the relaxation of the injection geometry require interruptions. The targeted top-up injection efficiency and a quieter beam during injections, similar to the level achieved at other facilities, can be also achieved at BESSY. Until then, users are advised to prepare their experiments and data acquisition procedures in order to take the blank pulse provided synchronous to the top-up injections into account.

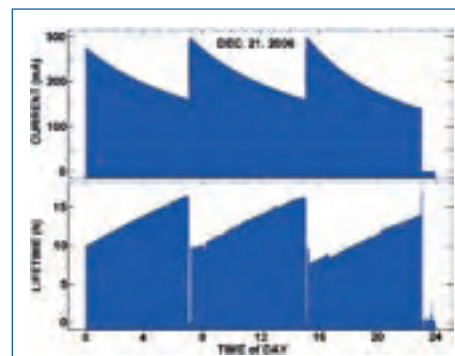


**Fig. 1:** The last day of user operation in 2006. Injections are scheduled every 8 h and beam is injected up to 300 mA, 10 mA are kept in a single bunch in the middle of the dark gap.

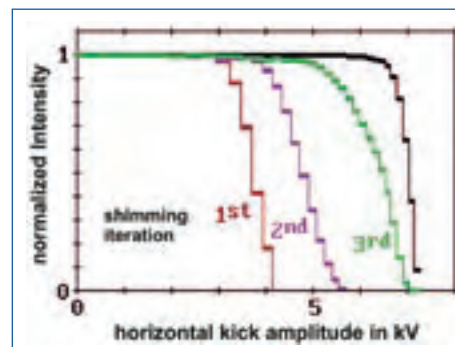


**Fig. 2:** Impact of the UE112 on the horizontal dynamic aperture for the 3 iterations of the shimming process in comparison to the aperture without ID (black). The plot shows the remaining normalised intensity of the beam after applying single horizontal kicks with increasing strength. The ID was set for linear vertical polarized radiation at the smallest gap.

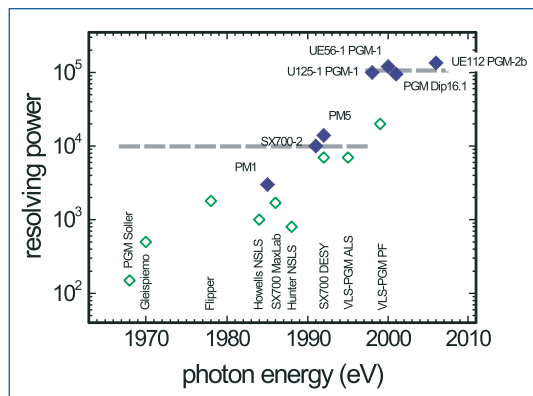


**Fig. 3:**  
Evolution of plane grating focusing.

and undulators and the diagnostic equipment attached has to be transparent in a sense that the determination of a couple of parameters like e.g. photon energy, energy resolution and polarization state of the light incident on the sample is sufficient for the user to run the experiment.

Parallel to these improvements, a new, EPICS based software was developed which is now being tested at the beamlines UE49 PGM and U41 PGM. This software handles the control panels for selecting the beamline parameters (including insertion device and monochromator) and the data acquisition software separately. A change of any beamline parameter does no longer require a parameter reset on the data acquisition programme. Upon successful testing the implementation of the new control software will start in 2007.

Although still operated with linearly polarized light, the new **plane grating monochromator** at the recently installed UE112 showed its extraordinary performance. With a value of 135.000 at 64.2 eV we established a new world record in resolving power with this instrument. The foundation for this result was laid in the early days of BESSY I, when Helmut Petersen developed the plane grating focusing scheme for the soft X-ray region. By applying this scheme to the well known SX-700 monochromator, BESSY could offer a resolving power of about 10<sup>4</sup> (at 64 eV of photon energy), already at that time a competitive result. With the developments in the optical beamline design, the performance of the angle encoders involved, the drive units and, last but not least, the ex-situ and in-situ surface metrology, accompanied by a reduced electron beam emittance, the

transition from BESSY I to BESSY II resulted in an improvement of the resolving power by about one order of magnitude (Fig. 3). The achieved energy resolution of better than 1 meV at the UE112 PGM is the first step of a joint project with IFW and TU Dresden to establish the 1<sup>3</sup>-ARPES experiments to investigate the electronic structure of high-T<sub>c</sub>-superconductors at 1 meV photon energy resolution, 1 K sample temperature, and 1 meV electron energy resolution.

Another collimated plane grating beamline was put into operation at a dipole source at segment 04. The **ISS collaboration** (Innovative Station for In Situ Spectroscopy) of the Fritz-Haber-Institut der Max-Planck-Gesellschaft will perform catalysis studies under operation conditions of the catalyst being close to reality. Since the studies require a complex sample pre-treatment, the experimental area is completely separated from the experimental hall. The hutch has been built during the shutdown in spring 2006, and it has been completed by the end of the year. Beamline and experimental area are now matter of detailed characterization (Fig. 4).

Since the first days of BESSY 1, **X-ray microscopy** has developed to play a dominant role among the applications of synchrotron radiation at BESSY. Based on the pioneering work of G. Schmahl's group at the Göttingen University, an X-ray microscope was built at BESSY II that utilised a three-mirror-system, two of them rotating around the optical axis, to generate a hollow cone illumination matching the aperture of the objective to that of a condenser, used to monochromatize the synchrotron light, to fully exploit the high brilliance delivered from the U41. In order to meet nowadays and future requirements of our users, the instrument has been significantly improved. A spherical grating monochromator replaces the condenser zone plate to generate monochromatized light at high spectral purity, and a capillary optics generates the hollow cone illumination. The new experimental setup is based on a tilt stage originally developed for electron tomography which supports automated data collection of cryogenic and heated samples. The object stage permits to tilt the sample in the X-ray microscope by ±80°. The instrument has already been successfully tested, resulting in a focal spot size of 0.7 x 1.5 μm<sup>2</sup>. The new setup is currently under construction and will be operational in spring 2007.



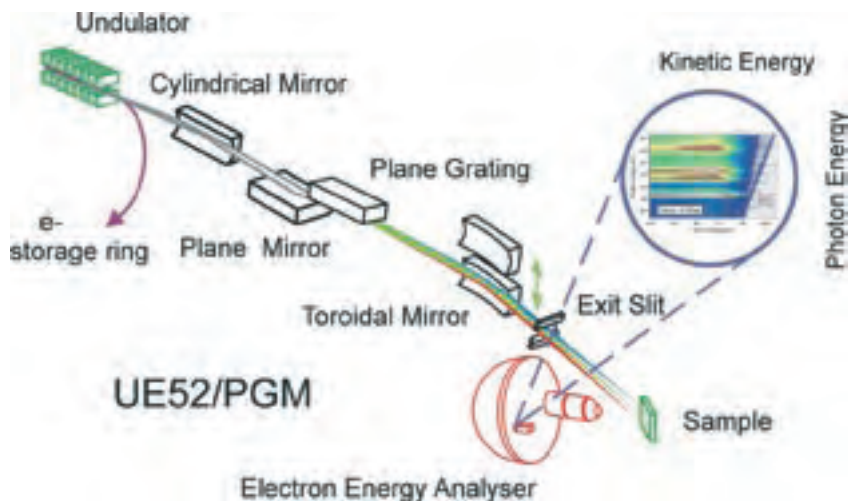
**Fig 4:**  
Joint collaboration characterizing a new beamline.

Two additional X-ray microscopes will be installed at a branch line available at the UE46. This work is carried out in collaboration with MPI Stuttgart. A new collimated PGM will be installed starting in September 2007. Its branch lines will serve two X-ray imaging stations being alternatively used. Both instruments will be put into operation early in 2008.

Our studies on the influence of liquid nitrogen cooling on the grating performance delivered promising results and inspired the design of a new **high performance spherical grating beamline**, which will serve as a source for resonant and coherent X-ray scattering experiments. This beamline will be installed at the UE49. The number of optical elements involved will be reduced to the minimum required to disperse and focus the synchrotron radiation down to a spot size of  $4 \times 1 \mu\text{m}^2$ , thus delivering the highest possible photon flux. The result of the intensive grating tests is a layout, where the spherical substrate with three variable line space (VLS) gratings is the first optical element hit by the synchrotron light. The challenge is to cool the grating sufficiently to avoid distortions of its surface due to the heat load from the insertion device.

UE49 also serves the plane grating beamline for photoemission microscopy. The **SP-PEEM (Spin-Polarized Photoemission Electron Microscope)**, operated by a BESSY research team, has already demonstrated a lateral resolution of 32 nm and recorded topological and magnetic contrast mechanisms of a Ni film exploiting the full control on the polarization state of the light delivered by the insertion device.

In spring 2007, the **UE52 PGM beamline**, operated by a cooperating research group located at Würzburg University, will be modified. A new focusing mirror chamber will be installed housing two mirrors. One mirror will still focus the dispersed light into the exit slit plane to perform standard absorption or photoemission experiments. A second mirror which can be used alternatively focuses the dispersed light on the sample. Combining this photon energy dispersion on the sample with the imaging properties of the hemispherical electron energy analyser, energy dispersive electron spectroscopy will be available. This multiplex technique allows the utilization of NEXAFS and XPS without the need of time-consuming scanning of the



photon energy (Fig. 5). Thus, changes on short time scales may be monitored with full spectroscopic information.

**Fig. 5:**  
Dispersive NEXAFS mode of operation

BESSY's experimental setup for high energy resolution high kinetic energy photoemission (HIKE) is now operational. Immediately after commissioning, the capacity of this new technique could be demonstrated by investigating buried interfaces, exploiting the shift of core levels at an interface with respect to the bulk material (see also the contribution of Gorgoi et al. in this Highlights edition).

During 2006, the **LIQUIDROME**, a new experimental station dedicated to investigations on liquid and degassing sample (Fig. 6) was put into operation. With the detectors attached (a Si drift detector and a GaAsP-diode), soft X-ray NEXAFS spectra can be recorded either at a pressure of about  $10^{-6}$  mbar or up to 1,000 mbar under He atmosphere. For the data analysis a whole package of software codes is available to calculate spectra for comparison for various electronic structures.

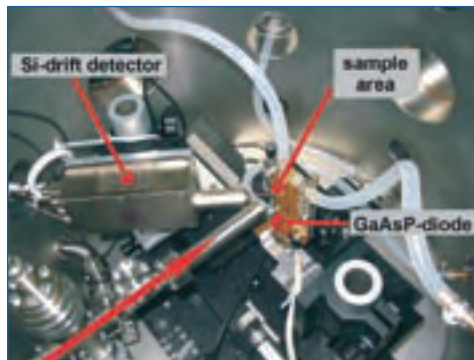


**Fig. 6:**  
LIQUIDROME – a new experimental setup for liquids and degassing samples.

**Contact:**

Christian Jung  
christian.jung@bessy.de

## STARS shining bright - the status of the BESSY-FEL Project



**Fig. 7:**  
Layout of STARS with two cascaded HGHG stages

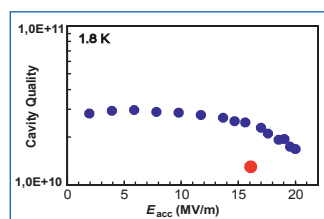
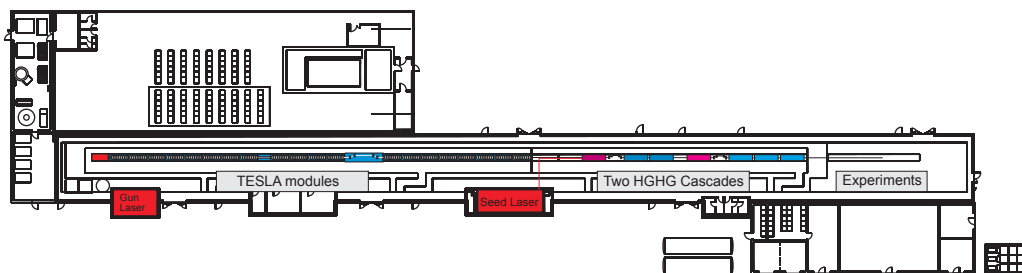


**Fig. 8:**  
Test of a fully dressed TESLA cavity under CW operation conditions. Red spot: Targeted operating point for BESSY-FEL.

The Technical Design Report (TDR) for the BESSY Soft X-ray Free Electron Laser (FEL) user facility in the photon energy range from 24 eV to 1,000 eV was evaluated by the Wissenschaftsrat (German Science Council) in 2005. The BESSY-FEL is based on a cascade of seeded high-gain-harmonic-generation stages and currently offers the only possibility to generate photon pulses of variable femtosecond duration, gigawatt peak power, full shot-to-shot pulse reproducibility, wide-range tunability and full transverse and longitudinal coherence. The BESSY user community is convinced that only a HGHG 2nd generation FEL will be able to fulfill all of these crucial requirements for the next generation of experiments.

In May 2006 the Wissenschaftsrat published its recommendation on the BESSY-FEL project and highlighted that the project is at the 'forefront of international research and will have a strong impact on basic as well as applied science' and strongly advised to setup of a two-stage HGHG cascade to demonstrate the feasibility in an R&D program spanning 3 to 4 years. We have eagerly taken up this recommendation and in 2006 presented a proposal for the proof-of-principle facility – STARS\* – for two cascaded HGHG stages (Fig. 7).

STARS encompasses many of the components of the BESSY-FEL. A high-brightness normal-conducting photoinjector produces the electron beam, which is accelerated by CW-adapted TESLA modules to 325 MeV. A bunch compressor ensures that the required peak current for efficient lasing is achieved. Finally, a two-stage HGHG cascade will lase in the wavelength range 40-70 nm producing 30 fs fully coherent light pulses. The use of a variable-gap APPLE-III undulator ensures full polarization control, as for the BESSY-FEL.

Although the primary function of STARS is to demonstrate the cascaded HGHG scheme, many of the components and technical

issues for STARS are identical or very similar to those of the BESSY-FEL. As a 'bonus', STARS will therefore serve as an ideal demonstrator for a number of components.

In preparing for the FEL and STARS, BESSY has therefore been pursuing an aggressive R&D program for the key components. This includes the development of a high-repetition-rate normal-conducting photoinjector as part of the EuroFEL collaboration and the participation in the FZR-DESY-MBI-BESSY collaboration for the development of a superconducting CW injector.

One of the main areas of research is development of TESLA technology for full CW operation. To this end, the HoBiCaT Test

Facility has been operating for several years. It allows the CW operation of two 'fully dressed' TESLA units under BESSY-FEL operating conditions. One of the critical issues is the fact that the dynamic heat load is one to two orders of magnitude greater than for pulsed operation. This puts an additional thermal strain

on components and impacts the size of the refrigeration plant significantly.

Recent tests, in collaboration with DESY and Jefferson Lab, of a fully dressed TESLA cavity (input coupler, liquid helium tank, HOM couplers, tuner) have demonstrated that CW operation up to 20 MV/m is possible (Fig. 8). Here, quality factors more than 80% higher than those planned for the BESSY-FEL were achieved, potentially leading to a huge savings in cryogenic power. Modifications of the helium tank have been identified that will permit operation at even higher field levels.

BESSY's experience with the Femtoslicing source has also demonstrated that we are capable of achieving and controlling the overlap of a fs laser with relativistic electrons (see Special on Femtoslicing). Thus, in a sense, we have already operated the first stage of an HGHG FEL in a storage ring. We are therefore confident of achieving our goal of operating a two-stage cascaded FEL within the next 3-4 years.

### The STARS design group

#### Contact:

Jens Knobloch  
jens.knobloch@bessy.de

#### Acknowledgements:

We have benefited greatly from discussions, comments and suggestions made by colleagues from Germany (DESY, MBI, TU-Darmstadt, TU-Dresden) as well as from abroad (ALS, APS, BNL, Cornell, ELETTRA, ESRF, INFN Milano, JLab, Maxlab, MIT Bates, CEA Saclay, SLAC, IPN Orsay and UCLA).

## The Metrology Light Source (MLS) of the PTB

Last year we have seen significant progress in the construction of the 600 MeV electron storage ring of the Physikalisch-Technische Bundesanstalt (PTB). The storage ring building was completed and handed over by the Bundesamt für Bauwesen und Raumordnung (BBR) into the responsibility of PTB. Inside the building, the construction of the MLS by BESSY progressed rapidly and is now almost completed.

In detail, all storage ring magnets have been delivered and the magnet girders have been aligned in the storage ring bunker (Fig. 9). The four segments within the magnet girders have been assembled and installed after ex-situ bake out. Also the straight vacuum section containing the rf cavity is completed.

The rf and injection components as well as the transfer line from the microtron to the storage ring were installed. Commissioning of the 100 MeV injection microtron, delivered in autumn 2006, showed that main parameters comply or exceed the specifications, e.g. a current of more than the specified 8 mA has been accelerated to 100 MeV (Fig. 10).

Components for the frontend systems have been supplied and major parts have already been mounted and placed in the storage ring tunnel. Most vacuum components for the planned IR and THz beamlines been partly installed in the storage ring bunker. The optical components for these beamlines have successfully passed acceptance tests.

In order to use of the MLS as a primary source standard for calculable synchrotron radiation we have to measure all storage ring parameters with a high accuracy. Important parts of instrumentation for the measurement of these parameters such as the parametric current transformer for the measurement of the electron beam ring current at high values have been installed already. The system for electron beam current measurement at very low values or for single electron counting is currently under construction and the  $\text{CO}_2/\text{CO}$  - laser as the central component of the electron energy measurement system has been specified and will soon be delivered.

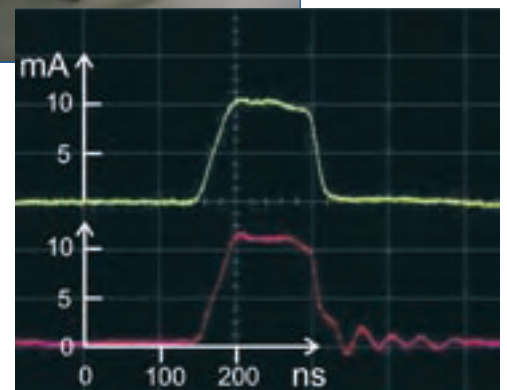
We are very confident that the commissioning of the storage ring can start as planned in spring 2007. User operation is scheduled to start at the beginning of 2008.



**Fig. 9:** One of four magnet sections with the vacuum chamber system installed. The upper part of the multipole magnets has been removed for the vacuum chamber installation.



**Fig. 10:** 100 MeV injection microtron installed in the microtron bunker. The inlay shows a measurement of the current pulses of the microtron at two positions in the transfer line during commissioning. The specified value of 8 mA for the current pulses is even exceeded.



### Contact:

Roman M. Klein  
[Roman.M.Klein@ptb.de](mailto:Roman.M.Klein@ptb.de)



User Pages

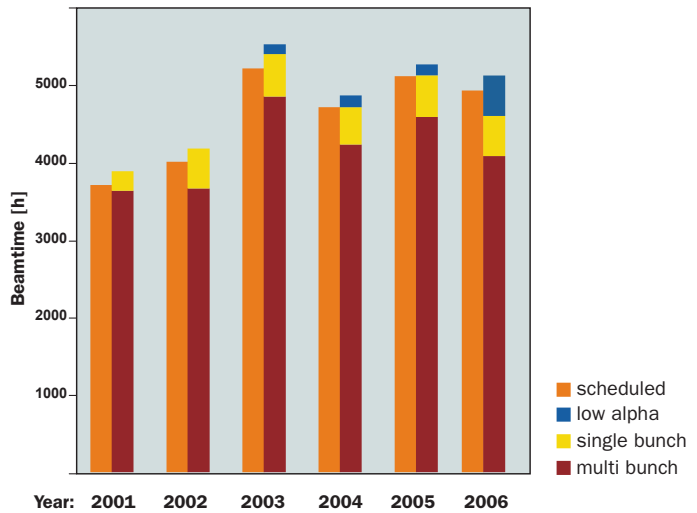
# Operation Statistics

In 2006, we scheduled 4,900 operation hours, somewhat less than in 2005 owing to a necessary four week shut-down in spring to install the new undulator UE112. By the end of the year we had delivered almost 5,100 user operation hours, thereof were four weeks of low- $\alpha$  and single bunch operation mode, respectively, due to the rising demand of short pulses and THz-radiation.

In total 7,939 beamtime shifts of 8h at 26 ID beamlines and 5,912 shifts at 14 bending magnet beamlines were delivered. The graphs show the main research areas and the distribution of the provided beamtime with respect to different user institutions and funding programs.

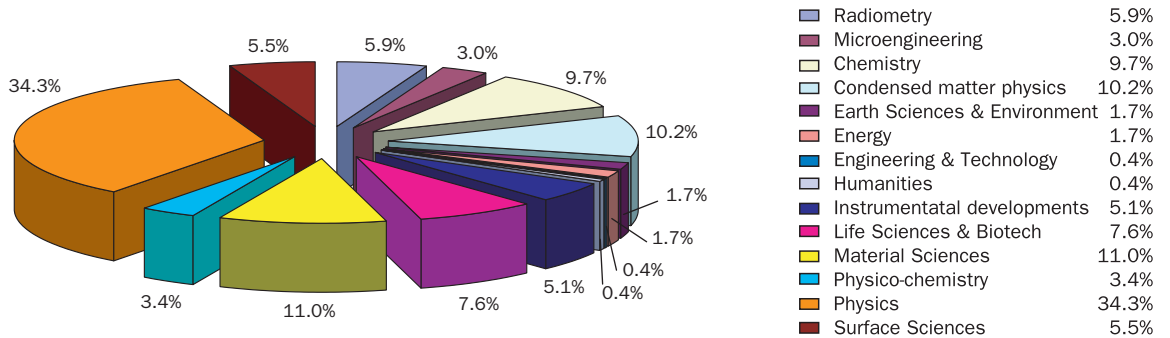
A total number of 834 proposals have been submitted via BOAT (BESSY Online Access Tool) of which 203 had to be rejected. For the remaining 631 accepted proposals we scheduled 654 user runs. More than 1,200 external researchers used BESSY for their studies representing an active scientific community, among them were 23% from EU countries funded by the EU-13 program. The life sciences community increased to about 13% of the total users.

## Beamtime at BESSY



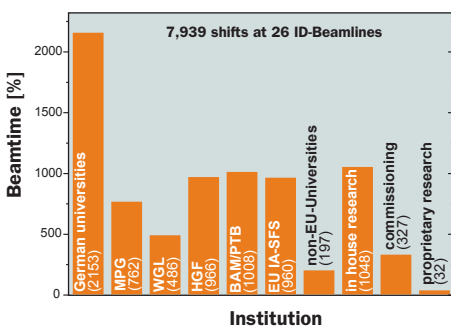
## Main Research Areas

### Number of Projects

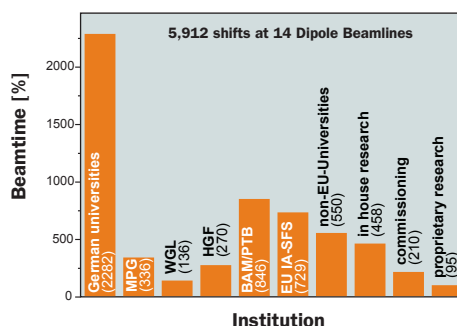


## Beamtime allocation in 2006

### Insertion Device Beamlines



### Bending Magnet Beamlines



MPG = Max-Planck-Gesellschaft  
 WGL = Leibniz Gemeinschaft  
 HGF = Helmholtz-Gemeinschaft  
 BAM = Bundesanstalt für Materialforschung und- prüfung  
 PTB = Physikalisch-Technische Bundesanstalt  
 EU IA-SFS = Integrating Activity on Synchrotron & FEL



## Improvements for Users

### Accidents don't just happen – they are caused.

With this statement we introduced the new interactive safety instructions, which are accessible in our library at all time. Their implementation is part of our intensified efforts to guarantee safe working conditions by informing about the safety regulations valid at BESSY.

It is our aim to help our users to perform their experiments as safe and efficient as possible. Nevertheless, the working conditions inside the storage ring hall are still not satisfactory. Not only during our inspections, carried out from time to time throughout the entire experimental area, we find limited admittance to safety installations like fire extinguisher or emergency switches, cardboard boxes or wooden packages for transportation, improper wiring of power supplies for the experimental equipment, including cables spanned across the experimental area, peaceful – but dangerous – coexistence of food and chemicals, and other violations of the safety regulations.



Performing experiments at BESSY requires the coexistence of about 50 user groups, with the local experimental areas lying close together. Safe working conditions thus are the fundamental basis for the efficient use of the beamtime.

On the basis of the weekly beamtime schedule we have improved our user support. During normal user operation, starting at 7:00 h Tuesday morning and lasting now until 23:00 h Sunday evening, user support, well known as *Hallendienst*, and operator service are available without interruption.

All relevant information and announcements concerning the user operation and the status of the storage ring is displayed via the monitor system, which has been recently updated. Since this monitor system is a kind of interface between *Hallendienst* and users,

it must fulfil certain requirements, in particular, it needs to be visible from the users local experimental area. Although quite a lot of TV sets are spread throughout the entire experimental area and the office buildings, it is sometimes hard to see one of them. We thus now offer the option to get the information pages on the local computer via an internet browser ([infosystem.bessy.de/monitor.html](http://infosystem.bessy.de/monitor.html)).

Currently, BESSY offers three different **modes of standard user operation** (Fig. 1):

- multi bunch hybrid mode; high photon flux plus (0.7 mA per bunch) plus single bunch (5 mA) for pump-probe experiments using the fs-slicing facility
- single bunch operation; time resolved experiments (two times two weeks every year) typical 20 mA, time resolution 800 ns
- low- $\alpha$  multi bunch hybrid mode four times a year for three days each time; 40  $\mu$ A per bunch for all bunches.

All three modes require keeping the position of the single bunch injected constant throughout the entire beamtime. Thus, a lot of care has been taken in the past to develop instruments, which allow for the monitoring of the single bunch position in order to keep it unchanged from fill to fill. In addition, for single bunch operation it is required to keep the bunch purity on the highest possible level. Currently, the purity is about 1,000 after injection, and it decreases by about a factor of two during the fill. To determine the fill pattern and to obtain single bunch position and purity, a time controlled single photon counting setup has been implemented in the storage ring. For future single bunch operation it is planned to display both values via the monitor system.

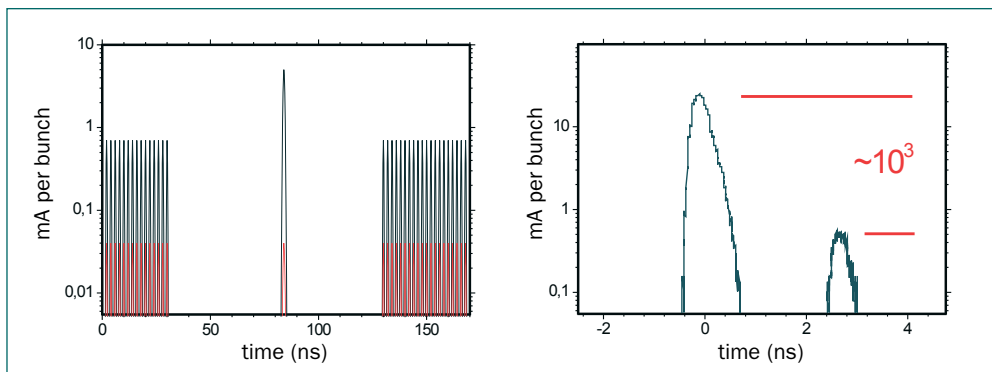


**Fig. 1:** Single hybrid bunch in the dark gap for normal operation mode (black) and low- $\alpha$  mode (red). The bunch purity after injection is 1,000 for single bunch operation (right panel).

From the time BESSY has taken responsibility for the **protein crystallography beamlines**, the infrastructure available for these experiments has been significantly improved. At beamline 14.1, a new mosaic detector with an active area of 225 x 225 mm<sup>2</sup> and a dynamic range of 16 bit has been implemented, and an improved software interface is available for a more efficient handling of the instrument. In addition, the acquisition of components for a highly standardized automated sample handling has started. The access to the facility is now available via BOAT. Users can schedule beamtime themselves, and they can easily prepare their beamtime after allocation. For the beamline management, the resources can be managed with much higher efficiency.

Since the end of 2006, BESSY is authorised to operate the **biology laboratory** (Fig. 2) located at the cargo port. The laboratory allows open handling of biological samples and genetically modified organisms within lowest safety levels. Users planning to prepare samples for their experiments in the BioLab are asked to submit the safety registration leaflet at latest three weeks before their beam time begins. Before they start working in the lab, they will be instructed about the special safety regulations. For the future it is planned to handle the beam time registration via BOAT, and to offer the safety instructions as a module within the interactive instructions.

Moving further towards higher brilliance, microfocus and automated operation, contemporary X-ray beamlines require excellent stability of the monochromatic beam. In collaboration with partners from several European Storage rings (BIOXHIT Project) and the company Micron Semiconductor, UK, BESSY and the Free University Berlin have developed a new transmissive two-dimensional **X-ray beam position monitor**, to be implemented in a fast feedback system.

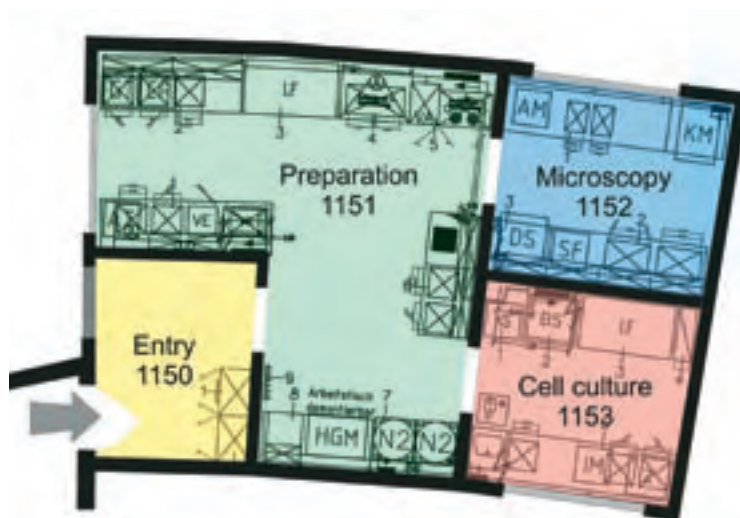


**Fig 2:** Sketch for the Biology Laboratory

The monitor is based on a position sensitive detector (PSD), thinned down to a thickness of about 5  $\mu\text{m}$ . Although this large area detector absorbs only a few per cent of the incident beam, its response allows for stabilization of the beam on a sub-micron scale. The detector transmission varies between 15 % at 2.5 keV and 93 % at 10 keV.

Finally, we have improved the support at the parking zones for experimental stations. For most of these zones, electric power, cooling water and compressed air are now available for a proper preparation of the beam time allocated. Since free space is a highly limited resource inside the storage ring hall, the claims for occupying parking zones have to be coordinated by the user support.

#### User Committee:

Ralph Püttner (Chairperson)  
Freie Universität Berlin  
Birgit Kanngießer  
(Vice-Chairperson)  
Technische Universität Berlin  
Peter Baumgärtel  
Universität Potsdam  
Wolfgang Braun  
Paul-Drude-Institut  
Ralf Feyerherm  
Hahn-Meitner-Institut

## ID Beamlines at BESSY (January 2007)

Further information on beamlines can be found on the 'user info pages' of the BESSY website

BAM  
Bundesanstalt für  
Materialforschung  
und -prüfung

BTUC  
Brandenburgische  
Technische  
Universität Cottbus

FUB  
Freie Universität  
Berlin

FZJ  
Forschungs-  
zentrum Jülich

HMI  
Hahn-Meitner-  
Institut  
Uni Gö  
Universität  
Göttingen

MPG  
Max-Planck-  
Gesellschaft

MPIKG  
Max-Planck-Institut  
für Kolloid- und  
Grenzflächen-  
forschung

PDI  
Paul-Drude-Institut

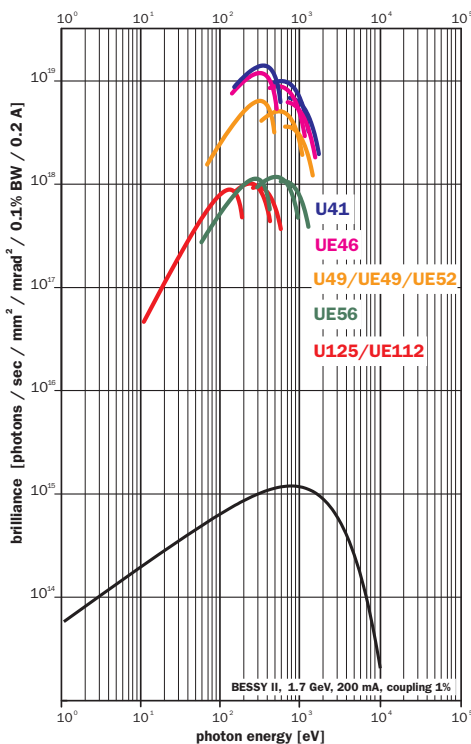
ID	Monochromator	Energy range (eV)	Operated by	Contact Persons
7T-WLS-1	KMC	6 k - 50 k	BAM/PTB	H. Riesemeier (BAM) A. Erko B. Müller (BAM)
	μSpot	2 k - 30 k	BAM/MPIKG	H. Riesemeier (BAM) I. Zizak O. Paris (MPIKG)
U125-2	SGM	20 - 500	BUS	R. Püttner (FUB) G. Reichardt
	KMC	6 k - 12 k	PDI/HUB	W. Braun (PDI) A. Erko P. Jenichen (PDI)
	10m-NIM	<10 - 35	Uni KI/BESSY	G. Reichardt I. Packe
7T-MPW	direct beam	3 k - 60 k	HMI	Ch. Genzel (HMI) A. Erko I. Denks (HMI) G. Wagener (HMI)
	KMC	3 k - 60 k	HMI	E. Dudzik (HMI) A. Erko R. Feyerherm (HMI) G. Wagener (HMI)
UE56-2	PGM 1	60 - 1,300	MPG	W. Mahler (MPG) B. Zada (MPG)
	PGM 2	60 - 1,300	MPG	W. Mahler (MPG) B. Zada (MPG)
6T-WLS 0.4T-LFD	Litho	> 2 k	BESSY	B. Löchel M. Bednarzik H.-U. Scheunemann H. Köhrich
U49-1	-	direct beam	PTB	R. Klein (PTB)
	13°		PTB	R. Klein (PTB) A. Gottwald (PTB)
	PGM	20 - 1,900	PTB	B. Beckhoff (PTB)
UE49	PGM a/b	85 - 1,600	BESSY	F. Kronast M. Mast J.-S. Schmidt
UE52	SGM	85 - 1,600	BESSY	K. Godehusen T. Zeschke F. Senf
	PGM	85 - 1,600	Uni Wü	D. Batchelor (Uni Wü) Ch. Jung Th. Schmidt (Uni Wü)
UE46	PGM	120 - 1,700	HMI	D. Schmitz (HMI) F. Senf H. Rossner (HMI)
UE56-1	PGM a/b	60 - 1,300	BESSY	T. Kachel Ch. Stamm J.-S. Schmidt
	ZP-mono	715 / 786 / 861	BESSY	A. Firsov I. Packe
	SGM	60 - 1,300	FZJ	S. Cramm (FZJ)
U41	TXM/STXM	~250 - ~600	BESSY/Uni Gö	P. Guttman (Uni Gö) G. Schneider
	PGM	170 - 1,800	BESSY	Ch. Jung M. Mast
U125-1	PGM 1	20 - 700	BESSY	O. Schwarzkopf F. Eggenstein
	PGM 2 a/b	5 - 180	BESSY	R. Follath St. Dorasch
7T-WLS-2	BL 14.1	4.5 k - 17.7 k	BESSY	U. Müller
	BL 14.2	4.5 k - 17.7 k	FUB	M. Fuchs (FUB)
	BL 14.3	4.5 k - 17.7 k	BESSY	U. Müller
U49-2	PGM 1	85 - 1,600	BESSY	O. Schwarzkopf J.-S. Schmid
	PGM 2	85 - 1,600	BTUC	P. Hoffmann (BTUC) W. Braun

# Dipole Beamlines at BESSY (January 2007)

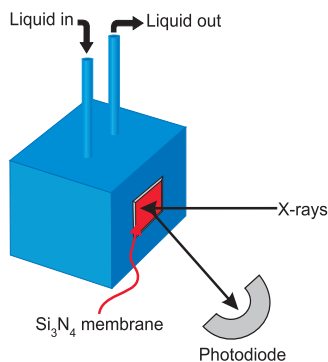
Further information on beamlines can be found on the 'user info pages' of the BESSY website

Monochromator	Energy Range (eV)	Operated by	Contact Persons
Litho EUV	95	BESSY	H.-U. Scheunemann H. Köhrich
KMC-1	1.7 k - 10 k	BESSY	M. Gorgoi M. Mertin
IR stations	Thz - 0.5	BESSY	U. Schade
ISSS	80 - 2,000	FHI	M. Hävecker (FHI) T. Blume A. Knop-Gericke (FHI)
Litho	direct beam	BESSY	B. Löchel M. Bednarzik H.-U. Scheunemann H. Köhrich
1m-NIM 1	3 - 35	PTB	M. Richter (PTB)
1m-NIM 2	3 - 35 white beam	PTB	R. Thornagel (PTB) R. Thornagel (PTB)
KMC	1.7 k - 10 k	PTB	M. Krumrey (PTB)
PGM	30 - 1,800	PTB	F. Scholze (PTB)
HE-SGM	200 - 700	CRG	A. Lippitz (BAM) O. Schwarzkopf
Optics-BL	20 - 2,000	BESSY	F. Senf
KMC 2	4.5 k - 15 k	BESSY	A. Erko I. Packe
PGM 3	20 - 1,900	BESSY	T. Kachel F. Eggenstein
3m-NIM	4 - 35	BESSY	G. Reichardt I. Packe
EDR	2 k - 12 k	Uni P	W. Leitenberger (Uni P) A. Erko
TGM 4	8 - 120	BESSY	K. Godehusen M. Mast
TGM 7	8 - 120	HMI	C. Pettenkofer (HMI) W. Bremsteller (HMI)
PGM-RD-BL	30 - 1,500	Uni Pet	Y. Dedkov (Uni DD) S. Molodtsov (Uni DD)
CP-NIM	4 - 35	BESSY	F. Schäfers M. Mertin

PTB  
Physikalisch-  
Technische  
Bundesanstalt  
HUB  
Humboldt-  
Universität zu  
Berlin  
FUB  
Freie Universität  
Berlin  
Uni P  
Universität  
Potsdam  
BAM  
Bundesanstalt für  
Materialforschung  
und -prüfung  
HMI  
Hahn-Meitner-  
Institut  
Uni DD  
Universität  
Dresden  
Uni Pet  
University  
St. Petersburg,  
Russia



Rapid prototyping for rapid pulses: Highly flexible mirror holders for the fs-laser line of the Femtosing source.



**LIQUIDROME cell for volatile liquids**

## Experimental Stations

**LIQUIDROME** is an experimental station dedicated for soft X-ray NEXAFS investigations on liquid and degassing sample. The experiments can be carried out under various conditions:

- pressure can be varied between  $10^{-6}$  mbar and 1,000 mbar of inert atmosphere (typically Helium)
- temperature can be varied between  $-50^{\circ}\text{C}$  and  $+100^{\circ}\text{C}$
- electric and magnetic fields can be applied.

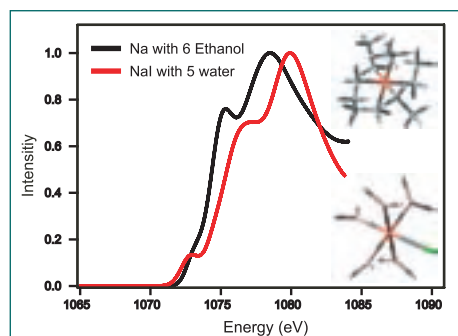
A window located on a nozzle close to the region of interaction separates the synchrotron radiation from the working conditions inside the chamber. Different window

materials like  $\text{Si}_3\text{N}_4$ , Aluminum or Polyimide are available and can be changed in-situ. The fluorescence yield is recorded via a GaAsP-diode. In addition, the electron yield can also be measured if required.

Non-volatile liquids can be studied in a jet, with a jet speed between 100 ml and 1,000 ml per minute. For volatile liquids, a sealed cell is available, where the fluid circulates behind a

$\text{Si}_3\text{N}_4$ -window (see Fig). A setup to measure stop-flow chemical reaction kinetics can be implemented. The chamber is quite spacious to allow for special detectors or sample environments to be inserted by users.

For the data analysis, a bundle of software packages is available to calculate the electronic structure of the sample under study. Using the software codes StoBe, FEFF8, Multiplet and Gaussian03, NEXAFS or EXAFS spectra can be derived on the basis of structural models. Furthermore, information on molecular energies and structure or on bond and reaction energies can be retrieved (see graph).



**NEXAFS spectra of Na in ethanol and water (E.F. Aziz et al., Phys. Rev. B, 73, 075120 (2006))**

**ISS** (Innovative Station for In Situ Spectroscopy), a project of BESSY and the Inorganic Chemistry department of the FHI (Fritz-Haber-Institut der Max-Planck-Gesellschaft), is dedicated to study the interaction of surfaces with their environment (i.e. gas/solid interfaces) under conditions equal to or close to reality allowing a detailed characterisation of catalytic relevant materials under realistic conditions to push forward rational catalyst design.

The PGM design offers the possibility to easily adapt the beamline to the users need (e.g. high flux, high resolution, or high purity of the X-rays). It delivers photons in the energy range between 80 eV and 2,000 eV. The monochromator holds two gratings (600 l/mm, 1,200 l/mm). Fast photon energy scans are feasible ("Quick NEXAFS") due to the implementation of a continuous driving mode of the monochromator. A typical spot size at sample position is around  $150\ \mu\text{m}$  (horizontal)  $\times$   $100\ \mu\text{m}$  (vertical, depending on exit slit size).

The high-pressure X-ray photoelectron spectroscopy (XPS) end-station of the FHI is equipped with differentially pumped electrostatic lens system attached to a modified hemispherical electron analyser (PHOIBOS 150). This set-up allows both in situ XPS and X-ray absorption spectroscopy measurements (total electron and Auger electron yield mode) in the presence of a reactive gas ( $p \sim 1$  mbar). The ambient gas phase can be analysed simultaneously to the spectroscopic characterisation of the sample by electron impact mass spectrometers (QMS) and a proton transfer reaction mass spectrometer (PTR-MS). Heating of the sample up to approx. 1,000 K is provided by a NIR-laser from the rear. The station is equipped with a sample transfer system that allows fast exchange of samples via a load lock.

The experimental end-station is placed inside a ventilated lab with safety sensors for  $\text{H}_2$  and hydrocarbons allowing the use of hazardous substances. The lab provides up to eight high purity grade gases as well as extra space for sample preparation and chemicals storage.

Regular operation of ISS will start in the 2<sup>nd</sup> semester of 2007.

### Contact LIQUIDROME:

Emad Flear Aziz Bekhit  
emad.aziz@bessy.de

### Contact ISS:

Axel Knop-Gericke  
knop@fhi-berlin.mpg.de

Michael Hävecker  
mh@fhi-berlin.mpg.de



**ISS endstation**

## Permanent experimental stations

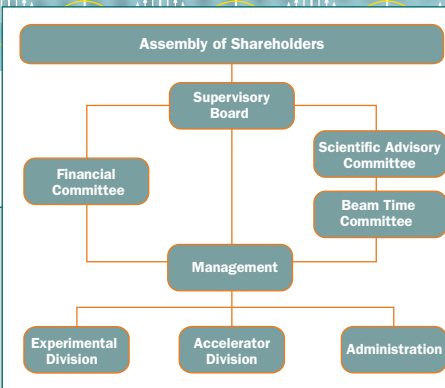
Experiment	Contact	Location
THz spectroscopy <sup>BioSR, Ind</sup>	holldack@bessy.de	IR
IR-spectroscopy and -microscopy <sup>BioSR, Ind</sup>	schade@bessy.de	IR
IR ellipsometry <sup>Ind</sup>	hinrichs@isas-berlin.de	IR
UVIS - protein circular dichroism spectroscopy <sup>BioSR</sup>	baumgaer@rz.uni-potsdam.de	3m-NIM
SURICAT - photoelectron and absorption spectroscopy	antje.vollmer@bessy.de	optics beamline
Two-Photon-Photoemission Experiment	weinelt@mbi-berlin.de	UE112 PGM 1
fs-slicing facility	hermann.duerr@bessy.de	UE56-1 PGM 1
1 <sup>3</sup> -ARPES ultra high resolution photoemission	s.borysenko@ifw-dresden.de	UE112 PGM 2b
SAMIC - spectroscopy and microscopy integrating chamber <sup>Ind</sup>	patrick.hoffmann@tu-cottbus.de	U49-2 PGM 2
SPEEM - spin resolved photoemission microscopy <sup>planned</sup>	florian.kronast@bessy.de	UE49 PGM a
SMART - spectro-microscope with highest spatial resolution	thomas.schmidt@physik.uni-wuerzburg.de	UE49 PGM b
7T high-field end station	schmitz@hmi.de	UE46 PGM
ISS in-situ catalysis beamline <sup>Inds</sup>	knop@fhi-berlin.mpg.de	ISS PGM
Reflectometry <sup>Ind</sup>	schaefers@bessy.de	optics beamline
XM - X-ray Microscopy <sup>BioSR, Ind</sup>	guttman@bessy.de	U41-XM
X-ray lithography <sup>Ind</sup>	loechel@bessy.de	6T-WLS, DIP 06
HIKE- Hard X-ray high kinetic energy photoelectron spectroscopy	mihaela.gorgoi@bessy.de	KMC 1
X-ray diffraction during MBE	braun@pdi-berlin.de	U125-2 KMC
$\mu$ Spot micro-XANES, -EXAFS, -fluorescence <sup>BioSR</sup>	zizak@bessy.de	7T-WLS-1
Diffraction, XANES, EXAFS	erko@bessy.de	KMC 2
Protein crystallography <sup>BioSR, Ind</sup>	umue@bessy.de	7T-WLS-2
BAMline - nondestructive testing in analytical chemistry <sup>Ind</sup>	heinrich.riesemeier@bam.de	7T-WLS-1
EDDI - energy dispersive diffraction	genzel@hmi.de	7T-MPW
MagS - resonant magnetic scattering	feyerherm@hmi.de	7T-MPW

## Variable experimental stations

Experiment	Contact
HIRES - high resolution electron spectrometer	rader@bessy.de
PHOENEXS - photoemission and near edge X-ray spectroscopy	varykhalov@bessy.de
MUSTANG - multi-user stage for angular resolved photoemission	gavrila@bessy.de
High resolution spinpolarisation photoelectron spectroscopy	c.m.schneider@fz-juelich.de
Stored Nano Particels	ruehl@phys-chemie.uni-wuerzburg.de
So-Li-AS - solid-liquid-analysis system	mayerth@surface.tu-darmstadt.de
VUV/XUV ellipsometry <sup>Ind</sup>	esser@isas-berlin.de
Scattering experiments in the VUV/XUV-range	eugen.weschke@physik.fu-berlin.de
Photoemission microscope for ps time resolved spectroscopy <sup>Ind</sup>	schoenhe@mail.uni-mainz.de
LIQUIDROME for NEXAFS on liquids and degassing samples <sup>Ind</sup>	emad.aziz@bessy.de
Soft X-ray emission spectrometer	anna.zimina@bessy.de
CISSY - CIS- diagnostic using Synchrotron radiation	cissy@hmi.de
ROSA - rotateable spectrometer apparatus	szargan@rz.uni-leipzig.de
Fluorescence spectroscopy <sup>Ind</sup>	ruediger.mitdank@physik.hu-berlin.de
Polarimetry	schaefers@bessy.de

**BioSR: suitable for biological samples**

**Ind: suitable for industrial users**



### Supervisory Board:

Prof. Dr. J. Treusch (Chairman)	Forschungszentrum Jülich
Prof. Dr. E. Umbach (Vice-Chairman)	Universität Würzburg
Frau Dr. B. Vierkorn-Rudolph	Bundesministerium für Bildung und Forschung
Prof. Dr. E. O. Göbel	PTB Braunschweig
Prof. Dr. R. Maschuw	Forschungszentrum Karlsruhe
Prof. Dr. H. Braun	Max-Planck-Gesellschaft München
Frau Dr. Ulrike Gutheil	Technische Universität Berlin
Prof. Dr. J. Schneider	DESY Hamburg
MinR. N. Barz	Bundesministerium für Wirtschaft und Technologie
Prof. Dr. M. Steiner	Hahn-Meitner-Institut Berlin
Senatsdirig. W. Eckey	Senatsverwaltung für Wissenschaft, Forschung und Kultur

### Scientific Advisory Committee:

Prof. Dr. Robert Schlögl (Chairman))	Fritz-Haber-Institut der MPG Berlin
Prof. Dr. Hans Ade	North Carolina State University
Prof. Dr. Vlasta Bonacic-Koutecký	Humboldt Universität zu Berlin
Prof. Dr. Reinhard Brinkmann	DESY Hamburg
Prof. Dr. Thomas Elsässer	Max-Born-Institut Berlin
Prof. Dr. Roger Falcone	ALS Berkeley (Institutional Member)
Prof. Dr.-Ing. Norbert Langhoff	Institut for Scientific Instruments Berlin
Prof. Dr. Nils Martensson	MAXLAB, Sweden
Prof. Dr. Eckhard Rühl	Freie Universität Berlin
Priv.- Prof. Dr. Ilme Schlichting	Max-Planck-Institut für medizinische Forschung Heidelberg
Prof. Dr. Hans-Peter Steinrück	Universität Erlangen-Nürnberg
Prof. Dr. Metin Tolan	Universität Dortmund
Prof. Dr. Richard Walker	Rutherford Appleton Laboratory (Diamond), Chilton

### Permanent Guests

Dr. Josef Feldhaus	HASYLAB/DESY Hamburg
Prof. Dr. Helmuth Möhwald	Max Planck Institut für Kolloid- und Grenzflächenforschung, Potsdam
Prof. Dr. Jürgen Richter	Bundesministerium für Bildung und Forschung
Dr. Rainer Schuchhardt	Senatsverwaltung für Wissenschaft, Forschung und Kultur Berlin

### Beam Time Committee

Prof. Dr. Wilfried Wurth (Chairman)	Universität Hamburg
Prof. Dr. Lorenz Singheiser (Vice-Chairman)	Forschungszentrum Jülich
Prof. Dr. Stefan Blügel	Forschungszentrum Jülich
Prof. Dr. Ralph Claessen	Universität Würzburg
Prof. Dr. Thomas Elsässer	Max-Born-Institut Berlin
Prof. Dr. Karsten Horn	Fritz-Haber-Institut der MPG Berlin
Dr. Michael Meyer	Centre Universitaire Paris-Sud
Prof. Dr. Anke Rita Pyzalla	Max-Planck-Institut für Eisenforschung Düsseldorf
Prof. Dr. Liu Hao Tjeng	Universität zu Köln
Prof. Dr. Hartmut Zabel	Ruhr-Universität Bochum

### Sub-Committee Protein Crystallography

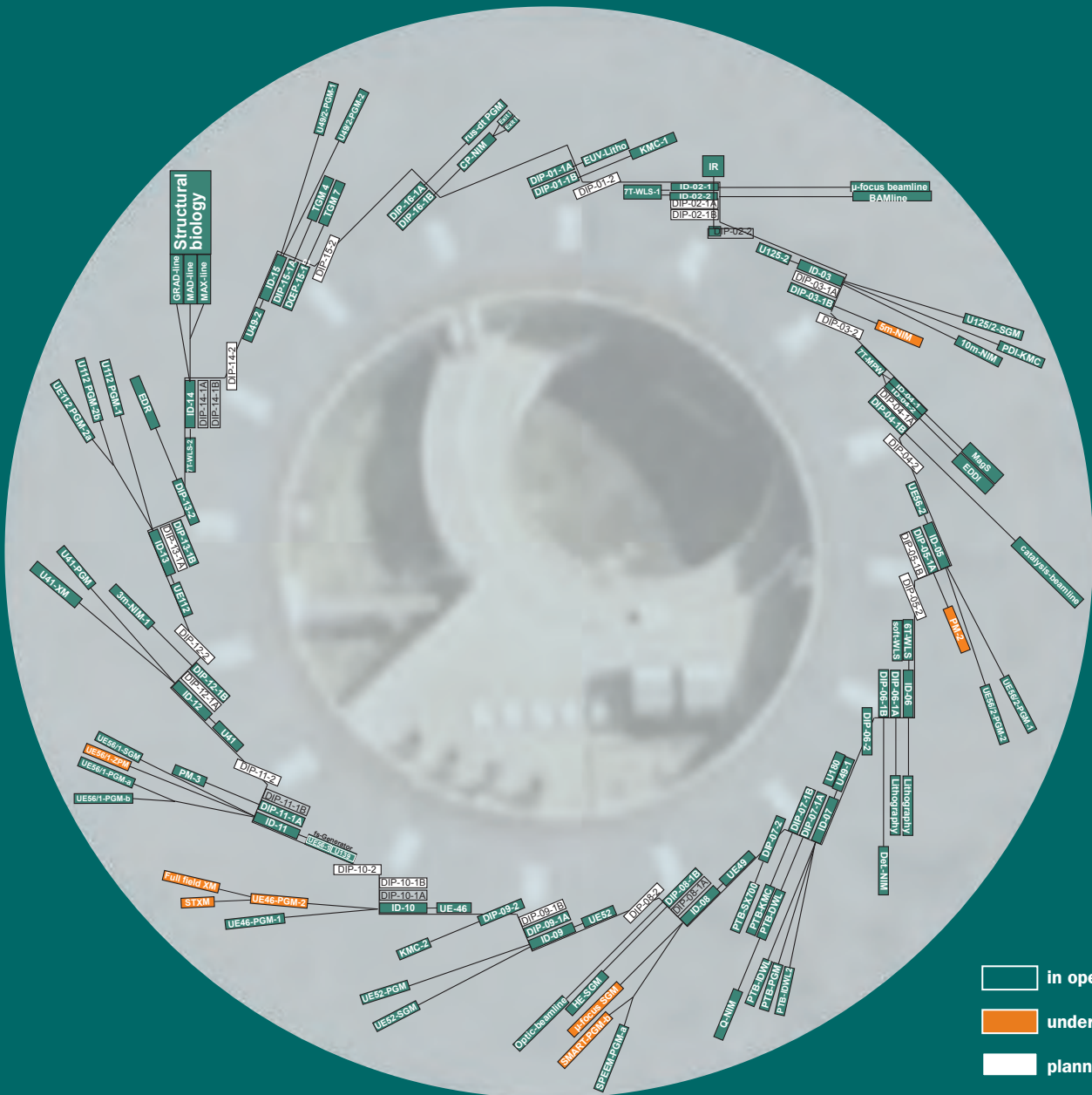
Prof. Dr. Ralf Ficner	Universität Göttingen
Prof. Dr. Peter Lindley	Universität Lissabon
Dr. Matthias Wilmanns	EMBL Hamburg

### Financial Committee

Ass.jur. S. Lettow (Chairman)	Forschungszentrum Karlsruhe
R. Kellermann (Vice-Chairman)	Forschungszentrum Jülich
Dr. W. Buck	PTB Berlin
M. Schleier	Max-Planck-Gesellschaft München
Dr. R. Schuchardt	Senatsverwaltung für Wissenschaft, Forschung und Kultur Berlin
H. Görres	Bundesministerium für Bildung und Forschung

### User Committee

Ralph Püttner (Chairperson)	Freie Universität Berlin
Birgit Kanngießer (Vice-Chairperson)	Technische Universität Berlin
Peter Baumgärtel	Universität Potsdam
Wolfgang Braun	Paul-Drude-Institut
Ralf Feyerherm	Hahn-Meitner-Institut



**Scientific Director**

Prof. Dr. Dr. h.c. Wolfgang Eberhardt  
 Secretary: Ines Maupetit  
 phone +49 (0)30 / 6392 4633  
 fax +49 (0)30 / 6392 2989  
 wolfgang.eberhardt@bessy.de,  
 ines.maupetit@bessy.de

**Technical Director**

Prof. Dr. Eberhard Jaeschke  
 Secretary: Dr. Nikoline Hansen  
 phone +49 (0)30 / 6392 4651  
 fax +49 (0)30 / 6392 4632  
 eberhard.jaeschke@bessy.de,  
 nikoline.hansen@bessy.de

**Administration**

Thomas Frederking  
 Secretary: Katrin Rosenblatt  
 phone +49 (0)30 / 6392 2901  
 fax +49 (0)30 / 6392 2920  
 thomas.frederking@bessy.de,  
 katrin.rosenblatt@bessy.de

**Beamtime Coordination**

Dr. Walter Braun, Dr. Gerd Reichardt  
 Secretary: Stine Mallwitz  
 phone +49 (0)30 / 6392 2904  
 fax +49 (0)30 / 6392 4673  
 beamtime@bessy.de

**User Office**

Ines Drochner, Cornelia Stürze  
 phone +49 (0)30 / 6392 4734  
 fax +49 (0)30 / 6392 4746  
 useroffice@bessy.de

**Public Relations**

Gabriele André,  
 Dr. Heike Henneken,  
 Dr. Markus Sauerborn  
 phone +49 (0)30 / 6392 4921  
 fax +49 (0)30 / 6392 4972  
 pr@bessy.de

**Credits**

For providing photographs and drawings we would like to thank:  
 Hendrik Spohler / laif (Front cover)  
 Kai Godehusen, Berlin  
 Alastair Rae, Northern Ireland  
 Books Illustrated, Illustration by Susan Scott, UK  
 Bill Adler, Washington, USA  
 Bureau International des Poids at Mesures, Paris, France  
 Cartoonstock.com  
 Euler Hermes, Hamburg  
 Infineon Technologies, München  
 Juan Salmotal Franco, Barcelona, Spain  
 Keith Petrie, Auckland, NZ  
 Michael Peters, Kürten  
 Mihaela Gorgoi, Berlin  
 National Academy of Sciences, USA  
 Physikalisch-Technische Bundesanstalt, Braunschweig  
 Silko Barth, Berlin





